INTERIM REPORT

Multi-pass and Non-concentric Target Circular Synthetic Aperture SONAR (CSAS)

SERDP Project MR-2439

APRIL 2016

Dr. Timothy M. Marston
University of Washington

Dr. Jermaine L. Kennedy
Naval Surface Warfare Center Panama City Division

Distribution Statement A
This document has been cleared for public release

SERDP
DOD ▪ EPA ▪ DOE

Page Intentionally Left Blank

This report was prepared under contract to the Department of Defense Strategic Environmental Research and Development Program (SERDP). The publication of this report does not indicate endorsement by the Department of Defense, nor should the contents be construed as reflecting the official policy or position of the Department of Defense. Reference herein to any specific commercial product, process, or service by trade name, trademark, manufacturer, or otherwise, does not necessarily constitute or imply its endorsement, recommendation, or favoring by the Department of Defense.

Page Intentionally Left Blank

REPORT DOCUMENTATION PAGE

Form Approved
OMB No. 0704-0188

The public reporting burden for this collection of information is estimated to average 1 hour per response, including the time for reviewing instructions, searching existing data sources, gathering and maintaining the data needed, and completing and reviewing the collection of information. Send comments regarding this burden estimate or any other aspect of this collection of information, including suggestions for reducing the burden, to Department of Defense, Washington Headquarters Services, Directorate for Information Operations and Reports (0704-0188), 1215 Jefferson Davis Highway, Suite 1204, Arlington, VA 22202-4302. Respondents should be aware that notwithstanding any other provision of law, no person shall be subject to any penalty for failing to comply with a collection of information if it does not display a currently valid OMB control number.
PLEASE DO NOT RETURN YOUR FORM TO THE ABOVE ADDRESS.

1. REPORT DATE *(DD-MM-YYYY)*	2. REPORT TYPE	3. DATES COVERED *(From - To)*
16/06/2016	Interim Report	July 2014 - April 2016

4. TITLE AND SUBTITLE
Multipass and Non-Concentric Target CSAS

5a. CONTRACT NUMBER

5b. GRANT NUMBER

5c. PROGRAM ELEMENT NUMBER

6. AUTHOR(S)
Dr. Jermaine Kennedy
NSWC-PCD

Dr. Timothy M. Marston
Applied Physics Laboratory, University of Washington

5d. PROJECT NUMBER
MR-2439

5e. TASK NUMBER

5f. WORK UNIT NUMBER

7. PERFORMING ORGANIZATION NAME(S) AND ADDRESS(ES)
NSWC-PCD, 110 Vernon Avenue, Code X-11, Panama City Beach, FL 32407
APL, University of Washington, Seattle, Washington 98105-6698

8. PERFORMING ORGANIZATION REPORT NUMBER

9. SPONSORING/MONITORING AGENCY NAME(S) AND ADDRESS(ES)
Strategic Environmental Research and Development Program
4800 Mark Center Drive
Suite 17D03
Alexandria, VA 22350-3605

10. SPONSOR/MONITOR'S ACRONYM(S)
SERDP

11. SPONSOR/MONITOR'S REPORT NUMBER(S)

12. DISTRIBUTION/AVAILABILITY STATEMENT
Approved for public release; distribution is unlimited.

13. SUPPLEMENTARY NOTES
N/A

14. ABSTRACT
The primary objective of this project is to create methods for the coherent fusion of CSAS data collected at multiple radii or altitudes, with the intention of generating datasets that could be used for accurate target classification, model parameter adjustment, or to train recognition algorithms using environmentally relevant data.

15. SUBJECT TERMS
N/A

16. SECURITY CLASSIFICATION OF:			17. LIMITATION OF ABSTRACT	18. NUMBER OF PAGES	19a. NAME OF RESPONSIBLE PERSON
a. REPORT	b. ABSTRACT	c. THIS PAGE			Dr. Jermaine Kennedy
U	U	U	UU	80	19b. TELEPHONE NUMBER *(Include area code)* 850-235-5804

Page Intentionally Left Blank

ACKNOWLEDGEMENT

This report was prepared under contract to the Department of Defense Strategic Environmental Research and Development Program (SERDP). The publication of this report does not indicate endorsement by the Department of Defense, nor should the contents be construed as reflecting the official policy or position of the Department of Defense. Reference herein to any specific commercial product, process, or service by trade name, trademark, manufacturer, or otherwise, does not necessarily constitute or imply its endorsement, recommendation, or favoring by the Department of Defense.

Page Intentionally Left Blank

TABLE OF CONTENTS

ACKNOWLEDGEMENT....iii

TABLE OF CONTENTS....iv

LIST OF TABLES....v

LIST OF FIGURES....v

LIST OF ACRONYMS....x

KEYWORDS....x

OBJECTIVE....1

TECHNICAL APPROACH....1
- FY15 Experimental technical approach....2
- FY15 Signal processing technical approach....3
- Application of FY14 coregistration algorithms to FY15 field data and subsequent modifications....4
- Multilateration....5
- Coregistration model changes....13
- Roll and heave calibration. 19
- Software implementation....27
- Coherent multipass data processing....28
- 3D Autofocus....30

RESULTS AND DISCUSSION....34

CONCLUSIONS TO DATE....41

REFERENCES....43

LIST OF TABLES

Table 1- Standard deviations of the vectors of the estimated parameters for the models incorporating bathymetry verses assuming a flat bottom.

Table 2- A list of the scanned targets and the number of scans completed for the radial and altitude types. The AUV malfunctioned after 6 scans around the steel barrel, and no altitude scans exist for either the steel barrel or the proud, solid 2-1 aluminum cylinder.

LIST OF FIGURES

Figure 1. Example of a synthesized multipass array. The vertical samples are irregular as a result of the different vertical spacings between the multipass scans and the interferometric receiver arrays. Additional irregularity occurs because of currents and, for the bottom three scans, a GPS localization offset acquired during a resurfacing operation.

Figure 2- Underwater photographs of various targets deployed in the Gulf of Mexico off the shore of Panama City Beach, FL.

Figure 3- An example scan showing the flight path of the AUV in Cartesian coordinates (right figure, blue line) and the location of the test-patches used for multilateration (right figure, red dots). The image snippets at left correspond to the test-patches.

Figure 4- The point-spread functions of the individual test patches, estimated via application of an autofocusing routine.

Figure 5- The radial, height, and angular corrections that are estimated from the iterated multi-lateration process and applied to the 3D coordinates of the SAS sonar platform.

Figure 6- The original point-spread functions (L) and point-spread functions after the coordinate updates (R).

Figure 7- CSAS image of a proud, vertically oriented plastic barrel on a limestone and coral sediment. Focus is achieved throughout the image excepting out-of-plane regions, in which case defocusing is due to being out of plane.

Figure 8- Zoomed in section of Figure 7 showing the barrel.

Figure 9- FY14 SAS multipass coregistration model.

Figure 10- FY15 AUV-scan coregistration model. The parameters are h_s: the height of the reference sonar above the nominal ground-plane, h_1: the initial vertical baseline estimate between the reference and comparison scan, Δh: the vertical baseline error, R: the radial location of the reference scan, r_1: the initial radial baseline estimate, Δr: the radial error variable, c_1: the reference sound-speed, c_2: the sound speed of the medium at the time the second scan is taken and lastly h_D: the sediment height relative to the nominal ground-plane. Lowercase r denotes the coordinate radial direction, and lowercase h represents the coordinate vertical direction.

Figure 11- Top: phase measurements produced by patch-wise correlation. Middle: correlation coefficients for the patches. Bottom: radial displacement estimates measured by combining the phase estimates with coarse dislocation estimates found using the correlation peaks.

Figure 12- Top left: Original displacement data estimated via patch-wise correlation. Middle left: the displacement surface, reconstructed using the bases functions and estimated error parameters for the FY15 model incorporating bathymetry. Bottom left: the displacement surface, reconstructed using the bases functions and estimated parameters for a flat-bottom assumption. Middle right: the model – data residual for the FY15 model. Bottom right: the residual error for the flat-bottom model. The color scale is in meters.

Figure 13- The estimated error parameters for the full FY15 model (blue) and the flat-bottom model (red).

Figure 14- Left: array localization results using the flat-bottom model (blue) vs. incorporation of bathymetry (red). Right: the range-projected vertical beamforming results for the case in which a flat-bottom is assumed (top) vs. incorporation of bathymetry (bottom).

Figure 15- Illustration of out-of-plane defocusing for CSAS images. The left column shows a scene imaged at two focusing planes: a plane corresponding to the height of the rocky outcropping and a plane corresponding to the adjacent sandy sediment. The insets labeled *A* and *B* show the relative focus of these patches for the different focusing planes: in the top row, patch *A* is in focus while patch *B* is not. For the bottom row the focus is reversed.

Figure 16- Flow chart of the entropic height map estimation process. Boxes in blue are data products, boxes in gray are processes.

Figure 17- Illustration of the entropic height map estimation process. The image at top left is sub-divided into a series of image patches (shown at right). These patches are individually re-focused at different height planes, and the height-plane corresponding to the maximum image contrast is selected as the true height of the patch.

Figure 18- The entropic height map generated using the image in shown in Fig. 17 (note that the resolution cells are half the size of the cells shown in Fig.17).

Figure 19- Illustration of the geometry of the interferometric data product. The interferometric readings from the sonar give bathymetric estimations for a line or beam extending from the coordinate of the aperture extending normal to the sonar (i.e., intersecting with the origin).

Figure 20- The bathymetry measured by the interferometric system (bottom) and the entropic height-map (top) converted to the sensor-centered format of the interferometric system.

Figure 21- This figure shows the difference between the interferometry height estimate and the entropic height estimate. Trends in the range direction are a result of roll and heave errors. Sound-velocity profile could potentially also introduce errors but these are not currently considered.

Figure 22- Interferometric roll (red) and heave (black) error bases computed via finite difference at a particular aperture location (θ ~= 100°). These bases are computed for all θ and used to fit the residual difference data shown in Fig. 20.

Figure 23- The residual roll error (top) and height error (bottom) shown in degrees and meters. Note the large roll offset of about half a degree.

Figure 24- The final residual between the interferometric and entropic bathymetry estimates.

Figure 25- Illustration of the symmetry of circular bathymetry estimates separated by 180 in a circular aperture.

Figure 26- Circular symmetry errors for the interferometric bathymetry estimates before (top) and after (bottom) calibration via comparison with the entropic estimates. This comparison is make by taking a bathymetry estimate and subtracting itself from a version that has been flipped around the range point corresponding to the origin of the circle and shifted by 180 degrees.

Figure 27- Processing flow for multipass data showing the three main stages (single scan processing, co-registration and 3D processing), the primary actions completed by the program and the required inputs and outputs.

Figure 28- Illustration of the vertical target distribution value D (in this case the exposed portion of a UXO) and its relationship to the tomographic grazing angle sampling value $\Delta\Theta$. Note that if the sonar penetrates the sediment that D would be the entire height of the UXO, including the buried portion.

Figure 29- Illustration of the 3D beamforming process. Following projection of each scan to the ground-plane the data is beamformed in the vertical dimension (A). This is done for all points around the aperture (B). A far-field conversion is applied to each height plane which is then projection-slice beamformed in $K_{x,y}$ wavenumber space [18]. This can be converted to a 3D wavenumber spectrum in $K_{x,y,z}$ by computing a vertical Fourier transform or an image by taking an inverse two-dimensional Fourier transform in the horizontal dimensions. The image and wavenumber domain can be computed from each other via 3D Fourier transform.

Figure 30- Outline of the vertical map-drift algorithm.

Figure 31- The application of the map-drift algorithm to the 3D data and the correction process. The raw, vertically beamformed data (top) is passed to the map-drift algorithm from which a phase-correction datacube is computed. The two-dimensional Fourier transform of the vertically beamformed data is computed in the *Z* and *r* dimensions and the phase correction is applied. The corrected dataset (bottom) is recovered following the inverse two-dimensional Fourier transformation.

Figure 32- The vertically beamformed data, averaged in the range-dimension and visualized. The bright line corresponds to the sediment interface. In the uncorrected data, the sediment height changes with look angle, vs. in the corrected data in which it remains at a constant altitude.

Figure 33- Slices through the 3D image data cube (top and middle) and a rendered 3D image (bottom) for the case in which no vertical map-drift was applied (left) versus the case in which it was applied (right). The images at right show superior focus in the vertical dimension. Note that back-scattering angle is mapped to color in the above examples.

Figure 34- Photograph of a 155 mm Howitzer shell (right) and the 3D volumetric acoustic image (left), showing the material boundaries at the front of the shell, the components of the end-cap, and a nylon rope tied around the center for diver manipulation (not in photo).

Figure 35- Rendered images and projections of the volumetric data corresponding to the scans described in Table 1. Column 1) shows the linear scale three-quarter view volumetric images rendered using alpha blending, column 2) shows projections of the volumetric images onto the *XZ* plane, column 3) shows projections onto the *YZ* plane, and column 4) shows projections onto the *XY* plane. From top to bottom, the rows show: a) proud howitzer, altitude scan, b) proud howitzer, radial scan, c) oblique howitzer, altitude scan, d) oblique howitzer, radial scan, e) proud vertical steel barrel, radial scan, and f) proud 2-1 solid aluminum cylinder, radial scan.

Figure 36- Illustration of high-frequency image snippets produced using the multipass 2-1 aluminum cylinder data. The variables are azimuthal and vertical rotation. The

figure is for illustrative purposes, an actual training set would vary more finely over angle, and over a larger span vertically, as well as introduce other variables such as noise and various types of realistic phase error.

Figure 37- The coherently processed low-requency 3D dataproduct from a multipass set, in this case containing a coral outcropping (red arrow) and a proud howitzer shell (white arrow). Image (A) shows the 3D image from a three-quarter view perspective, while (B) and (C) project the image onto the [X, Y], [Y, Z] and [X, Z] planes. Image (D) is a three-quarter view of the three-dimensional wavenumber spectrum of the image.

Figure 38- A high frequency three-quarter view (A) rendering of the rock and howitzer image shown in Fig. 37, along with two slices (B and C) through the rock. Note that overhangs are well imaged using the 3D tomography approach.

Figure 39- 3D snippet of the howitzer scene, showing just the howitzer. Image (A) is a three-quarter view, and image (B) is a horizontal planar slice through the image, showing the tip, the sides, the endcap, and material boundaries.

Figure 40- (A) a vertical slice through the image snippet showing a glint and its sub-sediment reflection, and (B and C) the three-dimensional wavenumber spectrum for the 3D snippet.

Figure 41- 3D multipass image of a lobster trap. Image (A) is a three-quarter view of the target, and (B), (C), and (D) are slices that show significant external and internal features of the target.

Figure 42- 3D multipass image of a plastic barrel. Image (A) is the three-quarter view of the target. Image (B) shows a side-view, emphasizing a corner scattering mechanism with the black arrow. Figure C is a cutaway of the target, where the red arrows show the enhanced scattering from the portion of the barrel filled with concrete and the white arrow points to the suspended sphere.

Figure 43- 3D multipass image of a car tire with no rim. Images (A) and (B) show two different views of the target, and image (C) shows a cutaway. From Fig. (C) it is clear that corner scattering dominates the backscattered response.

Figure 44- 3D multipass image of rock and coral sediment. Figure (A) shows the region from a three-quarter view perspective, and (B) – (D) are slices of the image.

LIST OF ACRONYMS

3D-3 Dimensional
AUV-Autonomous Underwater Vehicle
CSAS- Circular Synthetic Aperture Sonar
DoD-Department of Defense
kHz-kiloHertz
ONR-Office of Naval Research
SAS-Synthetic Aperture Sonar
SERDP-Strategic Environmental Research and Development Program
UXO-Unexploded Ordnance

KEYWORDS

Circular Synthetic Aperture Sonar of UXO, Synthetic Aperture Sonar of UXO, underwater UXO

OBJECTIVE

The Department of Defense (DoD) and the Strategic Environmental Research and Development Program (SERD) have identified a need for the development of systems with the ability to detect and identify submerged unexploded ordnance (UXO). Circular synthetic aperture sonar (CSAS) has been demonstrated to be an extraordinarily powerful tool for a variety of sonar based object classification/identification tasks, potentially including UXO detection. CSAS data products include high-resolution imagery and data ideally suited for acoustic frequency response vs. angle ("acoustic color") based target recognition. Research efforts aimed at modeling the acoustic response of targets in marine environments have identified several hurdles that must be overcome to maximize the effectiveness of response-based classification. These include response sensitivity to environmental parameters, attenuation and modification of features with aspect angle, and the coupling of structural modes to grazing angle which occurs in linear scan systems or, alternatively, in circular scan systems when a target is non concentric (SERDP projects MR-2230, 2231, & 1665). The insonification of targets over both a broad set of aspect and grazing angles makes multipass CSAS an ideal approach for addressing these difficulties. The primary objective of this project is to create methods for the coherent fusion of CSAS data collected at multiple radii or altitudes, with the intention of generating datasets that could be used for accurate target classification, model parameter adjustment, or to train recognition algorithms using environmentally relevant data. In support of the primary objective, methods for processing the co-registered data to reduce clutter, correct for near-field effects, and extrapolate/interpolate between multi-pass datasets to simulate target responses from arbitrary scan paths will be developed.

Experimental efforts in FY15 focused on using a fielded sonar system to collect multipass circular scans around UXO in un-controlled environments (in contrast to FY14, in which a rail system was used in a test pond). Signal processing efforts focused on using the collected data to develop a robust framework for coherent multi-pass SAS signal processing. This interim report will describe the details of the field experiments, as well as the signal processing efforts. The results were highly successful, and several papers describing the efforts were immediately drafted for journal and conference submission, all of which have been accepted with the addition of an invitation to give a tutorial on the subject in Europe. These papers will be appended to this interim report as supplementary material, and readers interested in the more technical aspects of some of the signal processing will be referred to specific sections of these papers.
The bulk of the technical content is deferred to the appended papers, however as-of-yet unpublished technical approaches will be discussed in detail in this report.

TECHNICAL APPROACH

As stated in the FY14 interim report, project MR-2439 contains two threads of effort: one pertaining to experimental data acquisition and the other aimed at processing the acquired data. The experimental half of this effort is intended to generate a database of realistic multi-pass circular scan data for UXO that can be used in the signal processing effort to develop data processing algorithms, discover the challenges associated with 3D data-processing and co-registration inherent to real data with phase and timing errors, and test co-registration and data

projection algorithms. As in the FY14 interim report, this report will begin by describing the FY15 experimental efforts and follow with the signal processing technical approach.

FY15 EXPERIMENTAL TECHNICAL APPROACH

Two multi-pass SAS experiments were carried out in FY15. The SAS system has two operational frequency bands: a high frequency band with a center frequency in the hundreds of kilohertz and a low frequency band with a center frequency in the tens of kilohertz. The SAS system was mounted on a REMUS 600 autonomous underwater vehicle [1]. The first test, conducted off the coast of Panama City Beach, Florida in December of 2014, was performed in 20 meters of total water depth, over a flat sediment composed primarily of fine sand and small shell fragments. Two different scan patterns were utilized. The first pattern used circular scans with a constant radius of 30 meters altitudes that varied between 4.3 meters and 6.9 meters in altitude, in steps of 0.3 meters. The second pattern, which was designed to be more compatible with tow body systems, fixed the altitude at 6 meters and varied the radii between 27 and 35 meters in increments of 1 meter. In total, both scans required 9 individual circular scans to form the full aperture. The presence of two parallel receive arrays separated by a vertical baseline on board the SAS system resulted in two vertical samples per scan, for a total of 18 sample points per multi-pass set. More details can be found in [2], which has been appended. Figure 1 is an example of an experimental realization of a vertical multipass set.

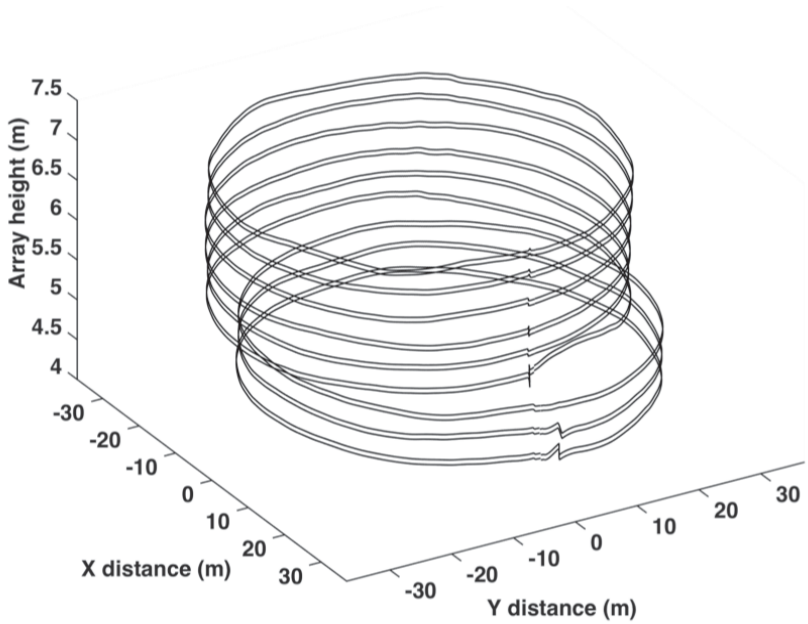

Figure 1. Example of a synthesized multipass array. The vertical samples are irregular as a result of the different vertical spacings between the multipass scans and the interferometric receiver arrays. Additional irregularity occurs because of currents and, for the bottom three scans, a GPS localization offset acquired during a resurfacing operation.

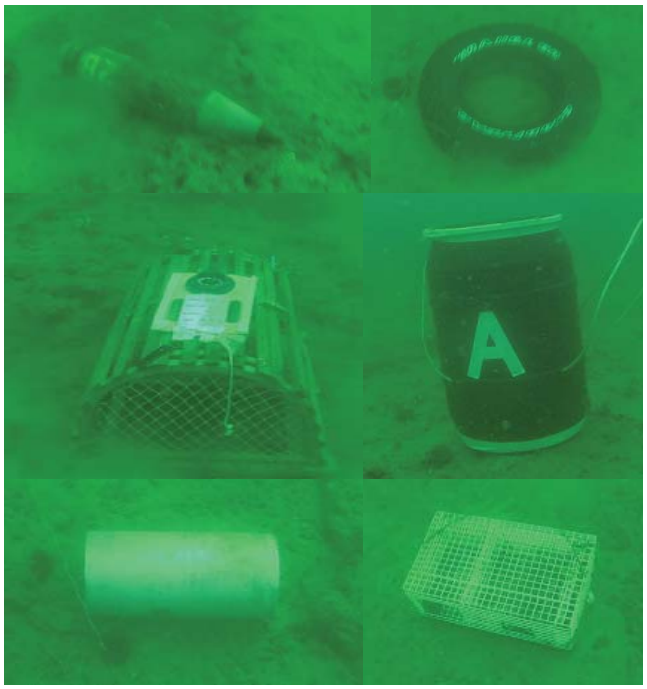

Figure 2. Underwater photographs of various targets deployed in the Gulf of Mexico off the shore of Panama City Beach, FL. The targets in this figure were scanned during the second set of tests conducted in June 2015.

The second test, also conducted off the coast of Panama City Beach, Florida, was performed in June of 2015. In this test the sediment was predominately limestone, rock and coral, some of which can be seen adjacent to the targets in Fig. 2. In the results section of this document, Fig. 44 b-d shows slices of the 3D tomographic reconstruction of a patch of sediment from the test area, illustrating the bathymetric complexity of the environment. Inclement weather prior to the tests caused dynamic currents which reduced platform stability. As in the first test, no strong static currents were present at the test site and large AUV crabbing was not an issue. The additional complexity of the bathymetry, however, played a significant role in algorithm development, which will be discussed in this document.

Targets were deployed in primarily in the proud configuration (i.e. on top of the sediment), however in the first set of scans, partially buried and obliquely buried configurations were used for some targets because the sandy sediment made this a possibility. The target inventory consisted of howitzer shells, a 2 foot by 1 foot diameter solid aluminum cylinder, steel and plastic barrels with the axis positioned vertically (the plastic barrel had a shotput suspended inside to test the visualization of internal features), and additional targets such as a lobster traps (wooden and wire) and a tire. Not all of the circular trajectory scans were performed successfully, in some cases due a navigation error and in some cases due to glitches in the software used to activate sonar signal transmission. Additionally, some targets appeared to have migrated from their originally deployed positions (possibly due to tidal currents) and were completely missed.

FY15 SIGNAL PROCESSING TECHNICAL APPROACH

Coherent multipass synthetic aperture sonar data processing is a challenging task, with difficulties exacerbated by the fact that no reliable absolute positioning methods were available for the utilized AUV systems. Isotropic scatterers can be introduced into the environment for navigation purposes, however this makes the multipass technology impractical. In the analogous field of synthetic aperture radar both GPS and isotropic scatterers are routinely used in similar experiments (see e.g. [3], [4] and [5]).

The primary task of FY15 was to apply the co-registration algorithm developed in FY14 to the experimental multi-pass datasets, make the modifications necessary to make it work reliably in different environments and allow coherent processing of multipass data, and lastly, to estimate the three-dimensional scattering response of targets from the data. The goal data product is a wavenumber representation of the 3D scattering function of a target with minimal phase error, for the purpose of training set generation. The following technical approach was taken to complete the related FY15 tasks:

1. The FY14 co-registration algorithm for AUV data (see FY14 interim report) was applied to the multipass scans from the AUV field tests. A significant number of modifications were made to the FY14 approach, particularly with regard to environmental adaptability, which will be described in subsequent sections.
2. Software was written in Matlab to automate the processing of the multi-pass datasets, allowing a large number of scans to be processed and the robustness of the code tested.
3. Coherent multi-pass data processing techniques were developed to allow uniformly sampled wavenumber and image expressions for the 3D target response to be reconstructed from the gappy and irregularly sampled experimental multipass apertures.

Each of the above steps will be elaborated in subsequent sections, however readers interested in the full technical details will be referred to FY15 papers written by the authors when available.

APPLICATION OF FY14 COREGISTRATION ALGORITHMS TO FY15 FIELD DATA AND SUBSEQUENT MODIFICATIONS

Two major changes were made to the co-registration approach proposed in FY14. The first major change was in how the 3D coordinates for the individual scans were estimated. In FY14 a pseudo-stripmap approach [6] leveraging estimates of range-variant quadratic phase error was used to refine position estimates. In FY15 this approach was replaced with a multilateration [7] because of it’s greater flexibility in environments of complex bathymetry and high currents.

The second major change was the model used for co-registration. It FY14 a coarse-to-fine approach was proposed that modeled multipass height, range, and reference scan altitude errors as variables during data regression. Higher-order effects such as relative platform velocity were not included as variables but incorporated explicitly into the data model. When applied to real data however, the flat sediment assumed in the FY14 model caused severe biasing in the estimated translation parameters. Secondly, medium propagation speed errors were found to be significant in the data. The model was updated to include the effects of bathymetric variability in

the terrain, and the reference scan altitude error variable, (which was replaced because of the presence of onboard interferometry in the SAS system), was swapped out with a medium propagation correction variable.

The first of these changes (multilateration) will be described in detail because even though some similar concepts can be found in [7], a significant number of changes and extensions were applied in the current case to make the algorithm robust and applicable to SAS data. The algorithm has proven to be robust on virtually all the tested CSAS datasets available in the present research effort, but as of yet there is no official documentation for the process besides a non-technical summary in the end-of-year report for ONR project N000141410087.

The second major change, (i.e. the coregistration model change) will only briefly be summarized because the technical details can be found in [2] and [8], papers authored by the principle investigators of the current project that will be appended to this document.

MULTILATERATION

The principle behind multilateration is that the location of a signal source can be estimated by inverting an over-determined system of equations formed from the relative positions of, and time delays to, a set of receivers. In [7] it was shown that measurements of circular SAR focusing aberrations at a series of dispersed control points can be related by the multi-lateration principle to aperture coordinate errors in three dimensions. The current research has extended the ideas in [7] to make the navigation inversion more robust by adding appropriate regularization and adaptive weighting schemes to the navigation error inversion process, as well as altering how the phase aberrations are measured. Additionally, the algorithm was extended to handle the high crab-angles encountered by SAS systems, large uncertainties in the initial vehicle altitude relative to the sediment, and relative height errors between the scene control points, the location of which were automated.

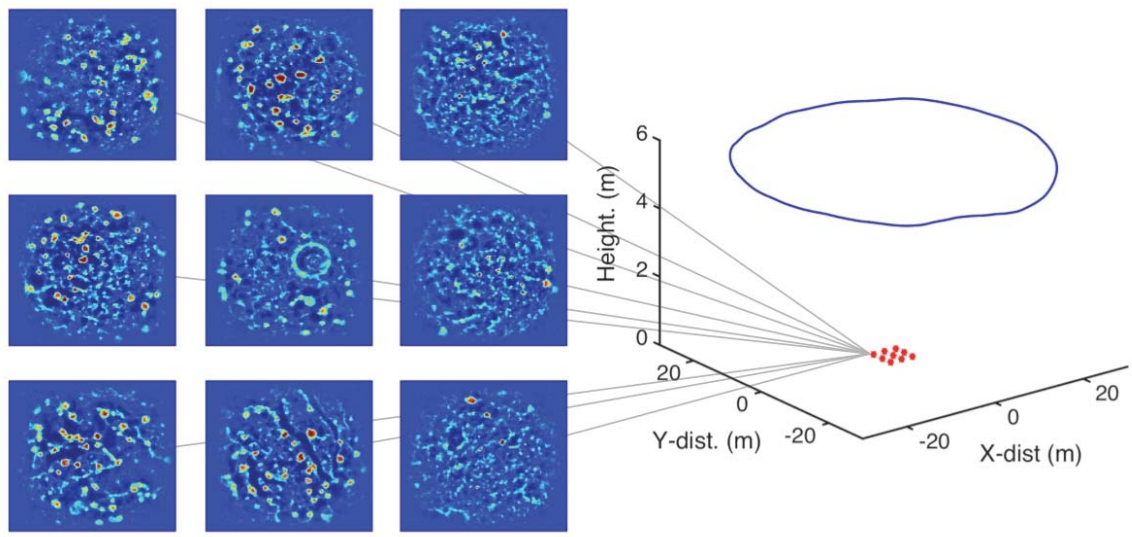

Figure 3. An example scan showing the flight path of the AUV in Cartesian coordinates (right figure, blue line) and the location of the test-patches used for multilateration (right figure, red dots). The image snippets at left correspond to the test-patches.

The multilateration principle is applied to circular synthetic aperture sonar data in the following manner. A series of *N* patches with pre-determined locations relative to the circular scan origin are selected. The center of the patches have the coordinates: $\left[r_p^{(1\ldots N)},\ h_p^{(1\ldots N)}, \theta_p^{(1\ldots N)}\right]$, where it is initially assumed $h_p^{(1\ldots N)}$, the height of the patches, are zero. In the present case, nine patches are used and arranged in a square grid around the coordinate origin as shown in Fig. 3. Using sub-aperture based autofocusing (see e.g. [7], [9]) each test-patch is autofocused and the point-spread functions are found, as shown in Fig. 4.

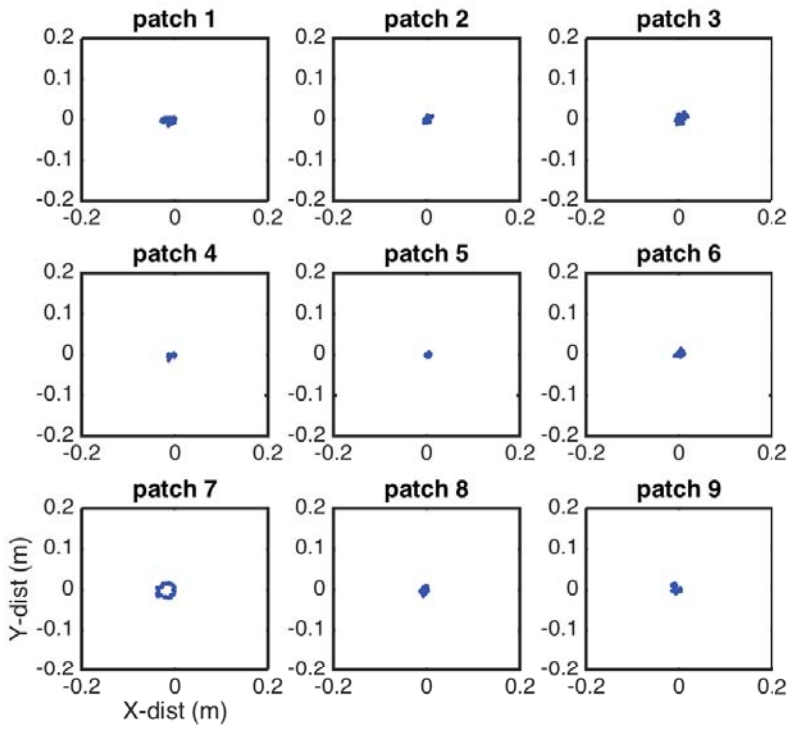

Figure 4. The point-spread functions of the individual test patches, estimated via application of an autofocusing routine.

The result of the autofocusing operation is a delay error (related to range, or position error) between each patch and each portion of the scan, i.e. for the nth focusing patch the correction function ϕ_n expresses the phase error as a function of the distance error between the nth test patch and the sonar when the sonar is at some angle θ relative to the aperture origin:

$$\phi_n(\theta) = e^{j2kd_n(\theta)}. \tag{1}$$

In (1) k is acoustic wavenumber $2\pi f_0/c$, f_0 is the center frequency of the sonar in Hz, c is the sound-speed in m/s, and $d_n(\theta)$ is the distance error in meters between the nth patch and the sonar platform when nominally at the angular location θ. A fundamental ambiguity exists, however, in the estimation for $d_n(\theta)$ found via autofocus: the focus of the patch is translation independent [9]. This ambiguity manifests as an undetermined first-order sinusoid with arbitrary amplitude and phase that can be added to the distance function:

$$\phi_n(\theta) = e^{j2k(d_n(\theta)+A\cos(\theta+B))}\ . \tag{2}$$

When applied as a correction function to the nth patch, eq. (2) with arbitrary values for A and B will have the exact same focusing effect as eq. (1). To overcome this difficulty the local aperture curvature, which is translation invariant, is calculated from $d_n(\theta)$:

$$\check{d}_n(\theta) = d_n(\theta) + \ddot{d}_n(\theta), \tag{3}$$

where $\check{d}(\theta)$ represents the curvature of the phase solution at θ and $\ddot{d}_n(\theta)$ is the second derivative of $d_n(\theta)$. The sign flip in the second derivative causes the sinusoidal term to drop out of $\check{d}(\theta)$. The originally assumed distance between the aperture point at θ and the nth test-patch is:

$$\widetilde{D}_n(\theta) = \sqrt{\left(r_s(\theta)\right)^2 + \left(r_p^{(n)}\right)^2 - 2r_s(\theta)r_p^{(n)}\cos\left(\theta - \theta_p^{(n)}\right) + \left(h_s(\theta) - h_p^{(n)}\right)^2}\,, \quad (4)$$

where $r_p^{(n)}$ and $h_p^{(n)}$ are the radial distance and height of the center of the nth patch relative to the polar origin and $\theta_p^{(n)}$ is the polar angle to the patch. The values $r_s(\theta)$ and $h_s(\theta)$ are the radial distance and height of the sonar relative to the polar origin when the sonar is at the angular location θ, and $\widetilde{D}_n(\theta)$ is the distance of the sonar to the center of the nth patch. For cylindrical coordinate positional errors Δr_s, Δh_s and $\Delta\theta$ the distance error $d_n(\theta)$ to the nth patch can be expressed:

$$d_n(\theta) = \widetilde{D}_n(\theta) - \ \ldots \quad (5)$$

$$\ldots \sqrt{\left(r_s(\theta) + \Delta r_s(\theta)\right)^2 + \left(r_p^{(n)}\right)^2 - 2\left(r_s(\theta) + \Delta r_s(\theta)\right)r_p^{(n)}\cos\left(\theta + \Delta\theta(\theta) - \theta_p^{(n)}\right) + \left(h_s(\theta) + \Delta h_s(\theta) - h_p^{(n)}\right)^2}$$

This is a non-linear function, however the perturbations in the function are expected to be slight because the values for $\Delta r_s(\theta)$, $\Delta h_s(\theta)$, and $\Delta\theta(\theta)$ will be small. Linearizing around the variables gives:

$$d_n(\theta) \cong \zeta_r(\theta, n)\Delta r_s(\theta) + \zeta_h(\theta, n)\Delta h_s(\theta) + \zeta_\theta(\theta, n)\Delta\theta(\theta), \quad (6)$$

$$\zeta_r(\theta, n) = \frac{r_s(\theta) - r_p^{(n)}\cos\left(\theta - \theta_p^{(n)}\right)}{\widetilde{D}(\theta)}\,, \quad (7)$$

$$\zeta_h(\theta, n) = \frac{h_p^{(n)} - h_s(\theta)}{\widetilde{D}(\theta)}\,, \quad (8)$$

$$\zeta_\theta(\theta, n) = \frac{r_p^{(n)} r_s(\theta)\sin\left(\theta - \theta_p^{(n)}\right)}{\widetilde{D}(\theta)}\,. \quad (9)$$

Following linearization, the error variables $\Delta r_s(\theta)$, $\Delta h_s(\theta)$, and $\Delta\theta(\theta)$ can be related to the curvature measurement vectors $\check{d}_n(\theta)$ in standard linear format:

$$Ax = b, \quad (10)$$

where, using eq. (3) and eq. (6), A can be expressed:

$$A = \begin{bmatrix} \check{I}\mathrm{Z}_r(\theta, 1) & \check{I}\mathrm{Z}_h(\theta, 1) & \check{I}\mathrm{Z}_\theta(\theta, 1) \\ \vdots & \vdots & \vdots \\ \check{I}\mathrm{Z}_r(\theta, N) & \check{I}\mathrm{Z}_h(\theta, N) & \check{I}\mathrm{Z}_\theta(\theta, N) \end{bmatrix} \quad (11)$$

$$\breve{I} = I + \frac{\ddot{I}}{\delta\theta} \tag{12}$$

where I is an $M \times M$ difference matrix and M is the length of the vector of angles θ, $\ddot{I}$ is the second-order difference matrix, $\delta\theta$ is the angular sample spacing of the vector θ, and $\mathrm{Z}_{r,h,\theta}(\theta, n)$ is a matrix with the only non-zero values being the main diagonal, which has as entries the values of the bases functions $\zeta_{r,h,\theta}(\theta, n)$. A is therefore an $NM \times 3M$ sized matrix. The values of the NM × 1 measurement vector b are:

$$b = \begin{bmatrix} \breve{d}_1(\theta) \\ \vdots \\ \breve{d}_N(\theta) \end{bmatrix} \tag{13}$$

where each $\breve{d}_n(\theta)$ is an $M \times 1$ column vector of curvature error estimates computed from the estimated phase errors via eq. (3). The solution vector x is the $3M \times 1$ column vector of the unknown M-length error vectors $\Delta r_s(\theta)$, $\Delta h_s(\theta)$, and $\Delta\theta(\theta)$:

$$x = \begin{bmatrix} \Delta r_s(\theta) \\ \Delta h_s(\theta) \\ \Delta\theta(\theta) \end{bmatrix} \tag{14}$$

The formulation of the inverse problem thus far is sufficient for cases in which the heights of the patches $h_p^{(1\ldots N)}$ are known or assumed to be zero. In the present case, due to bathymetric variability, making $h_p^{(1\ldots N)}$ a set of unknown variables in the solution vector is necessary, however the coupling between $h_p^{(1\ldots N)}$ and the other variables in the solution vector causes the equation to be nonlinear requiring an iterative solution. In the present case an initial estimate $h_{p_0}^{(1\ldots N)}$ is used in the calculation of the bases functions of eq. (6-8). The measurement vector remains the same but A is redefined as follows:

$$A = \begin{bmatrix} \breve{I}\mathrm{Z}_r(\theta,1) & \breve{I}\mathrm{Z}_h(\theta,1) & \breve{I}\mathrm{Z}_\theta(\theta,1) & \mathrm{H}_p(\theta,1) & 0 & \vdots \\ \vdots & \vdots & \vdots & 0 & \mathrm{H}_p(\theta,n) & 0 \\ \breve{I}\mathrm{Z}_r(\theta,N) & \breve{I}\mathrm{Z}_h(\theta,N) & \breve{I}\mathrm{Z}_\theta(\theta,N) & \vdots & 0 & \mathrm{H}_p(\theta,N) \end{bmatrix}, \tag{15}$$

where:

$$\mathrm{H}_p(\theta, n) = \breve{I}\frac{h_{p_0}^{(n)} - h_s(\theta)}{\tilde{D}(\theta)}, \tag{16}$$

which is an $M \times 1$ vector, making the new dimensions of A equal to $MN \times (3M + N)$ and the solution vector correspondingly a $(3M + N) \times 1$ vector:

$$x = \begin{bmatrix} \Delta r_s(\theta) \\ \Delta h_s(\theta) \\ \Delta\theta(\theta) \\ h_p^{(1)} \\ \vdots \\ h_p^{(N)} \end{bmatrix} \tag{17}$$

It can be noticed that there are two linear dependencies within the solution vector values: a non-zero average value for the vector $h_p^{(1\ldots N)}$ is identical to an average downward shift of the array. Similarly, a planar tilt of the patches is identical to a planar tilt of the array, which for small angles can very nearly be simulated by a first-order sinusoidal height term around the array. These problems can be fixed by adding appropriate regularization to penalize solutions for $h_p^{(1\ldots N)}$ that have an average offset or planar tilt:

$$x = (A^T A + \lambda_1 \Gamma_1^T \Gamma_1 + \lambda_2 \Gamma_2^T \Gamma_2 \ldots)^{-1} A^T b \ , \tag{18}$$

where $\Gamma_{1,2\ldots}$ are a series of $(3M + N) \times (3M + N)$ regularization matrices designed to penalize the offset and planar tilt components of $h_p^{(1\ldots N)}$, or additionally to penalize large values for $\Delta r_s(\theta)$, $\Delta h_s(\theta)$, and $\Delta\theta(\theta)$. In the current multilateration version, the following regularization matrices are employed:

$$\Gamma_1 = \begin{bmatrix} \overbrace{0 \quad 0 \quad \cdots \quad\quad\quad\quad}^{3M} & \overbrace{\cdots \quad\quad 0}^{N} \\ 0 \quad 0 & \\ \vdots \quad\quad \ddots & \vdots \\ \quad\quad\quad\quad 0 & \\ \vdots & 1 \quad \cdots \quad 1 \\ & \vdots \quad \ddots \\ 0 \quad \ldots \quad\quad \ldots & 1 \quad\quad 1 \end{bmatrix} \tag{19}$$

and

$$\Gamma_2 = \begin{bmatrix} \overbrace{1 \quad 0 \quad \cdots \quad\quad\quad\quad}^{3M} & \overbrace{\cdots \quad\quad 0}^{N} \\ 0 \quad 1 & \\ \vdots \quad\quad \ddots & \vdots \\ \quad\quad\quad\quad 1 & \\ \vdots & 0 \quad \cdots \quad 0 \\ & \vdots \quad \ddots \\ 0 \quad \ldots \quad\quad \ldots & 0 \quad\quad 0 \end{bmatrix} \tag{20}$$

The dimensions of each sub-portion of the matrices are shown via the braces above. Γ_1 penalizes the average of the solution for $h_p^{(1\ldots N)}$, and Γ_2 penalizes large values for $\Delta r_s(\theta)$, $\Delta h_s(\theta)$, and $\Delta\theta(\theta)$. In both cases $\Gamma = \Gamma^T \Gamma$ and the total regularization is:

$$\lambda_1\Gamma_1^T\Gamma_1 + \lambda_2\Gamma_2^T\Gamma_2 = \begin{bmatrix} \overbrace{\begin{matrix} \lambda_2 & 0 & \cdots & \\ 0 & \lambda_2 & & \\ \vdots & & \ddots & \\ & & & \lambda_2 \end{matrix}}^{3M} & \overbrace{\begin{matrix} \cdots & 0 \\ & \\ & \vdots \\ & \end{matrix}}^{N} \\ \begin{matrix} \vdots & & & \\ 0 & \dots & \dots & \end{matrix} & \begin{matrix} \lambda_1 & \cdots & \lambda_1 \\ \vdots & \ddots & \\ \lambda_1 & & \lambda_1 \end{matrix} \end{bmatrix}. \tag{21}$$

A last modification to the inversion process is the addition of an adaptive weighting factor $w_{1\dots N}(\theta)$ to weight the level of influence each curvature measurement in $\check{d}_{1\dots N}(\theta)$:

$$x = (A^T(A \circ W) + \lambda_1\Gamma_1^T\Gamma_1 + \lambda_2\Gamma_2^T\Gamma_2 \dots)^{-1}(A \circ W)^T b\ , \tag{22}$$

$$W = \begin{bmatrix} \overbrace{\begin{matrix} w_1(\theta) & w_1(\theta) & \cdots & w_1(\theta) \\ \vdots & \vdots & & \vdots \\ w_N(\theta) & w_N(\theta) & \cdots & w_N(\theta) \end{matrix}}^{3M+N} \end{bmatrix}, \tag{23}$$

where $\circ$ is the Hadamard product and W is a matrix the same size as A but in which each column is identically the concatenated set of weighting values $w_{1\dots N}(\theta)$ for the curvature entries. This weighting matrix greatly improves performance because it has been observed that, especially when partial occlusions of the image patches occur, the quality of the curvature estimates for each value of θ are not uniform. The weighting matrix reduces or eliminates the contributions to the error variable estimates of these lower-quality regions, while emphasizing the higher quality entries. The optimal method for determining the weights $w_{1\dots N}(\theta)$ has not yet been found but some alternatives are to estimate the values during the autofocusing procedure, or, as is done currently, iteratively estimate them using the residual between the data and it's least-squares model, i.e. initialize $w_{1\dots N}(\theta)$ to uniform values of 1 for all measurements and iterate the following:

$$w_{1\dots N}^{(k)}(\theta) = \frac{\epsilon}{(b - A\tilde{x}_{k-1})^2 + \epsilon}, \tag{24}$$

where ϵ is an anomaly rejection parameter that, for decreasing values, increasingly rejects measurement samples with a high distance from the modeled values reconstructed from the least-squares estimates (represented by the squared term in the denominator of eq. (24)).

It has been observed that the effect of the weighting regularization matrix is altered by the values in W, i.e. for small values of W the effect of the weighting matrix is exacerbated. If values for ϵ are set sufficiently large to prevent W from becoming sparse this doesn't become a problem, however future work would be to find a balancing term to keep the effect of the regularization matrix uniform despite the changing values of W.

This 3D coordinate inversion process is implemented in an iterative framework that can be summarized in the following steps:

1. A set of small image patches are beamformed
2. The image patches are autofocused and a set of aperture curvature errors are computed via eq. (3) from the phase solution.
3. Eq. (22) is used to compute aperture coordinate refinement estimates in an iterative re-weighted framework that adaptively estimates W via eq. (24).
4. The coordinates are updated.
5. Steps 1 – 4 are repeated a set number of times or until a convergence criterion is met.

In the currently implemented version, patches that have overwhelmingly low weights, perhaps due to occlusion over most of the aperture, are re-positioned in effort to generate higher quality data for coordinate inversion. Furthermore, the second order derivative in (3) causes the curvature solutions to be predominantly high frequency. The least-squares solutions can converge slowly for low-frequency blur-causing errors, an additional set of vectors that are essentially low-pass filtered are introduced in the solution vector b to keep the solution from de-emphasizing low-frequency corrections.

Several iterations of multilateration algorithm were applied to the data set used to generate Fig.'s 3 and 4 and the coordinate updates in the radial, height, and angular dimensions are plotted in Fig. 5.

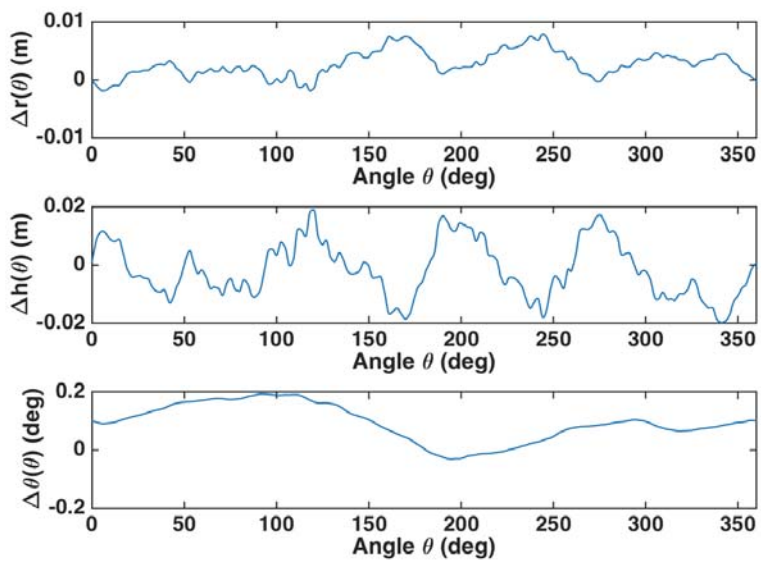

Figure 5. The radial, height, and angular corrections that are estimated from the iterated multi-lateration process and applied to the 3D coordinates of the SAS sonar platform.

The point-spread functions have improved considerably, as shown in Fig. 6. (The originals are shown for comparison.)

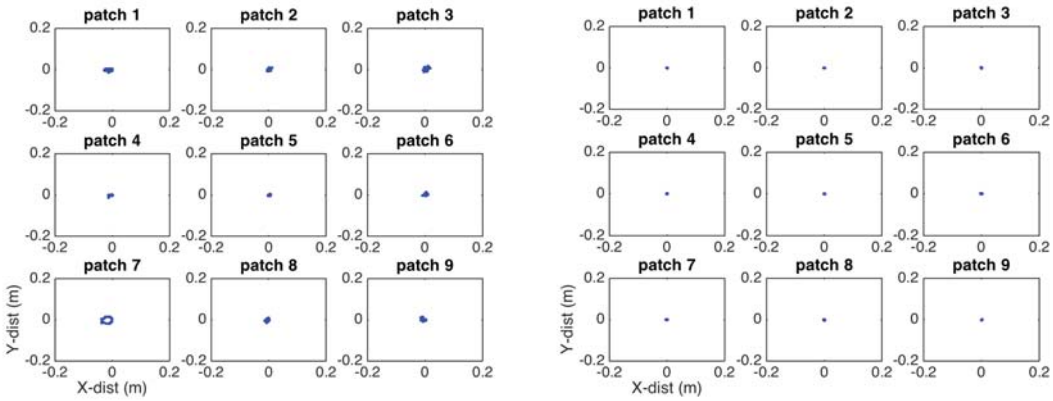

Figure 6. The original point-spread functions (L) and point-spread functions after the coordinate updates (R).

The beamformed image, autofocused via multilateration, is shown in Fig. 7.

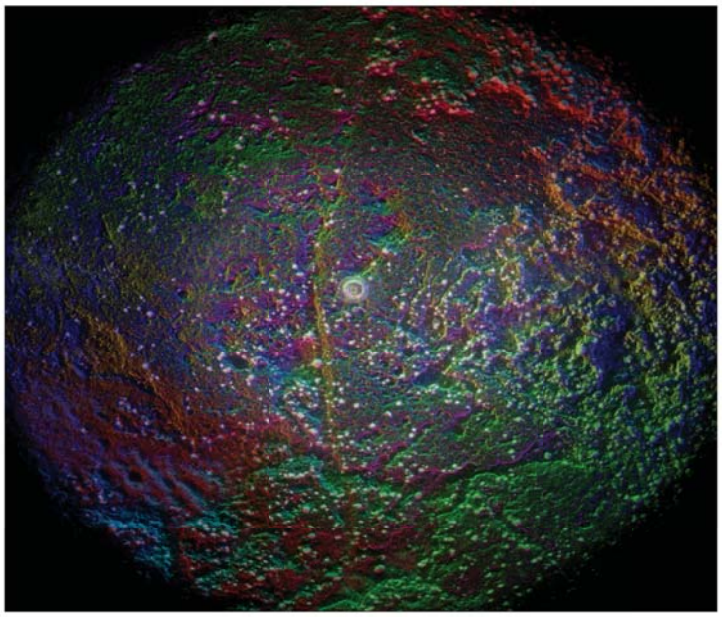

Figure 7. CSAS image of a proud, vertically oriented plastic barrel on a limestone and coral sediment. Focus is achieved throughout the image excepting out-of-plane regions, in which case defocusing is due to being out of plane.

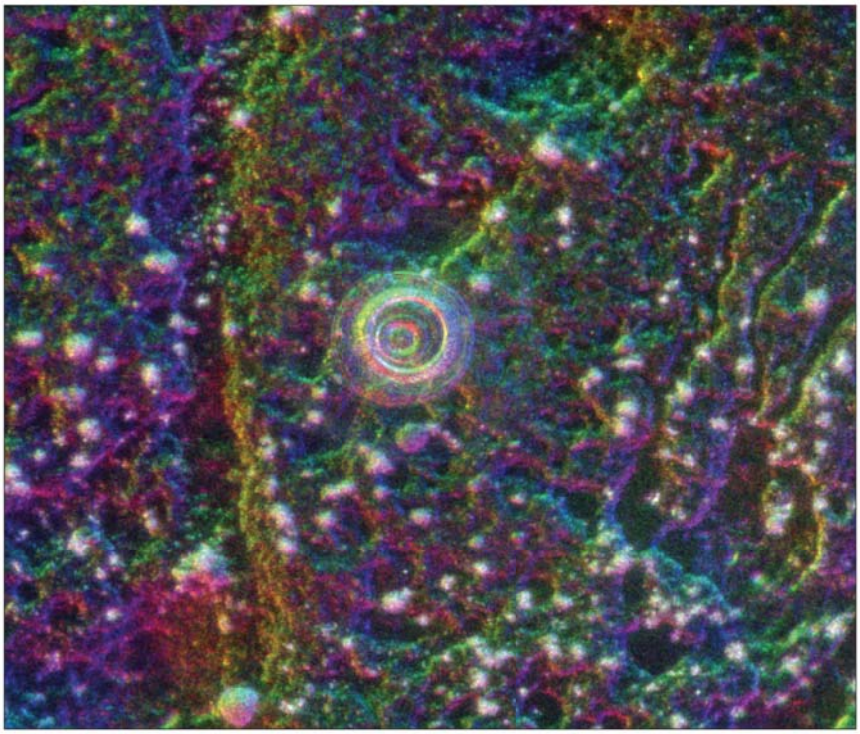

Figure 8. Zoomed in section of Figure 7 showing the barrel.

Multiple methods exist for autofocusing the individual patches during the multi-lateration process. Examples include the generalized cone approach described in [9], the differential aperture approach described in [10], or the cumulative sum algorithm described in [7]. The current implementation uses a modification to the cumulative sum algorithm described in [7], however the authors currently believe that some improvement could be attained by combining this approach with one of the other approaches because the data products of the algorithms in [9] and [10] are, directly, the aperture curvature function and have better noise characteristics. In contrast, the cumulative sum approach described in [7] tends to result in noisier curvature measurements but relies less on integration and functions well through occlusions.

As a final note, in the currently implemented approach a single-patch algorithm of the type described in [9] is applied to the beam center of the image over a large image patch (where it can be noted that, as previously discussed in the FY14 interim report [10], the center of insonification can vary from the center of the circle due to static currents and oscillatory vehicle crabbing). The purpose of this process is to provide a bulk correction that removes large-scale curvature errors, reducing the point-spread function size and allowing smaller patches to be used for multi-lateration. This step is not necessary, but by allowing the patch sizes in the multi-lateration algorithm to be reduced the recovered autofocusing solutions are averaged over a smaller area, improving accuracy and also increasing the speed of the routine.

COREGISTRATION MODEL CHANGES

In FY14 the proposed model for co-registration was the following:

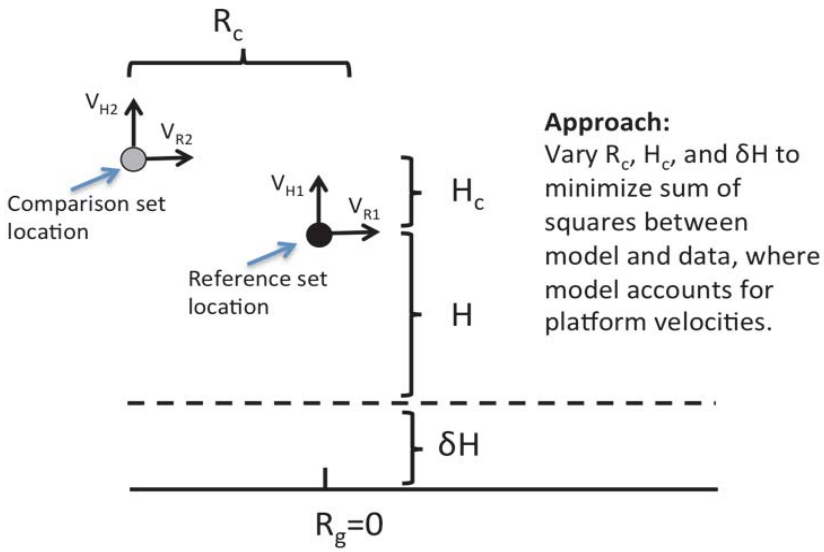

Figure 9. FY14 SAS multipass coregistration model.

The variables in the FY14 model, as depicted in Fig. 9, are the height H_c and radial R_c differences between the reference and comparison sets as well as a general model error for the height of the sonar above the sediment, δH. The system used in FY15 is interferometric (and, even if not, an alternative method for arriving at δH using entropy maximization can be used as a substitute, which will be discussed later), which meant that a sufficiently accurate estimate for the height of the reference set above the sediment can be assessed prior to co-registration. The updated FY15 model, which can be found in [2] and shown in Fig. 10, is:

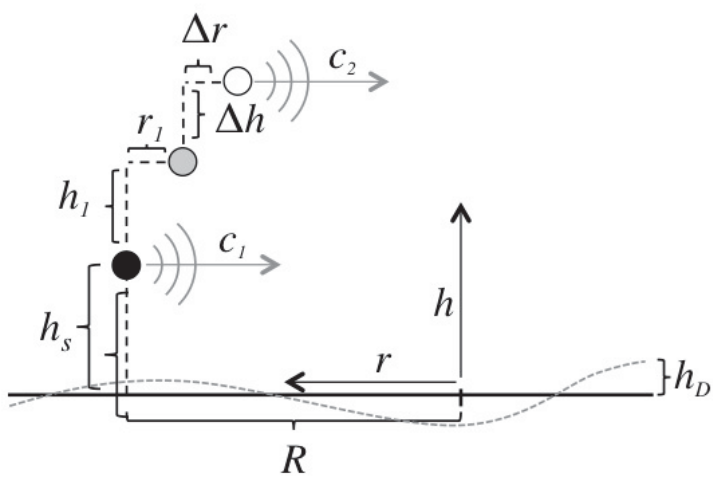

Figure 10. FY15 AUV-scan coregistration model. The parameters are h_s: the height of the reference sonar above the nominal ground-plane, h_1: the initial vertical baseline estimate between the reference and comparison scan, Δh: the vertical baseline error, R: the radial location of the reference scan, r_1: the initial radial baseline estimate, Δr: the radial error variable, c_1: the reference sound-speed, c_2: the sound speed of the medium at the time the second scan is taken and lastly h_D: the sediment height relative to the nominal ground-plane. Lowercase r denotes the coordinate radial direction, and lowercase h represents the coordinate vertical direction.

Significant changes include the assumption of initial radial and height baselines r_1 and h_1, (initialized as the nominal radial and/or height difference between scans programmed into the vehicle objective), the reformulation of the location of the origin at the center of the cylindrical coordinate system, the inclusion of the bathymetry h_D, and a new variable, c_2, an independent sound-speed for the comparison scan. Presumably, c_2 should not vary significantly between scans, however due either to inaccuracies and drift in the onboard CTD or inhomogeneities in the water column, the average sound speeds measured at each scan varied enough to bias localization estimates between scans if left unaccounted. Unlike the FY14 model, the FY15 model did not include velocity terms because the relative platform velocities between scans did not vary significantly enough in the tested datasets to warrant their inclusion. For completeness, however, the model may be updated in FY16, especially if scans in environments with high velocity oscillatory currents (from wave action, etc.) are conducted.

To summarize the new co-registration process, both the reference and comparison scan data sets are interpolated to the nominal ground-plane height $h = 0$, and interpolated as well to a uniform grid in the angular dimension, allowing coherent comparison between scans. These scans are then patch-wise correlated to generate a set of data products, which include complex phases, coherence measurements, and displacement measurements in units of meters. The displacements are found using the phase and locations of the correlation peaks. Examples of these data products are shown in in Fig. 11:

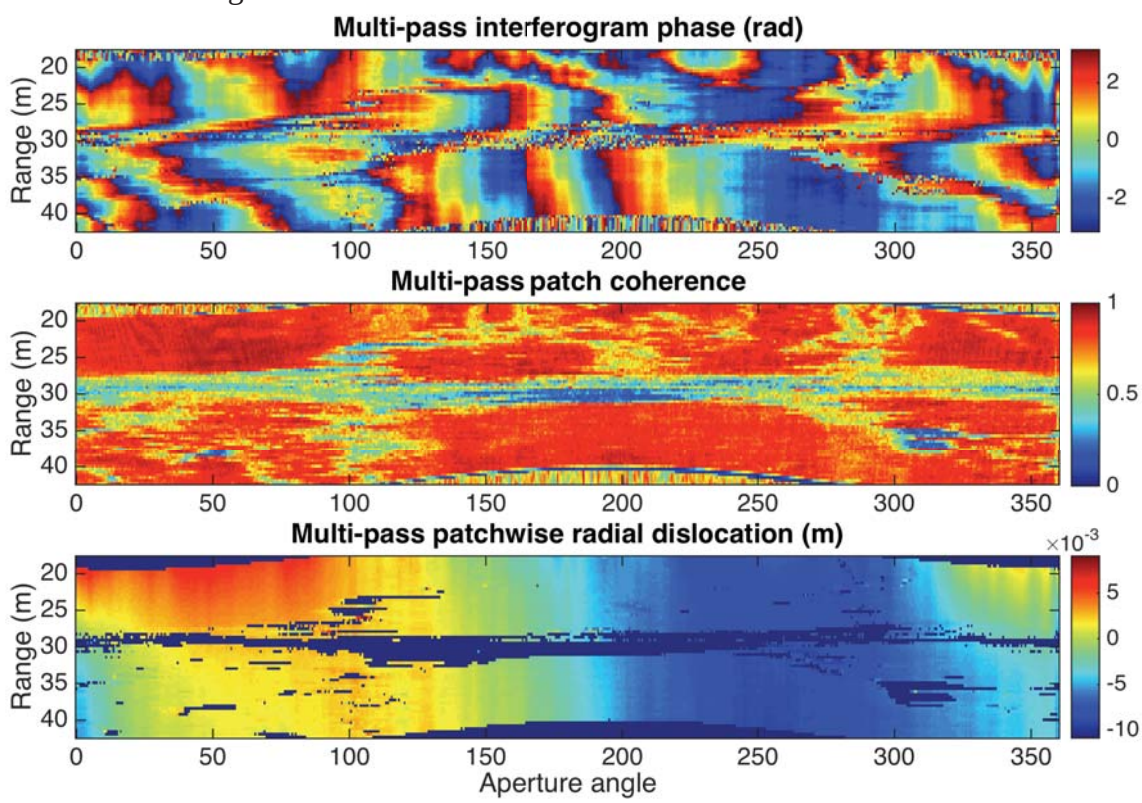

Figure 11. Top: phase measurements produced by patch-wise correlation. Middle: correlation coefficients for the patches. Bottom: radial displacement estimates measured by combining the phase estimates with coarse dislocation estimates found using the correlation peaks.

Regression is used to fit the displacement map in Fig. 11 to a set of bases functions. The derivation and linearization of the mathematical model associated with the displacement map in Fig. 11 can be found in Sec. IIIB of [2], and the final linearized description of the model, expanded around initial error estimates Δr, Δh, and σ (where $\sigma = c_1/c_2 - 1$) is:

$$\rho_{cor}(r_g) \approx \psi + \psi_0 + \zeta_{\Delta r}(r_g)(\Delta r - \Delta r_0) + \zeta_{\Delta h}(r_g)(\Delta h - \Delta h_0) + \zeta_{\sigma}(r_g)(\sigma - \sigma_0)\ , \tag{25}$$

$$\zeta_{\sigma}(r_g) = \frac{(r_g + r_1 + \Delta r_0)^2 + (h_S - h_d(r_g) + h_1 + \Delta h_0)^2}{\psi_0}\ , \tag{26}$$

$$\zeta_{\Delta r}(r_g) = \frac{(r_g + r_1 + \Delta r_0)(1 + 2\sigma_0)}{\psi_0}\ , \tag{27}$$

$$\zeta_{\Delta h}(r_g) = \frac{(h_S - h_d(r_g) + h_1 + \Delta h_0)(1 + 2\sigma_0)}{\psi_0}\ , \tag{28}$$

$$\psi(r_g) = \sqrt{r_g^2 - 2h_S h_d(r_g) + h_d(r_g)^2} + r_1, \tag{29}$$

$$\psi_0(r_g) = -\sqrt{(1 + 2\sigma_0)\left((r_g + r_1 + \Delta r_0)^2 + (h_S - h_d(r_g) + h_1 + \Delta h_0)^2\right) - (h_S + h_i)^2}\ . \tag{30}$$

In eq. (25) – (30), $\rho_{cor}(r_g)$ is the residual radial displacement at some aperture location (experimentally corresponding a column from the displacement data at the bottom of Fig. 11), $\zeta_{\Delta r,\Delta h,\sigma}$ are the bases vectors, ψ and ψ_0 are terms that become important when the expansion is not around zero, and the other terms are explained in the caption of Fig. 10. Regression begins by initializing Δr_0, Δh_0, and σ_0 to zero, (in which case ψ and ψ_0 cancel), and performing a weighted least-squares fit with the bases functions:

$$\begin{bmatrix} \Delta\tilde{r} \\ \Delta\tilde{h} \\ \tilde{\sigma} \end{bmatrix} = \left(\begin{bmatrix} \zeta_{\Delta r} \\ \zeta_{\Delta h} \\ \zeta_{\sigma} \end{bmatrix} \cdot \begin{bmatrix} (w \circ \zeta_{\Delta r})^T & (w \circ \zeta_{\Delta h})^T & (w \circ \zeta_{\sigma})^T \end{bmatrix} \right)^{-1} \cdot \begin{bmatrix} (w \circ \zeta_{\Delta r})^T \\ (w \circ \zeta_{\Delta h})^T \\ (w \circ \zeta_{\sigma})^T \end{bmatrix} \cdot \rho_{cor}^T, \tag{31}$$

where w is the weighting function for the data, (determined via the patch correlation coefficients), $\circ$ is the Hadamard product, superscript ^{T} represents the transpose operator and $\Delta\tilde{r}$, $\Delta\tilde{h}$, and $\tilde{\sigma}$ are the error values fitted from the ith row of radial displacements.

Following initial data fitting the estimates of the error values determine the new expansion points, i.e. $\Delta r_0 = \Delta\tilde{r}$, $\Delta h_0 = \Delta\tilde{h}$, and $\sigma_0 = \tilde{\sigma}$. Using these new values the bases are recalculated and eq. (31) is re-evaluated. A full technical description of the process is described in Section IIIB of [2], which includes methods for adaptively determining the values of the weighting function w as well as methods for coupling the estimates from adjacent aperture points to allow additional information about the likelihood of the behavior of the SAS platform to inform the estimates for the error variables and the weights.

The inclusion of bathymetric data into the regression process in the FY15 model is a major advantage over the FY14 process, which assumed a flat sediment. To illustrate, the displacement data in Fig. 10 was fit using both the flat bottom assumption in one case and in another case the full FY15 model that incorporates bathymetry. In Fig. 12, the data is shown (Fig. 12, top left) along with the surface reconstructions for the data generated using the bases that assume a flat bottom or incorporate bathymetry. Furthermore, the residual errors between the dataset and the individual models are shown for both instances as well.

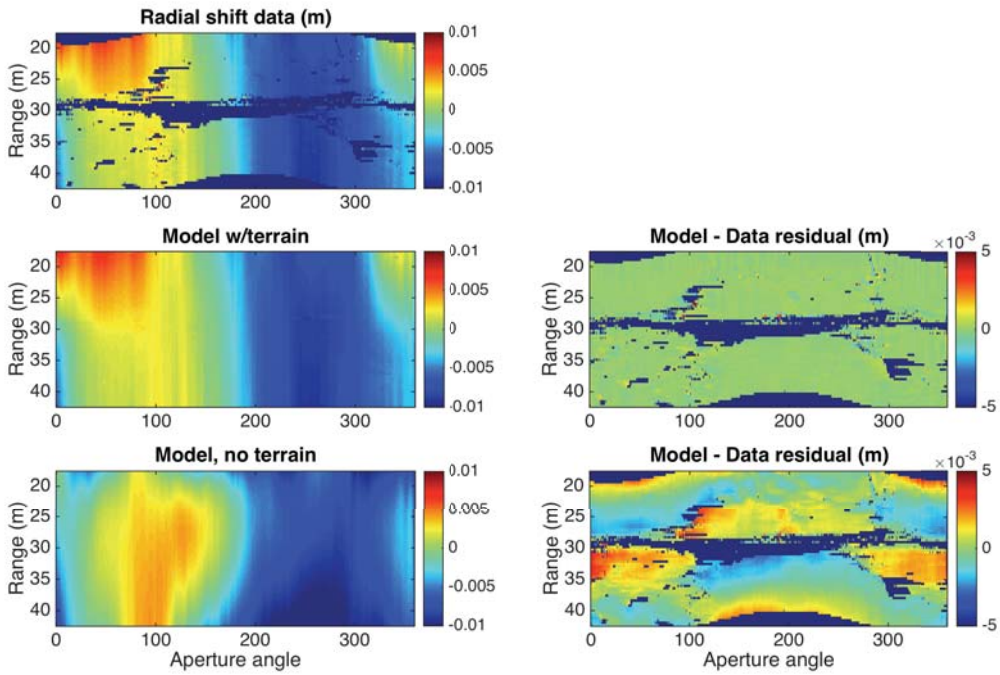

Figure 12. Top left: Original displacement data estimated via patch-wise correlation. Middle left: the displacement surface, reconstructed using the bases functions and estimated error parameters for the FY15 model incorporating bathymetry. Bottom left: the displacement surface, reconstructed using the bases functions and estimated parameters for a flat-bottom assumption. Middle right: the model – data residual for the FY15 model. Bottom right: the residual error for the flat-bottom model. The color scale is in meters.

The contrast between the methods is stark: the residual for the model incorporating bathymetry is much smaller. Qualitatively, the model generated by the parameter fits also appears much more like the original data (compare the middle left and top left images in Fig. 12). The difference also manifests in the estimated error parameters, which are shown in Fig. 13.

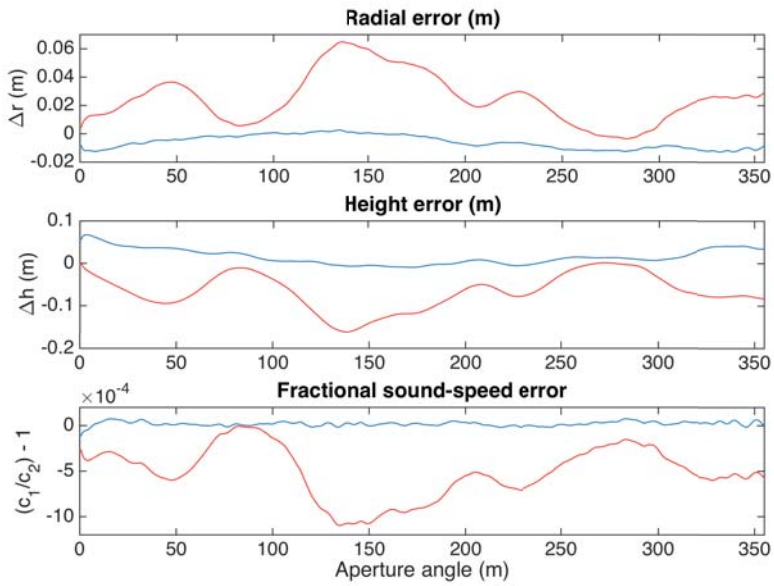

Figure 13. The estimated error parameters for the full FY15 model (blue) and the flat-bottom model (red).

Not only are the estimated parameters very different, but also the standard deviations of the flat-bottom estimates are much higher:

	Model w/bathymetry	Model, flat bottom
Δr, standard dev.	0.47×10^{-2}	1.76×10^{-2}
Δh, standard dev.	1.84×10^{-2}	4.22×10^{-2}
σ, standard dev.	0.24×10^{-4}	2.82×10^{-4}

Table 1. Standard deviations of the vectors of the estimated parameters for the models incorporating bathymetry verses assuming a flat bottom.

The fact that a model of one form gives both a lower residual and simultaneously produces a series of coefficients across all samples that are less complex is indicative of a better model. The contrast is especially apparent in the case of the standard deviation of the estimated sound-speed bias, which has been reduced by over an order of magnitude.

Finally, the inclusion of terrain into the coregistration process prevents coregistration and aperture localization errors from propagating throughout the array and biasing the locations of the aperture coordinates. This affects the measurements of the estimated grazing angle and the coherent processing of the data, which is illustrated in Fig. 14.

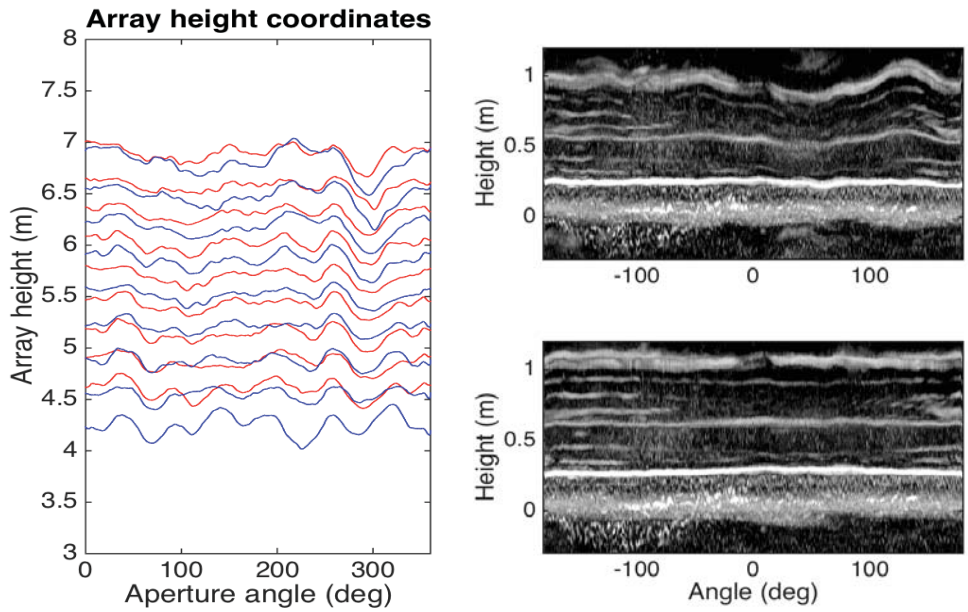

Figure 14. Left: array localization results using the flat-bottom model (blue) vs. incorporation of bathymetry (red). Right: the range-projected vertical beamforming results for the case in which a flat-bottom is assumed (top) vs. incorporation of bathymetry (bottom).

The final result has a big effect on the coherently synthesized estimate for the vertical scattering profile of a target, and correspondingly, the angle of incidence between each scan and the target.

One may reasonably ask why, given the size of the errors, beamforming is even possible in the flat-bottom case. The reason is that the flat-bottom assumption causes a systematic error that roughly affects all aperture coordinates at a given angle θ equally, i.e. the array is expanded or contracted. Rather than adding phase noise, this causes a contraction or expansion in the height dimension of the vertically beamformed image, as is clearly visible in the top right image of Fig. 14.

More details on the coregistration process, as well as the effect of bathymetry on the multipass aperture synthesis can be found in Section III of [2] as well as [8], both of which have been appended to this report.

ROLL AND HEAVE CALIBRATION

In the previous section it was shown that bathymetry estimates can be used to greatly increase the accuracy of the localization process. In the current system, these bathymetric priors are generated using interferometry; however, interferometry can be biased by platform height, roll, or sound-speed errors. These errors propagate to the localization estimates.

It has been noted previously that circular scans have an inherent level of vertical resolution for small scatterers [12], [13]. For the same reason, traditional line-scan SAS with heavy non-

linearities can have bathymetry dependent focus [14], [15]. This is illustrated in the Fig. 15, in which CSAS images focused to different height planes are compared.

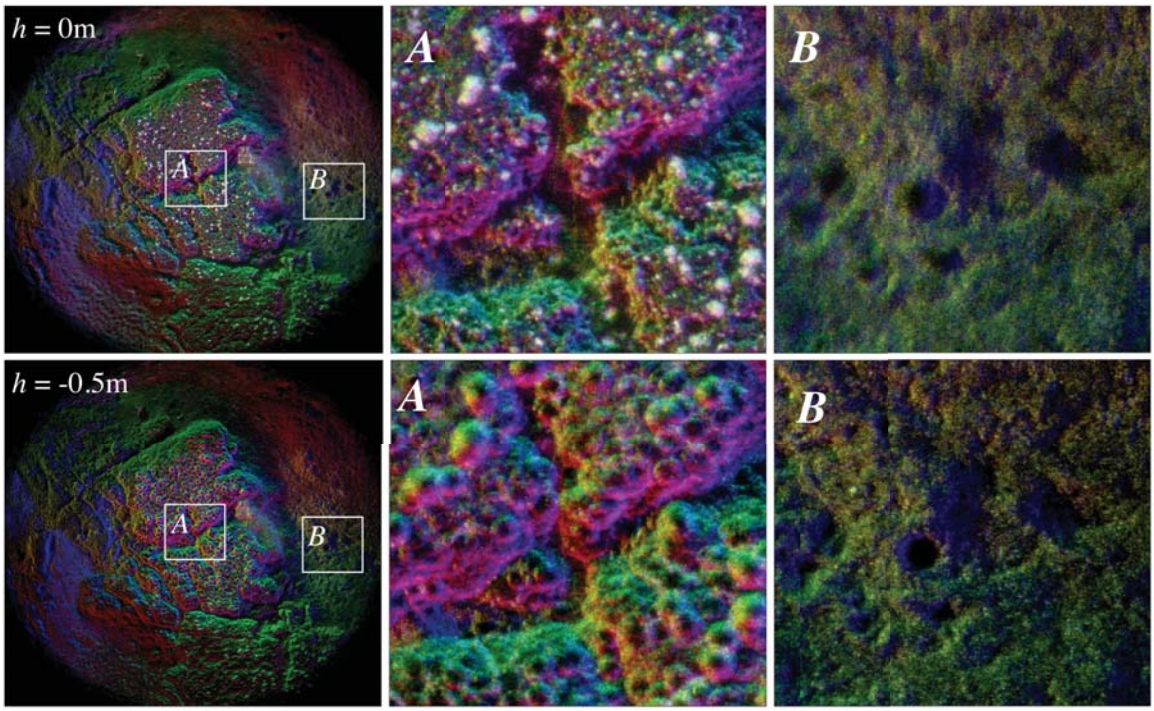

Figure 15. Illustration of out-of-plane defocusing for CSAS images. The left column shows a scene imaged at two focusing planes: a plane corresponding to the height of the rocky outcropping and a plane corresponding to the adjacent sandy sediment. The insets labeled *A* and *B* show the relative focus of these patches for the different focusing planes: in the top row, patch *A* is in focus while patch *B* is not. For the bottom row the focus is reversed.

In the current research effort, these properties are exploited to generate an alternative bathymetry map that can be used to calibrate the interferometer. To generate a non-interferometric bathymetry map a CSAS image is generated by backprojecting CSAS data to a height-plane equivalent to the average estimated height of the sediment relative to the circular scan. The complex image is sub-divided into a series of small squares, and phase transformations in wavenumber space simulating height-plane changes are applied for a series of heights. The height-plane that minimizes the entropy (alternatively, maximizes the contrast) of the image patch is selected as the true height of the patch. In the current research effort his height estimate is called the “entropic” estimate. An advantage of the entropic approach is that it is inherently insensitive to roll error and oscillatory height errors in the sonar platform around the aperture because roll has very little effect on the focus of the image and oscillatory heave manifests as higher order terms in the phase solution which do not appear to significantly change the location of the minimum entropy point. A flowchart of the process is shown in Fig. 16, along with some examples in subsequent Fig. 17.

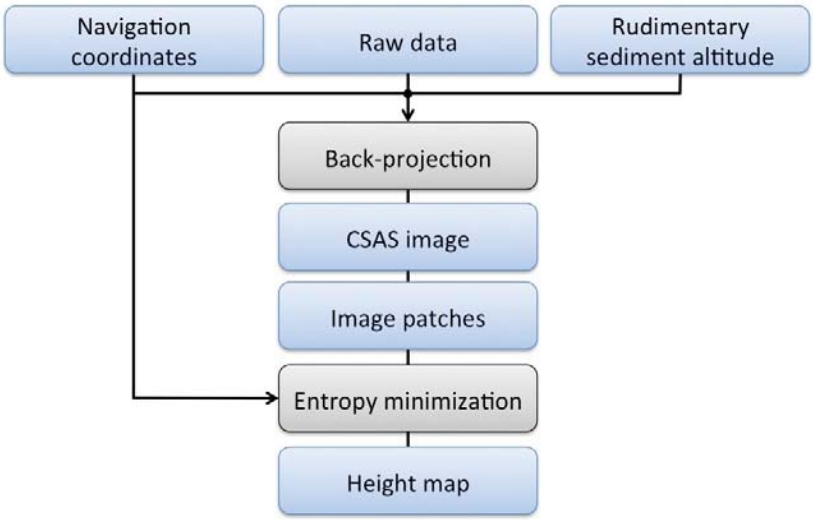

Figure 16. Flow chart of the entropic height map estimation process. Boxes in blue are data products, boxes in gray are processes.

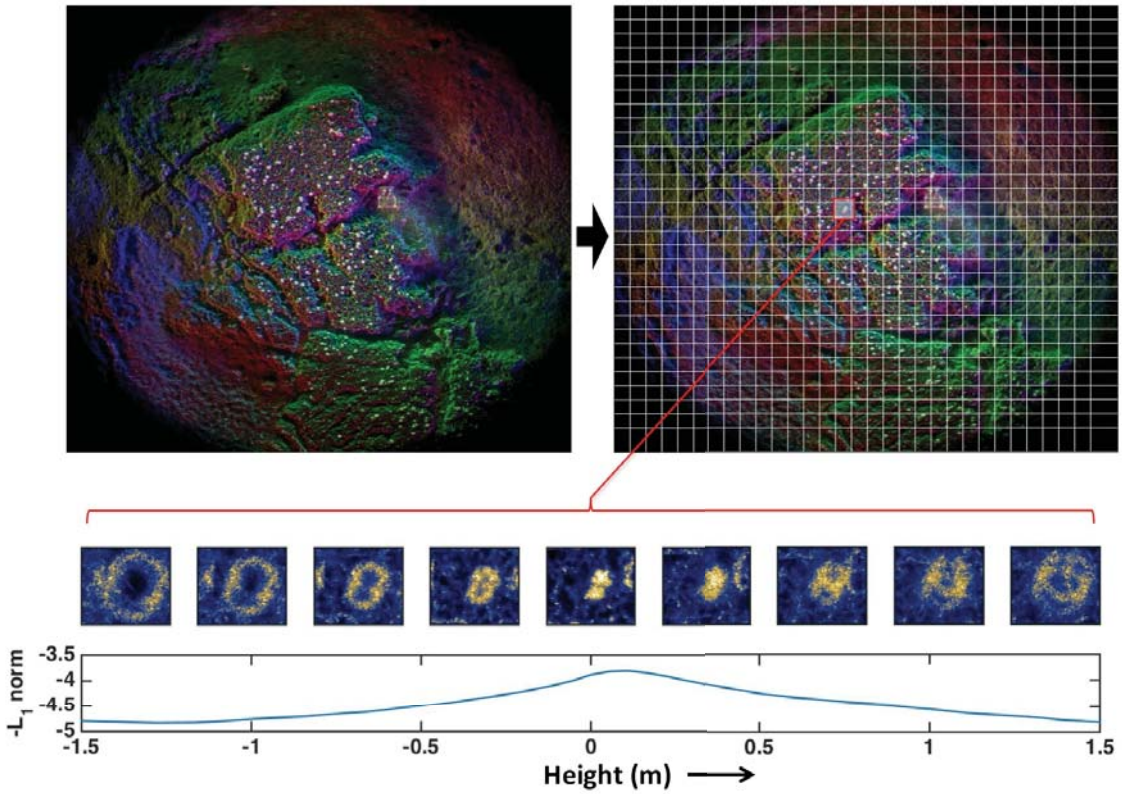

Figure 17. Illustration of the entropic height map estimation process. The image at top left is sub-divided into a series of image patches (shown at right). These patches are individually re-focused at different height planes, and the height-plane corresponding to the maximum image contrast is selected as the true height of the patch.

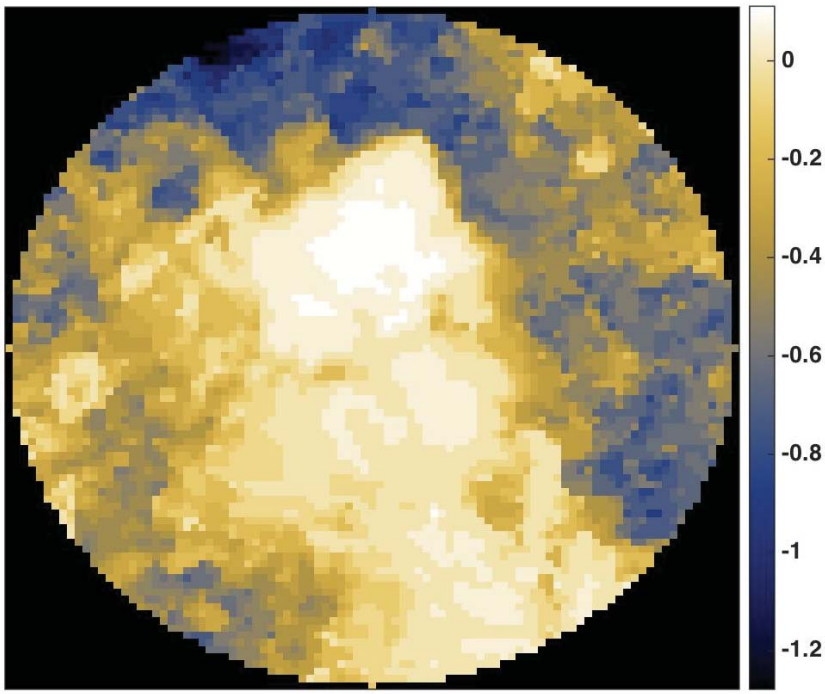

Figure 18. The entropic height map generated using the image in shown in Fig. 17 (note that the resolution cells are half the size of the cells shown in Fig.17).

Following contrast maximization a height map has been generated in Cartesian coordinates (Fig. 18). This height-map has not been computed in a manner that is immediately useful for calibration because the interferometric estimates are in a sensor-centric format more similar to polar coordinates, as illustrated in the Fig. 19:

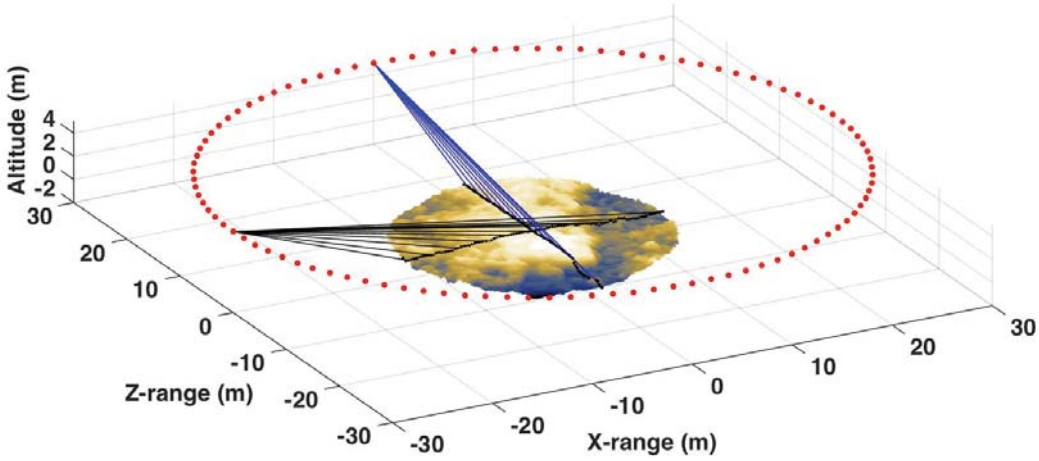

Figure 19. Illustration of the geometry of the interferometric data product. The interferometric readings from the sonar give bathymetric estimations for a line or beam extending from the coordinate of the aperture extending normal to the sonar (i.e., intersecting with the origin).

This sensor-centric format also incorporates the effect of a beamwidth, which will be wide or narrow depending on the number of elements beamformed prior to interferometry. The entropic bathymetry estimate is converted to the sensor-centric format by interpolating the bathymetry to a polar coordinate system centered on the individual interferometric sensor locations. A weighting function based on the sensor azimuthal beam-pattern is applied to the bathymetry estimates, which are then averaged in the angular dimension. The final result is very similar to a radon-transformation of the bathymetric height map in Cartesian coordinates. A comparison between the interferometry height estimation (bottom) versus the converted entropy solutions (top) is shown in Fig. 20.

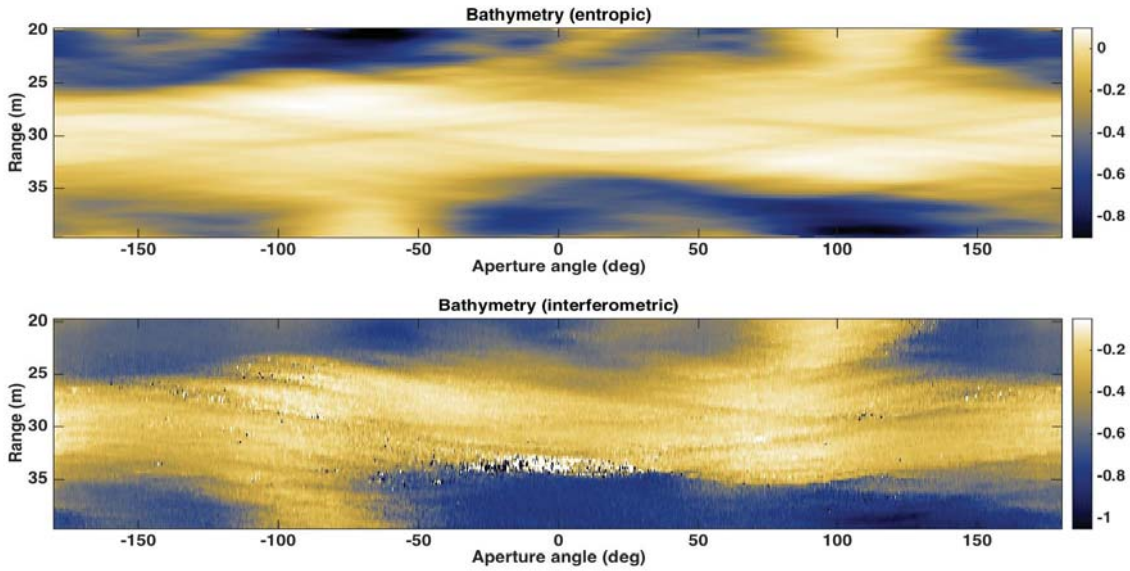

Figure 20. The bathymetry measured by the interferometric system (bottom) and the entropic height-map (top) converted to the sensor-centered format of the interferometric system.

Note that even though the current implementation is rather rudimentary (array yaw, and scatterer amplitude are not accounted for during the conversion process), qualitatively the comparison between height-map estimation methods shown in Fig. 19 is good. To generate a roll and heave calibration the difference between these scans is computed and the results are shown in Fig. 21:

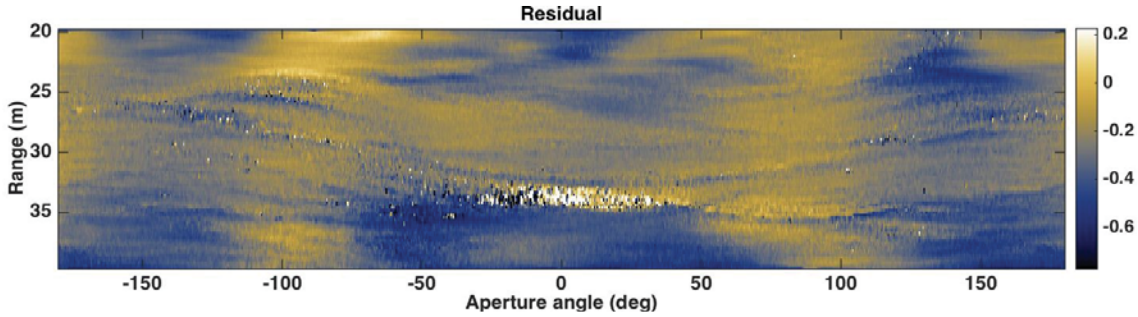

Figure 21. This figure shows the difference between the interferometry height estimate and the entropic height estimate. Trends in the range direction are a result of roll and heave errors. Sound-velocity profile could potentially also introduce errors but these are not currently considered.

To make a height and roll calibration the difference is represented as the weighted sum of bases functions representing the individual error functions associated with heave and roll: roll error manifests as a linear slope plus an offset, whereas heave error manifests simply as an offset. Both functions are modulated by the bathymetric height value itself. Example bases calculated via finite-difference for a height difference of ~0.1 meters and an angular difference of -0.01 radians are shown in Fig. 22.

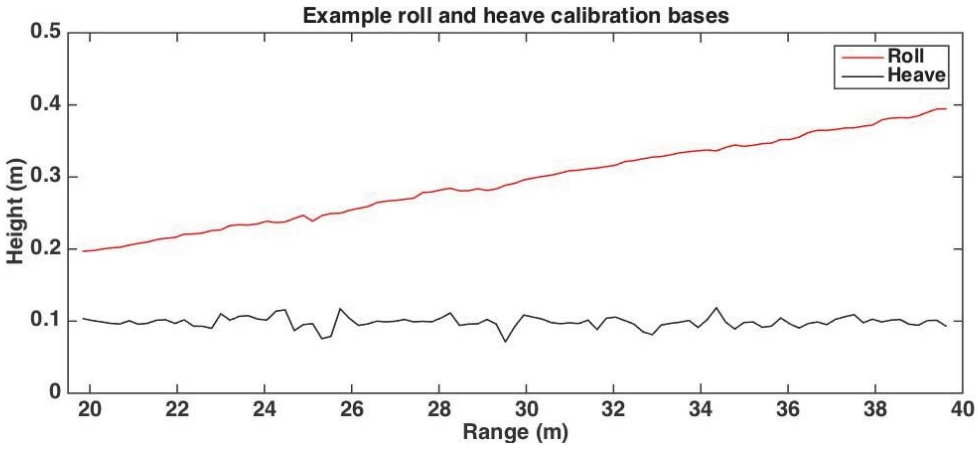

Figure 22. Interferometric roll (red) and heave (black) error bases computed via finite difference at a particular aperture location (θ ~= 100°). These bases are computed for all θ and used to fit the residual difference data shown in Fig. 20.

The inversion is regularized to penalize roughness (rapid changes) in heave error due to system inertia and the high confidence of the micronavigation results. The solution values for the roll and heave inversion are shown in Fig. 23:

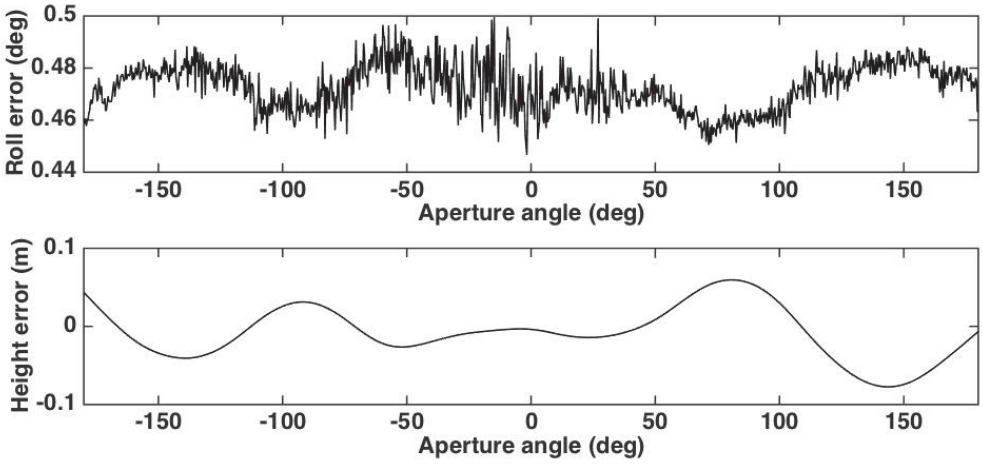

Figure 23. The residual roll error (top) and height error (bottom) shown in degrees and meters. Note the large roll offset of about half a degree.

The final residual is shown in Fig. 24, using the same colorscale in Fig. 21:

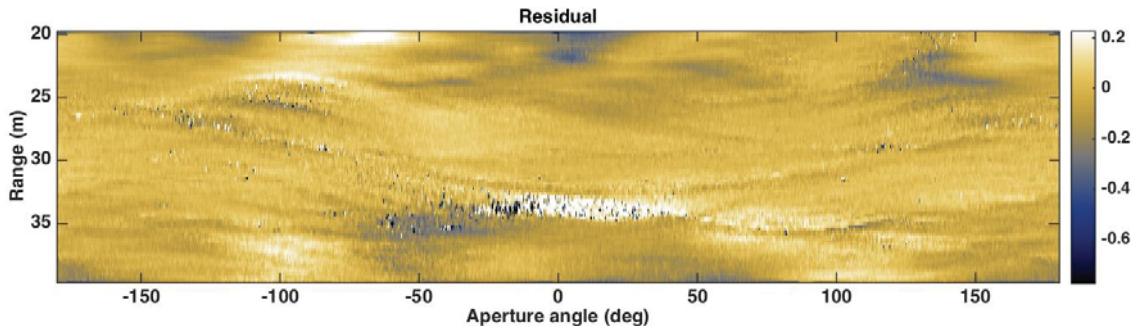

Figure 24. The final residual between the interferometric and entropic bathymetry estimates.

The question arises as to why height error with an RMS value of 0.03 meters can still be present after multilateration. The radial and height error basis functions in multilateration are only strongly linearly independent when the focusing patches cover a large range of grazing angles. In the present case the range of grazing angles is fairly limited and as a result, it is possible during autofocusing to trade a small amount of heave for sway and vice versa, without having a large affect on the focus of the patches, which may be happening here. This calibration process helps disambiguate these navigation error terms.

Verification of the solution can be found by taking advantage of the fact that in a circular aperture scenario a symmetry exists that causes the bathymetry estimate for each aperture location have an approximate mirror image on the opposing side of the aperture as depicted in Fig. 25:

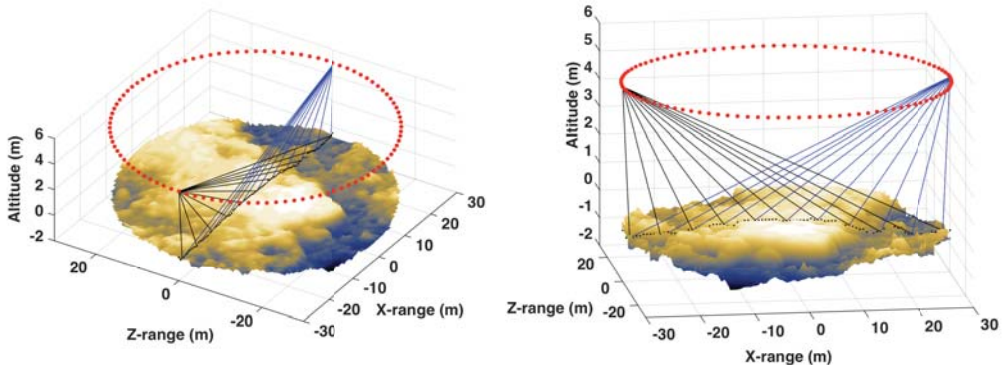

Fig. 25 Illustration of the symmetry of circular bathymetry estimates separated by 180 in a circular aperture.

It is possible to estimate the quality of the height values by calculating the average height error between the interferometric estimates and their opposing mirror images. These values are plotted in Fig. 26.

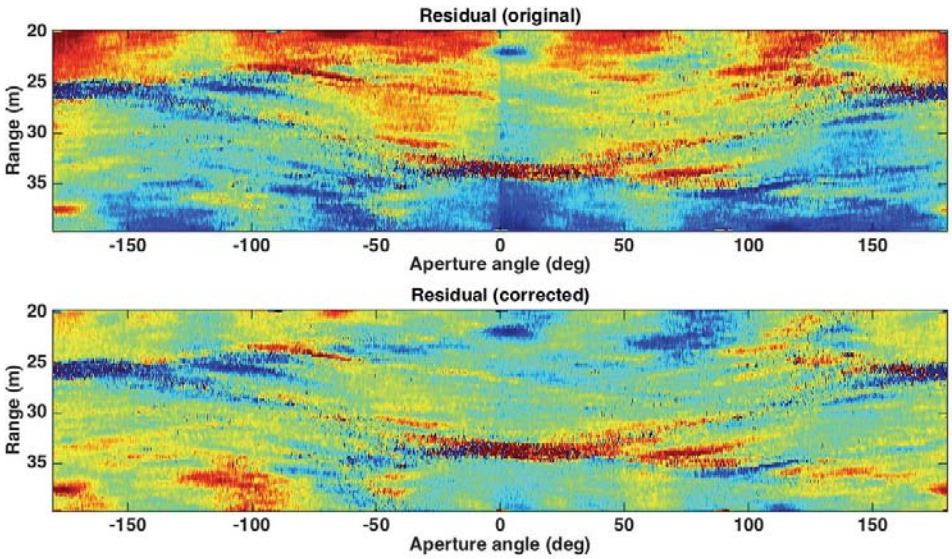

Figure 26. Circular symmetry errors for the interferometric bathymetry estimates before (top) and after (bottom) calibration via comparison with the entropic estimates. This comparison is make by taking a bathymetry estimate and subtracting itself from a version that has been flipped around the range point corresponding to the origin of the circle and shifted by 180 degrees.

The root-median-square of the original residual is 9.1 centimeters, versus 5.0 centimeters for the corrected version, an improvement by nearly a factor of two, with most of the improvement probably coming from the roll offset term.

Given the insensitivity of the entropy-based bathymetry estimate to various errors, one may reasonably ask why the entropy based bathymetry estimate is not used for the subsequent multipass alignment operation for which bathymetry is necessary. The answer is that the entropy based height estimate can only be computed for a relatively narrow span of ranges. The isolation of vertical and horizontal displacements is a necessity in the multipass alignment process, but high accuracy requires that a large span of grazing angles, and thus ranges be used. It is difficult to generate an entropy based height-map for a large enough area to accomplish this, because outside of a vicinity near the center of the circular aperture, the total contributions from the non-linear path decrease, causing the focus to be less sensitive to changes in altitude. Furthermore, interferometry is much faster to compute, because it requires only a set of correlations and phase differences. In contrast, the entropic height map requires that a high-accuracy beamforming operation be applied to circular SAS data and followed with a very large number of two-dimensional Fast Fourier Transforms applied patchwise. As a result, this calibration is only performed for the reference scan in the multipass set.

Lastly, despite the inclusion of this calibration process the residual error in the height map (RMS ~5 centimeters for the corrected version) will still cause observable biasing in the final three-dimensional image. As a result, a three-dimensional autofocusing algorithm was developed, which will be discussed in the section on coherent multipass dataprocessing.

SOFTWARE IMPLEMENTATION

The current version of the coregistration software is written in Matlab® and still in experimental format (i.e. some basic Matlab scripting knowledge is required to run the software), however for basic operation it keeps the human out of the loop except for the specification of various directories and files to load. The programming flow, from a scripting standpoint, is illustrated by the flow-chart in Fig. 27:

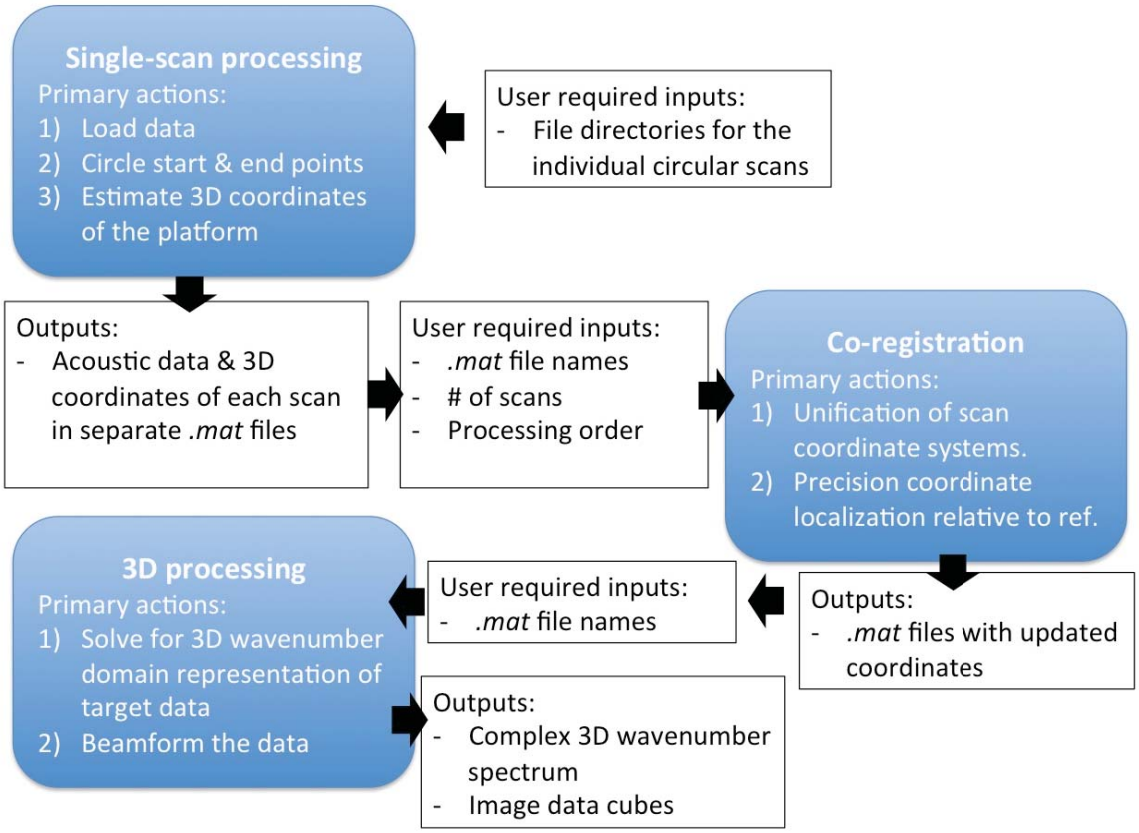

Figure 27. Processing flow for multipass data showing the three main stages (single scan processing, co-registration and 3D processing), the primary actions completed by the program and the required inputs and outputs.

The goal of keeping the human out of the loop is to test the robustness of the algorithm, i.e. if the program can coherently process the data with no user interaction in a broad variety of scenarios then it is robust.

In FY16 the major software emphases will be to 1) stress the algorithm in more difficult environments, which may include lower contrast sediments, higher oscillatory currents, shallower water with more multipath, etc., 2) Develop algorithms for generating training set data from the collected 3D wavenumber spectra and do target recognition tests, and 3) extend the current coherent multipass processing approach to allow collection over a broader range of vertical grazing angles than at present.

COHERENT MULTIPASS DATA PROCESSING

Following coregistration, the data are coherently combined via beamforming. The sampling is typically irregular in the multipass dimension (see e.g. Fig. 1), and in some circumstances undersampled, depending on the band of the sonar and the size of the target. The tomographic sampling requirements for a target in terms of the the angular spacing between samples Θ, can be expressed as a function of the diameter of the target scatterer distribution *D* and the wavelength of the acoustic frequency λ [2, 16]:

$$\Delta\Theta < \frac{\lambda}{2D}. \tag{32}$$

In the utilized scan patterns the average ΔΘ, (change in target grazing angle between scans) is ~0.56° for the vertical scan pattern and ~0.36° for the radial scan pattern. For a broadband sonar system with a maximum frequency of 30 kHz, (useful for structural acoustics analysis), eq. (32) indicates that objects with vertical scatterer distributions less than ~2.6 m and ~4.1 meters respectively will be well sampled.

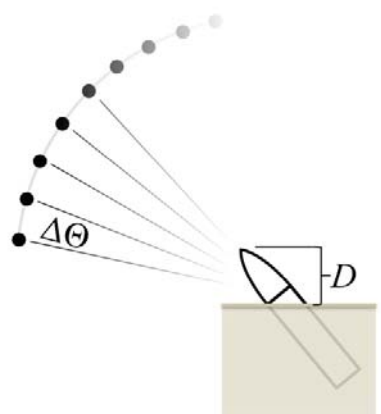

Figure 28. Illustration of the vertical target distribution value *D* (in this case the exposed portion of a UXO) and its relationship to the tomographic grazing angle sampling value ΔΘ. Note that if the sonar penetrates the sediment that *D* would be the entire height of the UXO, including the buried portion.

Most UXO, even at oblique angles such as illustrated in Fig. 28, will have scatterer distributions that are less than several meters in the vertical direction. For the experimental system making the measurements shown in this paper, all insonified targets are well sampled in the low frequency band. At the high band, the aperture was partially undersampled for some large targets, i.e. the criterion of eq. (32) was met for certain portions of the aperture, but not others. The beamforming method, which is described in full technical detail in Section IV of [2], is composed of the following 5 steps:

1) The data from each scan is interpolated to the ground-range
2) The data is sub-banded

3) Using either an inter-band or azimuthal (or both) block-sparse assumption, the vertical scattering profile is solved using a joint-sparse linear system solver (M-FOCUSS [17]).
4) The horizontal scattering profile is solved by applying projection slice beamforming to each plane of the vertical scattering profile
5) The complex 3D target scattering information is converted to either the wavenumber or image domain using a 3D FFT.

Fig. 29. graphically illustrates how the individual, vertically beamformed data slices are combined around the aperture and used to form either a 3D image or a 3D wavenumber spectrum.

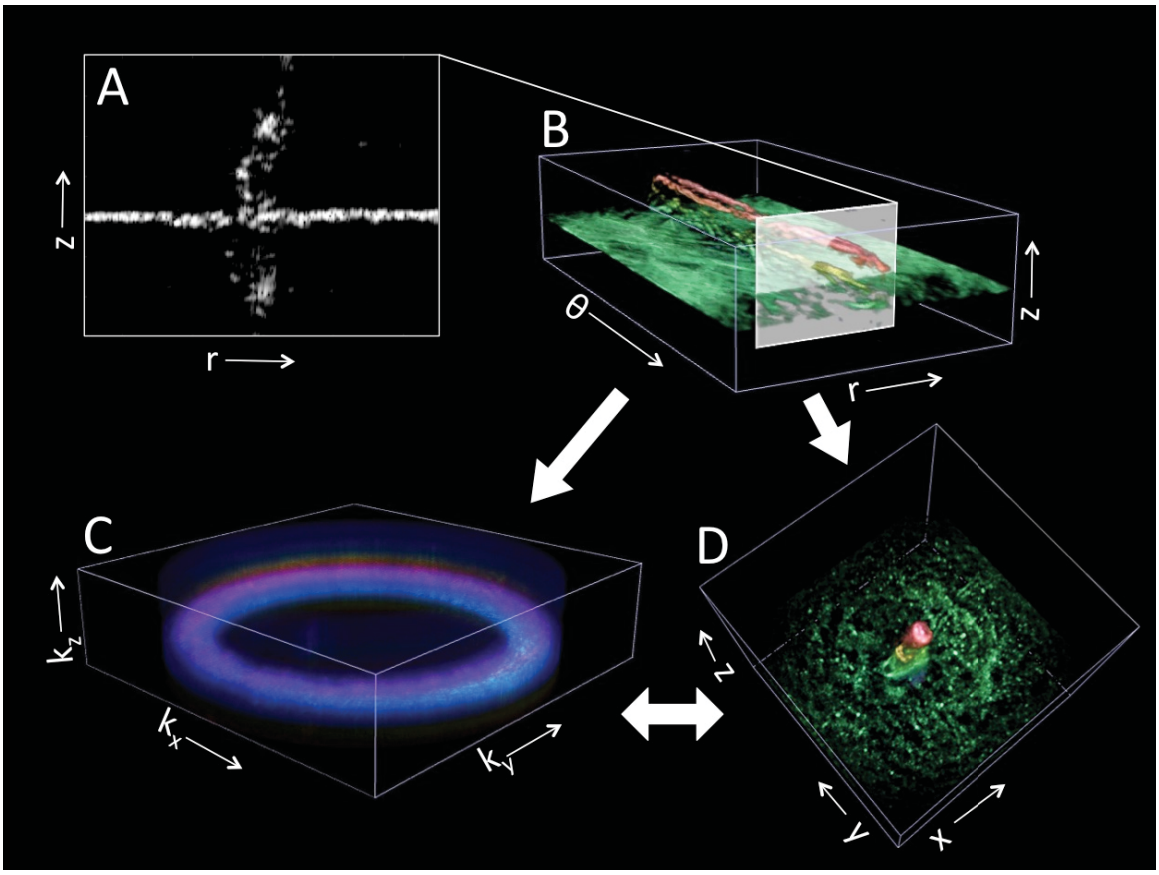

Figure 29. Illustration of the 3D beamforming process. Following projection of each scan to the ground-plane the data is beamformed in the vertical dimension (A). This is done for all points around the aperture (B). A far-field conversion is applied to each height plane which is then projection-slice beamformed in $K_{x,y}$ wavenumber space [18]. This can be converted to a 3D wavenumber spectrum in $K_{x,y,z}$ by computing a vertical Fourier transform or an image by taking an inverse two-dimensional Fourier transform in the horizontal dimensions. The image and wavenumber domain can be computed from each other via 3D Fourier transform.

When a complex image or wavenumber spectrum is generated, the complementary spatial or spectral domain representation can be created via a simple and efficient 3D Fast Fourier Transform (FFT). To make the image in Fig. 29 and the other images shown in [2], [8] and [19],

the spectrum is sub-divided into a series of sub-apertures and incoherently combined. This was found to reduce speckle and increase the interpretability of images. The tool used to visualize the images in Fig. 29 and related publications was VAA3D, a 3D visualization tool that is frequently used for medical purposes [20], [21].

3D AUTOFOCUS

The current implementation of the multipass coregistration algorithm estimates the location of all scans in a dataset relative to a reference dataset. Navigation errors in the reference dataset, particularly sonar altitude errors, result in artifacts in the wavenumber spectrum and vertical smearing in the image. To reduce these errors a vertical map-drift algorithm was developed. It functions in a manner very similar to the cumulative-sum algorithm described in [7], but instead of tracking shifts in the horizontal plane it tracks altitude drift in slices of the vertically beamformed data. A flow-chart of the vertical map-drift algorithm is shown in Fig. 30, followed by an algorithm description.

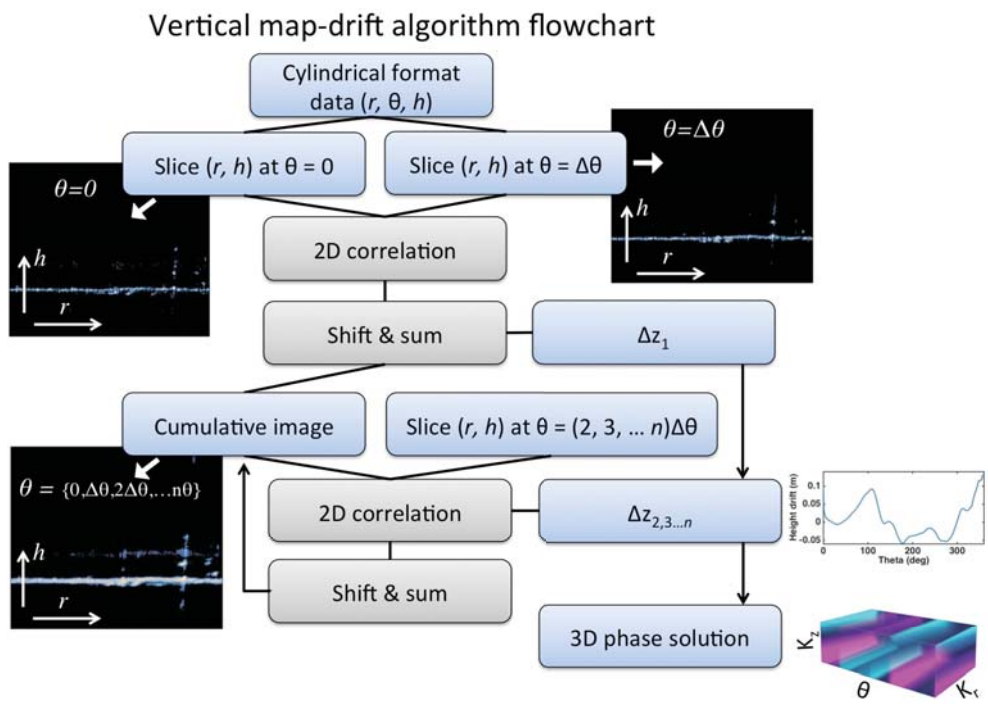

Figure 30. Outline of the vertical map-drift algorithm.

The algorithm operates as follows: after beamforming in the vertical dimension the slice at the first aperture point ($\theta = 0$) is two-dimensionally cross-correlated with the slice at the adjacent location $\theta = \Delta\theta$. (Note – shifts in only one dimension are expected, but two-dimensional correlation is used because it results in a correlation measurement with a high signal-to-noise ratio). The relative vertical shift of the image ΔZ_1 is refined to sub-pixel precision using parabolic interpolation as demonstrated in [22]. Linear interpolation is used to align the image at $\theta = \Delta\theta$ with the image at $\theta = 0$, and the images are summed to form a cumulative image. This cumulative image is then correlated with the next adjacent aperture, at $\theta = 2\Delta\theta$. The vertical shift ΔZ_2 is computed, the aperture at $\theta = 2\Delta\theta$ is aligned with the cumulative image and summed with

it. This process of correlating with the next adjacent aperture, shifting and summing is progressively applied through the whole aperture[1], resulting in a vector of shift measurements, $\Delta Z_{1,2\ldots N}$.

When the vertical shifts are known, the complex vertically beamformed data can be shifted in the height dimension to correct for the drifts, however this induces a radial error term because the slant range to the center of the image has been effectively changed. To prevent this error from occurring an additional range shift is applied that preserves the original slant-range of the data in the slice. The two-dimensional phase correction that is applied at each aperture location $\theta_{1,2\ldots N}$ is:

$$\phi_n(K_z, K_r) = e^{-j(\Delta Z_n K_z + \Delta r_n K_r)} \tag{33}$$

$$\Delta r_n = \sqrt{R_n^2 - 2\Delta Z_n H_n - \Delta Z_n^2} - R_n \tag{34}$$

Where H_n and R_n are the altitude and radial distance of the sonar at θ_n, and K_Z and K_r are the height (Z) and radial (r) dimension wavenumbers. The correction is applied directly to the two-dimensional Fourier-transform of the data slice at θ_n:

$$\bar{S}_n(r, Z) = \mathcal{F}^{-(2)}\left\{\mathcal{F}^{(2)}\left\{\tilde{S}_n(r, Z)\right\}\phi_n(K_z, K_r)\right\}, \tag{35}$$

where $\mathcal{F}^{(2)}$ and $\mathcal{F}^{-(2)}$ are the forward and inverse 2D FFT operations, $\tilde{S}_n(r, Z)$ is the original (corrupted) raw data that has been beamformed in the vertical dimension, $\phi_n(K_z, K_r)$ is the complex phase correction shown in (33), and $\bar{S}_n(r, Z)$ is the corrected data. This process is graphically illustrated in Fig. 31:

[1] In practice the vertical scattering profile changes significantly as a function of aperture so only a limited history of aligned frames are preserved in the cumulative image as the algorithm progresses.

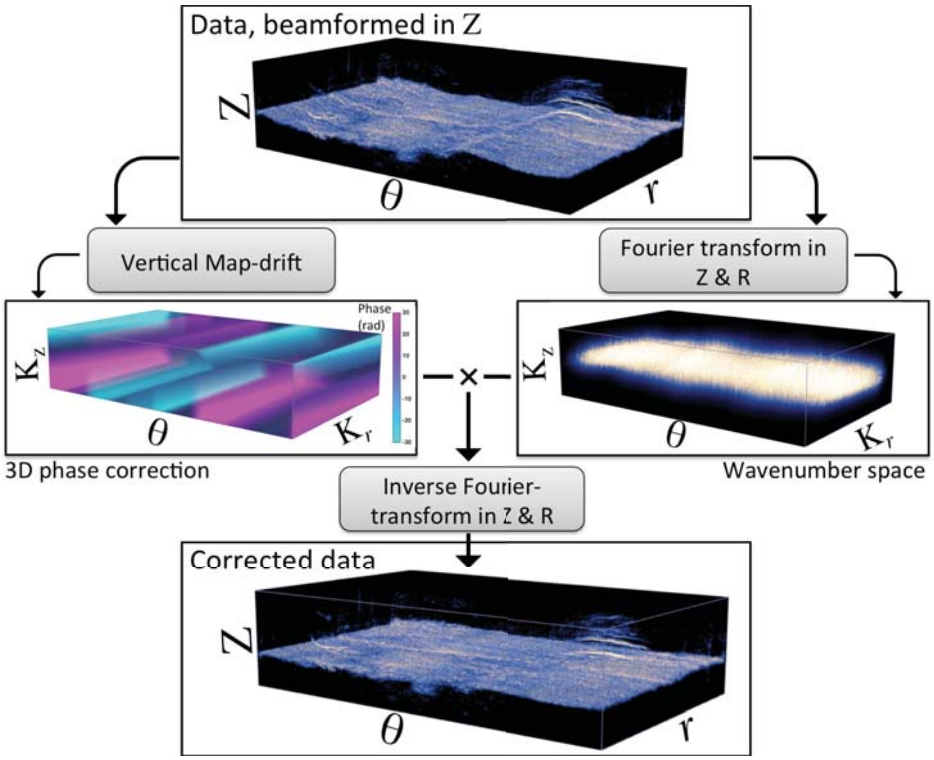

Figure 31. The application of the map-drift algorithm to the 3D data and the correction process. The raw, vertically beamformed data (top) is passed to the map-drift algorithm from which a phase-correction datacube is computed. The two-dimensional Fourier transform of the vertically beamformed data is computed in the *Z* and *r* dimensions and the phase correction is applied. The corrected dataset (bottom) is recovered following the inverse two-dimensional Fourier transformation.

The test data shown in Fig.'s 30 and 31 is of relatively flat sediment, so a helpful graphic illustrating the affect of the algorithm is to show the projection of the data onto the $r = 0$ plane. Following correction the sediment altitude appears nearly flat as a function of θ, as shown in Fig. 32.

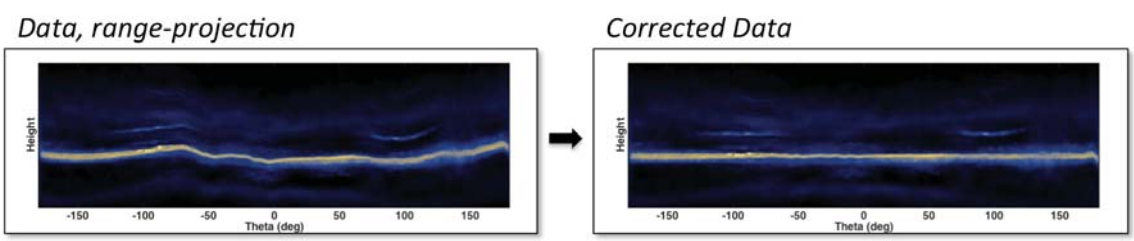

Figure 32. The vertically beamformed data, averaged in the range-dimension and visualized. The bright line corresponds to the sediment interface. In the uncorrected data, the sediment height changes with look angle, vs. in the corrected data in which it remains at a constant altitude.

The effect on the image is to enhance the vertical focus of the three-dimensionally beamformed data. By applying projection slice beamforming to the horizontal planes of vertically

beamformed data, the 3D image can be reconstructed. The following figure compares vertical slices through the image for the case in which the vertical map-drift algorithm was applied prior to beamforming vs. the case in which it was left uncorrected. Additionally, an alpha-rendered patch of the 3D image is shown to highlight the effects on 3D imagery.

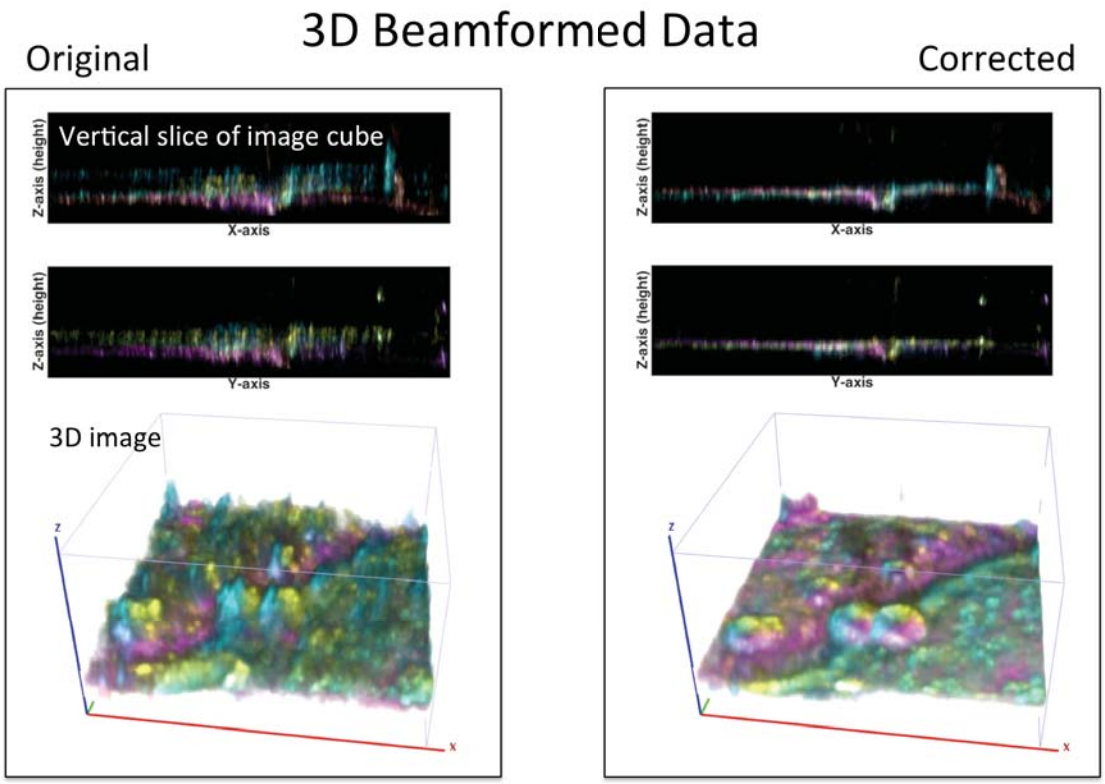

Figure 33. Slices through the 3D image data cube (top and middle) and a rendered 3D image (bottom) for the case in which no vertical map-drift was applied (left) versus the case in which it was applied (right). The images at right show superior focus in the vertical dimension. Note that back-scattering angle is mapped to color in the above examples.

As can be seen in Fig. 33, the corrected data results in much better focus in the vertical dimension.

This concludes the section on the coherent processing of the data to generate a coherent three-dimensional data-product. Related to the goals of this product, generating a well-focused complex three-dimensional image data product indicates that the three-dimensional wavenumber spectrum has low levels of phase error and can be used for training set generation, which will be the focus of the final year of the current research effort.

As a final note, the number of steps required to arrive at a useful data product seems fairly large, however in many cases reasonable data products can be generated without using any of the roll calibration / autofocusing operations or even exploiting interferometry. In fact, all of the example data products shown in [2] were done without explicitly using any interferometry in the signal processing chain at all (a flat bottom was assumed during navigation), and vertical map-drift

autofocusing was never applied. The primary advantage of the more complex approach is that the data product is better in a larger variety of environments.

RESULTS AND DISCUSSIONS

The results of the first set of multipass experiments, conducted in December 2014, are discussed in detail in Section V of [2]. These results, which will be summarized here, focused primarily on high-frequency image domain data products. Figure 31 shows a volumetric image of a howitzer, proud on a sandy sediment.

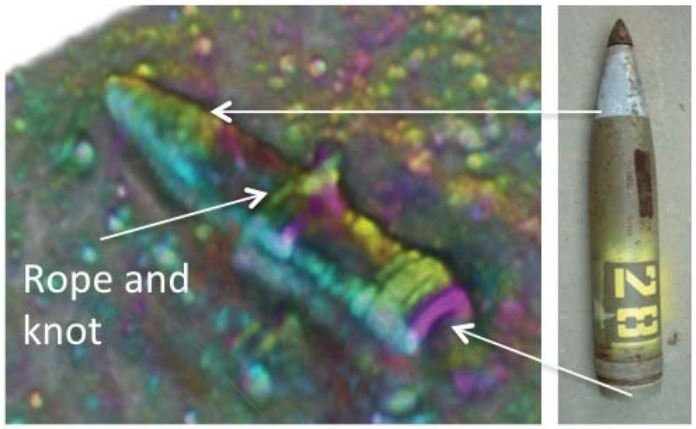

Figure 34. Photograph of a 155 mm Howitzer shell (right) and the 3D volumetric acoustic image (left), showing the material boundaries at the front of the shell, the components of the end-cap, and a nylon rope tied around the center for diver manipulation (not in photo).

Despite the center frequency being relatively high (low hundreds of kilohertz), the material boundaries at the front of the shell are visible. Other details, such as the rope tied around the shell to aid in diver manipulation, and the rings of the end-cap are also clearly visible. The same target was scanned using both the radial and vertical scan patterns. Table 2 shows a list of all the targets and the scan patterns that were completed for each target:

Target	Radial scans	Altitude scans
Proud Howitzer	9	9
Oblique Howitzer	9	9
Steel Barrel	6	0
2-1 cylinder	8	0

Table 2. A list of the scanned targets and the number of scans completed for the radial and altitude types. The AUV malfunctioned after 6 scans around the steel barrel, and no altitude scans exist for either the steel barrel or the proud, solid 2-1 aluminum cylinder.

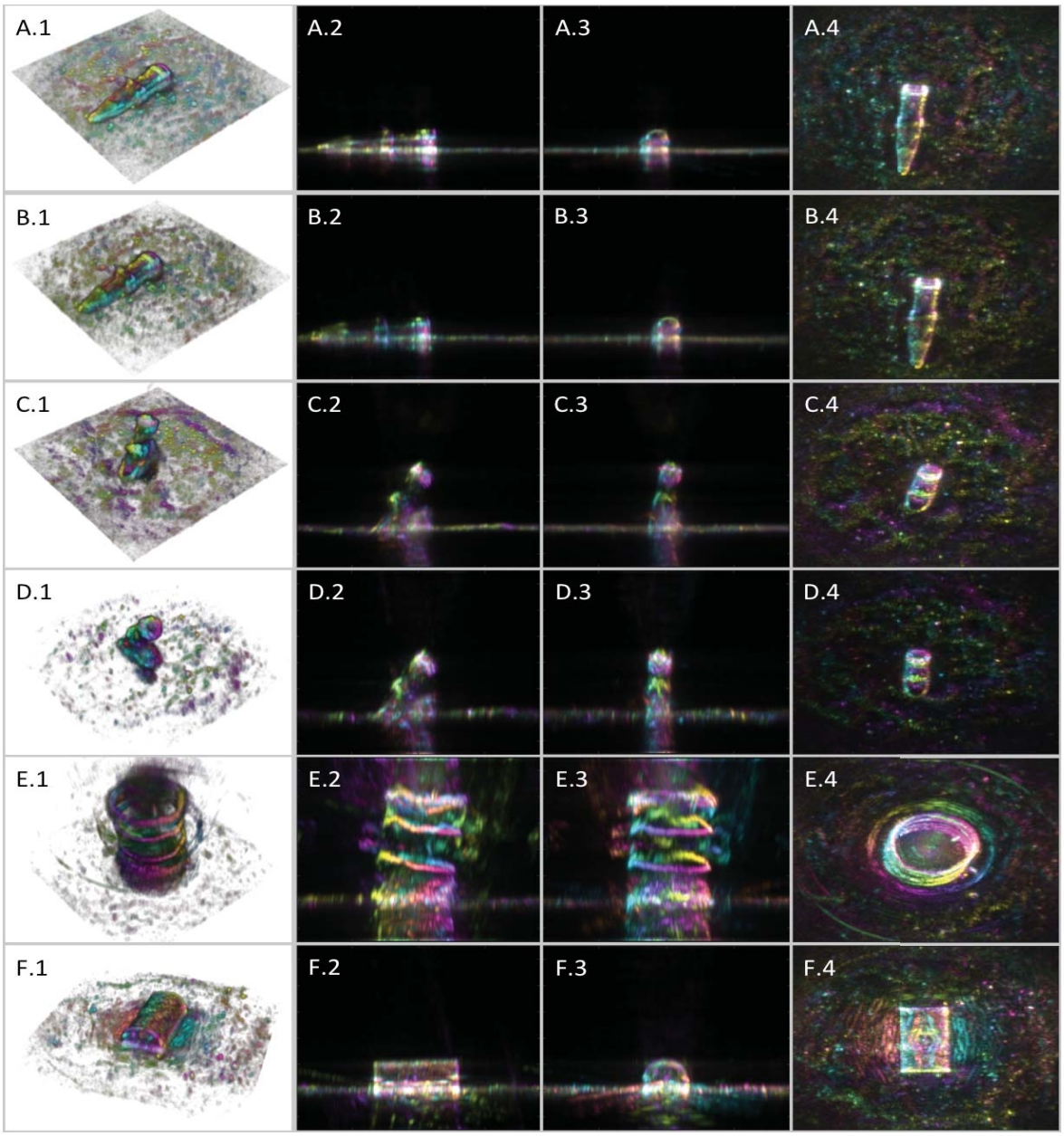

Figure 35. Rendered images and projections of the volumetric data corresponding to the scans described in Table 1. Column 1) shows the linear scale three-quarter view volumetric images rendered using alpha blending, column 2) shows projections of the volumetric images onto the *XZ* plane, column 3) shows projections onto the *YZ* plane, and column 4) shows projections onto the *XY* plane. From top to bottom, the rows show: a) proud howitzer, altitude scan, b) proud howitzer, radial scan, c) oblique howitzer, altitude scan, d) oblique howitzer, radial scan, e) proud vertical steel barrel, radial scan, and f) proud 2-1 solid aluminum cylinder, radial scan.

Figure 35 is a visualization of each of these targets for the different scan configurations. Note that the barrel still images extremely well despite the fact that only two-thirds of the scans around the target were successfully completed. Furthermore, it was confirmed that for small

image patches the two scanning approaches (vertical and radial) give almost identical results (e.g. compare row A with row B, and row C with row D). The target orientation relative to the sediment (e.g. proud, partially buried, oblique, etc.) can be precisely determined from the 3D images in Fig. 36, indicating that the high-frequency 3D image data-products can be used as ground-truth position data for low-frequency model - vs. - data comparisons, which could be useful for evaluating target simulation methods.

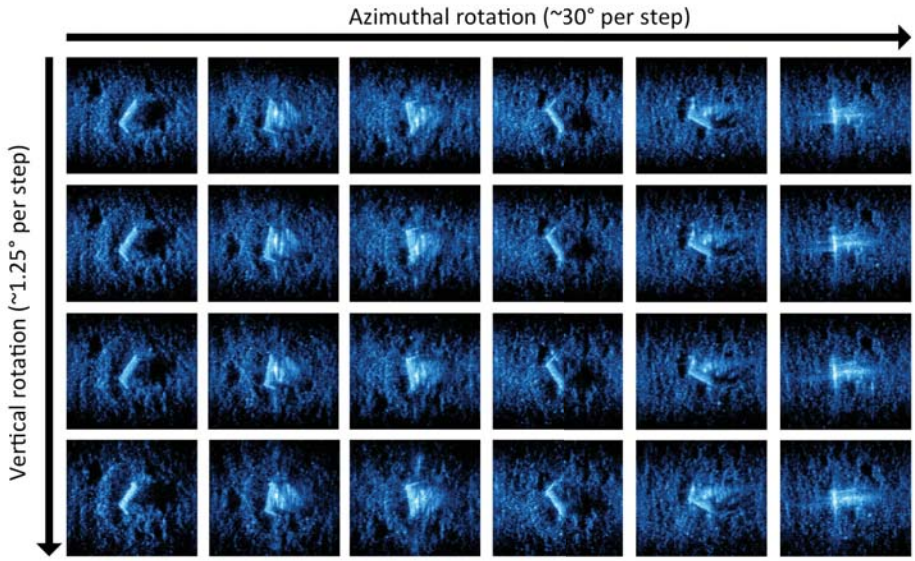

Figure 36. Illustration of high-frequency image snippets produced using the multipass 2-1 aluminum cylinder data. The variables are azimuthal and vertical rotation. The figure is for illustrative purposes, an actual training set would vary more finely over angle, and over a larger span vertically, as well as introduce other variables such as noise and various types of realistic phase error.

Figure 36 demonstrates the generation of a basic aspect vs. grazing angle training set from the 2-1 cylinder data. In the figure, the target orientation is changed to span both of these variables over ~140 degrees in horizontal rotation and ~6 degrees in vertical orientation. The span of angles in the vertical dimension is short, limiting the observable change of behavior in that dimension, however FY16 experiments have been designed to extend the sample range in this dimension.

The results in Fig. 35 and 36 made no use of the roll calibration and autofocus calibrations, and made only basic assumptions about the sediment (i.e. that height did not vary with range: effectively a flat sediment assumption). High quality results could still be produced because the sediment was flat in the scanned region. In the second dataset, collected in June of 2015, the sediment was rocky, and the bathymetric variation was much higher. In response to these changes, the roll-calibration and autofocusing techniques described in previous sections were developed and bathymetry priors were estimated via interferometry and plugged into the co-registration equations. Furthermore, additional emphasis was placed on low-frequency data processing. Figure 37 shows an example 3D image and 3D wavenumber spectrum for a scene

containing a large coral outcropping (marked by red arrow) and a howitzer with an end-cap (marked by white arrow).

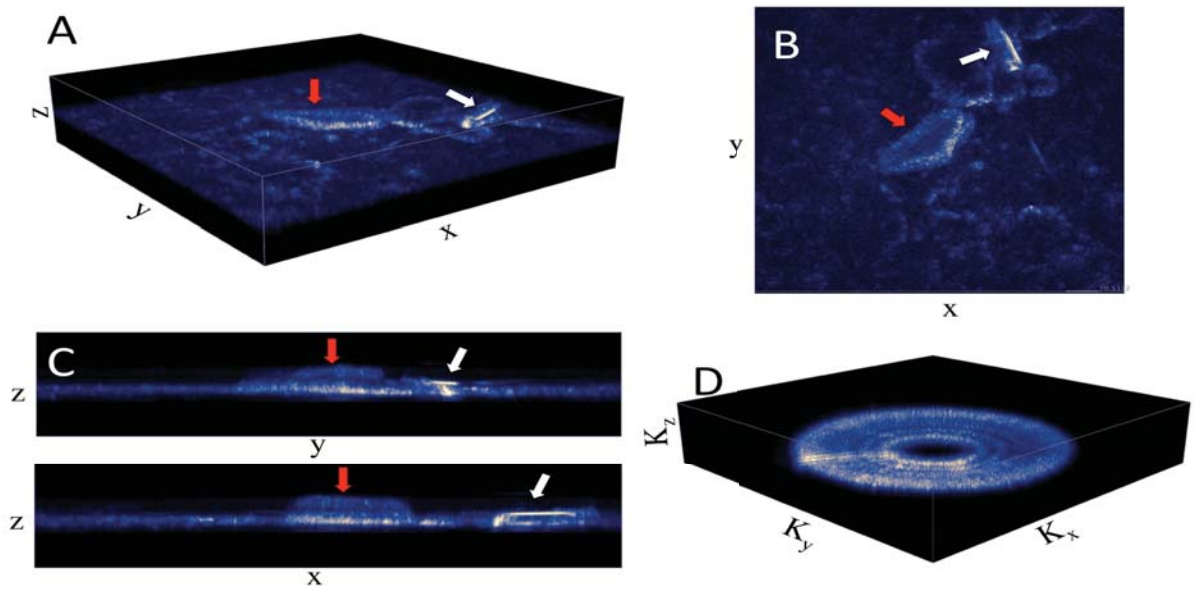

Figure 37. The coherently processed low-requency 3D dataproduct from a multipass set, in this case containing a coral outcropping (red arrow) and a proud howitzer shell (white arrow). Image (A) shows the 3D image from a three-quarter view perspective, while (B) and (C) project the image onto the [X, Y], [Y, Z] and [X, Z] planes. Image (D) is a three-quarter view of the three-dimensional wavenumber spectrum of the image.

The 3D volumetric images in Fig. 36 are simply the magnitudes of the coherent data-products, and the incoherent sub-aperture averaging process and aspect-to-color maping applied in Fig. 32 is not being applied here. In comparison to the high-frequency data-product for the same scene, the low-frequency image has relatively low vertical resolution, as can be seen by comparison with the high frequency version shown in Fig. 38.

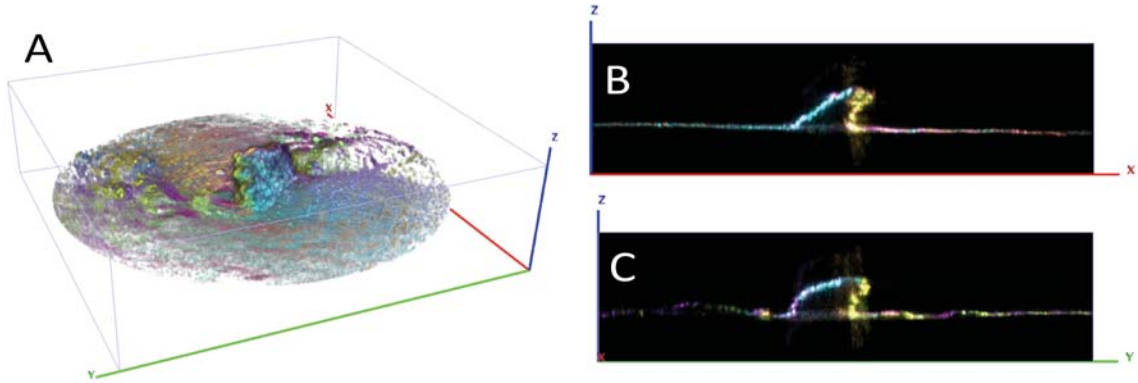

Figure 38. A high frequency three-quarter view (A) rendering of the rock and howitzer image shown in Fig. 37, along with two slices (B and C) through the rock. Note that overhangs are well imaged using the 3D tomography approach.

Figure 39 shows zoomed views of the low-frequency image of the target, captured from the 3D dataset shown in Fig. 37.

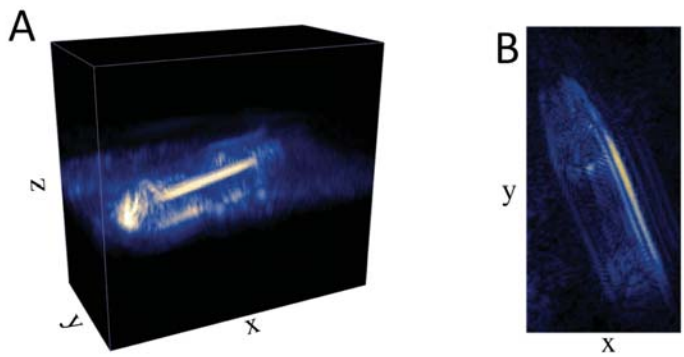

Figure 39. 3D snippet of the howitzer scene, showing just the howitzer. Image (A) is a three-quarter view, and image (B) is a horizontal planar slice through the image, showing the tip, the sides, the endcap, and material boundaries.

If the three-dimensional wavenumber spectrum is computed from the 3D snippet containing just the howitzer, the wavenumber spectrum of the target becomes much more visible, which is shown in Fig. 40.

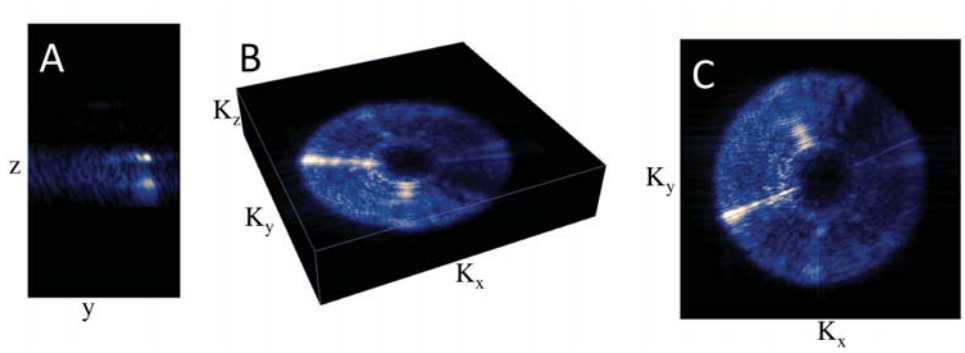

Figure 40. (A) a vertical slice through the image snippet showing a glint and its sub-sediment reflection, and (B and C) the three-dimensional wavenumber spectrum for the 3D snippet.

In Fig. 40 a vertical slice through the specular edge-glint is shown to highlight its relation to a wavenumber domain phenomenon. The specular glint in Fig. 40(A) (the bright, well-focused glint) is accompanied by a reflection below the sediment. This phenomenon is well known in other literature (see e.g. [23] and [24]). In the wavenumber spectrum, the presence of the glint causes an interference fringe that manifests as a series of evenly spaced nulls in the vertical direction for the narrow glint feature, that are visible in Fig. 40(B). These nulls are a three-dimensional visualization of the sweeping null phenomenon described in [25], and this is probably the first experiment to visually tie these concepts together (i.e. explain the sweeping null phenomenon in [25] in terms of a vertical interference pattern that manifests in the 3D wavenumber domain that is caused by multipath inteferences).

Many other targets were scanned in the second data set, and the following example high-frequency images are a subset of the data products. Figure 41 shows a lobster-trap. From the various renderings of the lobster trap the external features (curved top, bottom, wooden slats comprising the top etc.) are visible, as well as the internal features such as the ring-inlets for the lobsters as well as a the netting stretched between the rings and the sides and a post to which the netting is connected in the interior. The sediment is also visible beneath the target.

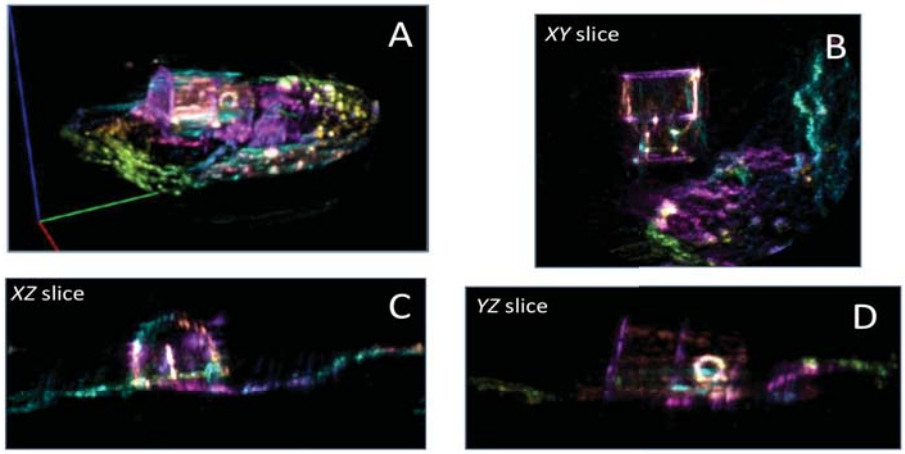

Figure 41. 3D multipass image of a lobster trap. Image (A) is a three-quarter view of the target, and (B), (C), and (D) are slices that show significant external and internal features of the target.

Figure 42 shows the 3D image for a plastic barrel. The bottom 8 inches of the barrel were filled with concrete. Additionally, a track-and-field shotput was suspended in the center about 14 inches below the top of the barrel. Scattering features from both the concrete (red arrows) and the sphere (white arrow) are visible in the three-dimensional reconstruction.

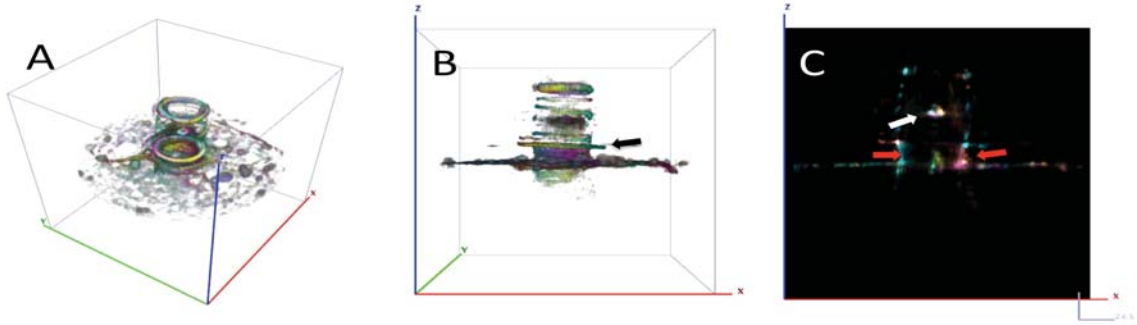

Figure 42. 3D multipass image of a plastic barrel. Image (A) is the three-quarter view of the target. Image (B) shows a side-view, emphasizing a corner scattering mechanism with the black arrow. Figure C is a cutaway of the target, where the red arrows show the enhanced scattering from the portion of the barrel filled with concrete and the white arrow points to the suspended sphere.

Note that the concrete causes an enhanced scattering from the side of the barrel (red arrows) but that the top of the concrete does not appear in the image, due to the sound completely reflecting off of the top. One of the brightest features of the target, however, is the corner scattering mechanism formed by internal reflections off the back side of the barrel and the concrete interface. This corner scatterer has an extremely bright focusing point at the top of the concrete interface and extends temporally beyond the back wall of the target. This feature is marked in Fig. 42(B) with a black arrow.

Figure 43 shows a tire from different perspectives. The rim of the tire was removed, so there was no bright, high impedance reflection. Furthermore, there was very little rough surface scattering from the tire, and most of the signature from the target was dominated by corner scattering.

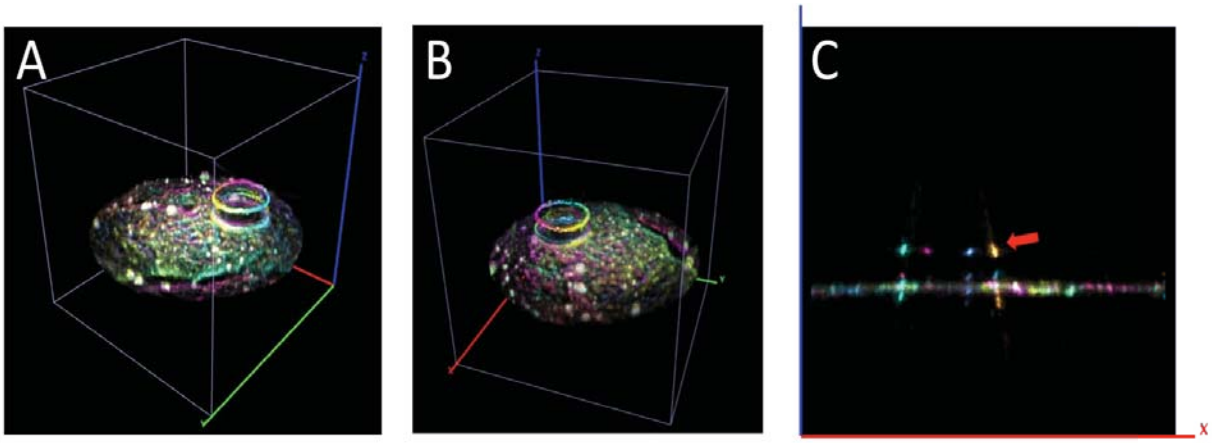

Figure 43. 3D multipass image of a car tire with no rim. Images (A) and (B) show two different views of the target, and image (C) shows a cutaway. From Fig. (C) it is clear that corner scattering dominates the backscattered response.

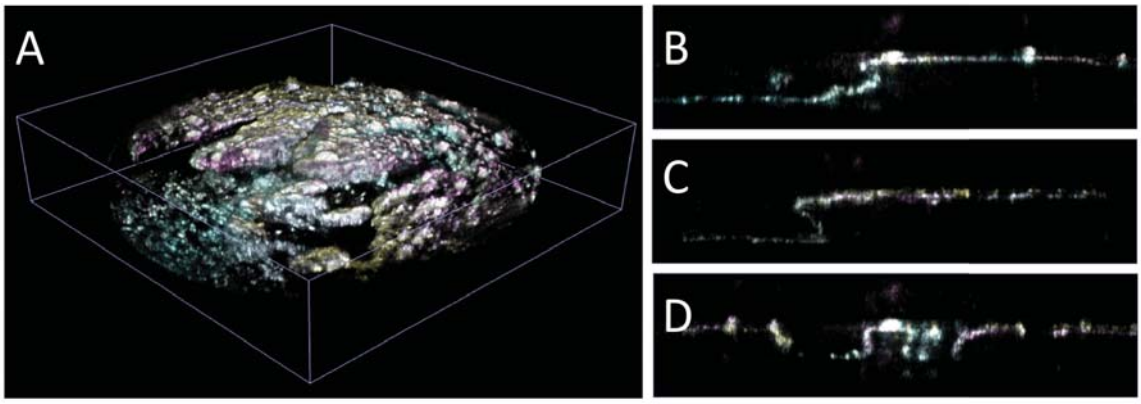

Figure 44. 3D multipass image of rock and coral sediment. Figure (A) shows the region from a three-quarter view perspective, and (B) – (D) are slices of the image.

The images shown in Fig. 44 have no deployed target in the scene allowing a rock and coral formations to be viewed and illustrate advantages and drawbacks of 3D multipass imaging. Due to the low grazing angles used during the scan (~11°) it is possible to image underneath

overhangs, as is visible in Fig. 44(B) and (C). On the downside the low grazing angles may prevent insonification of occluded regions at the base of trenches, a problem visible in Fig. 44(D), in which the bases of the trenches are occluded and don't beamform.

Additional scans exist that have not yet been processed, but a common flaw to all the datasets captured thus far is the limited span of grazing angles. The scan patterns used in the FY15 datasets only cover about 5 degrees total of grazing angle, which limits the volume of information captured in the 3D wavenumber domain. In FY16 test plans are in place to scan targets over a broader range of grazing angles (~15 degrees) which should make the low-frequency data products more useful, especially for training set generation and comparison with finite-element models.

CONCLUSIONS TO DATE

Training set generation for UXO classifiers is a primary goal of this project, and what will be facilitated by the previously described 3D data processing techniques. To understand why training set generation is important it is helpful to have some context for SONAR based UXO classification. The field of machine learning has been undergoing a revolution in the past decade, and computers are getting extremely good at tasks similar to UXO classification, such as such as facial recognition [26] and even general image recognition [27]. It is reasonable to ask why computers have gotten so good at image recognition, while a robust sonar-based solution to the UXO classification problem still remains elusive, though it may seem intuitively to be simpler.

In recognition tasks, two primary ingredients are required for successful classification: *training data* that spans the degrees of freedom of the signals, and robust yet descriptive and discriminatory *features* that can be computed from the signals. Features are a key concept: a feature is a numeric description of some property of a sensed signal. Ideally a feature will have some value if the signal originates from a UXO, and a different value if the signal originates from a non-UXO, however the complexity and degrees of freedom of realistic sonar signals mean that a simple binary relationship between class and feature values almost never exists. Example features may be the mean, variance or skewness of a signal, or may simply be the amplitude of a pixel or pixels in an image snippet. Alternatively, features may be the length of a shadow extracted from an image, the width of a broad-band spectral feature of a target, or some measure of the target symmetry.

Critical to SONAR based UXO recognition, the value of most features will be coupled either weakly or strongly to such parameters as angular orientation, burial depth, sediment type, etc. and may also be affected by errors in coherent signal processing. To accommodate the complexity of sonar signals and the degrees of freedom of a signal originating from clutter or a UXO, a large number of features may be required. This invokes the concept of the "curse of dimensionality": as the number of features increases, the amount of data required to determine statistically significant relationships between features increases exponentially. This is a major hindrance to classification: to classify UXO data are needed showing target signatures of UXO at different angles, different altitudes, different burial depths, in different environments, and with different levels of "corruption" (noise, phase error, biofouling, etc.). Without this information it may be difficult to even know which features are useful and discriminatory.

To address this lack of data, much research has been directed towards numerically modeling the response of targets. Furthermore various experimental efforts, such as PondEx10 [28], GulfEx12, TrEx13 [29], and BayEx14 have been funded to get real data for targets in different environments. These efforts are complementary, because the experimental work can be used to both validate the numerical efforts as well as understand what the practical effects the environment may have on the physical scattering mechanisms associated with targets. Given the degrees of freedom for UXO signals however, it is impossible for the current set of experimental or numerically generated datasets to provide robust classification in all environments.

The goal of this project is to provide a technique to help fill a portion of this data gap: to provide a means by which environmentally relevant training sets can be rapidly acquired. Previously, a number of variables were listed that affect UXO signals: sensor aspect angle, sensor grazing angle, sensor beamwidth and bandwidth, target obliqueness and burial depth, sediment type, ambient noise, multipath noise, coherent processing error, etc. These variables can be divided into three catagories: sensor variables (aspect angle, grazing angle, sensor beamwidth), noise variables (ambient and multipath noise, coherent processing error), and target variables (obliqueness, burial depth, sediment type). Of these categories, both the sensor and noise variables can be *rapidly* simulated given an in-situ measurement of the three-dimensional scattering response of a target. An example of this rapid simulation was shown in Fig. 36 for a limited set of aspect and grazing angles.

The work in FY15, summarized in this interim report, has demonstrated that it is possible to make these in-situ measurements. Three-dimensional imagery is a useful method for estimating the quality of the reconstruction process, (i.e. high distortion and/or noise in the images indicate phase error in the wavenumber spectrum), and from the 3D dataproducts different classification training samples can be generated (e.g. Fig. 36). Though the multipass algorithms were successful, a drawback of the data captured thus far is the narrow span of grazing angles, preventing observation of significant coupling between grazing angle and target scattering strength to be observed. In FY16 this shortcoming will be addressed experimentally. Additionally a tool will be developed to generate data snippets from coherently processed multipass data, to span a selectable number of the previously mentioned sensor and noise variables. Though this technique may not be used to alter target variables such as burial depth and sediment type, it is readily perceivable that the ability to span the sensor and noise variables from in-situ measurements of the target response will aid in feature selection and by adding statistical significance to features, enhance classification performance.

Based on the successful implementation of the updated 3D co-registration and multilateration data processing algorithms on the AUV acquired field data, and the demonstrated capability to perform the necessary co-registration procedures on the multipass circular SAS data, it is recommended that the field trials listed in the Go/No-Go section of this SERDP project be funded (i.e., a Go for the FY15 to FY16 decision point).

REFERENCES

1. R. P. Stokey et al., “Development of the REMUS 600 autonomous underwater vehicle,” in Proc. IEEE OCEANS, Washington, DC, Sept. 2005.

2. T. M. Marston and J. L. Kennedy, “Volumetric acoustic imaging via circular multipass aperture synthesis,” IEEE J. Ocean. Eng., [Early Access], Feb. 2016.

3. O. Ponce, P. Prats-Iraola, M. Pinheiro, M. Rodriguez-Cassola, R. Scheiber, A. Reigber, and A. Moreira, “Fully polarimetric high-resolution 3-D imaging with circular SAR at L-Band,” IEEE Trans. Geosci. Remote Sens., vol. 52, no. 6, pp. 3074–3090, June 2014.

4. C. H. Casteel, L. A. Gorham, M. J. Minardi, S. Scarborough, and K. D. Naidu, “A challenge problem for 2D/3D imaging of targets from a volumetric data set in an urban environment,” in Proc. Algorithms for Synthetic Aperture Radar Imagery XIV. SPIE Defense and Security Symp., Orlando, FL, Apr. 9–13, 2007.

5. O. Frey, F. Morsdorf, and E. Meier, “Tomographic processing of multi-baseline P-band SAR data for imaging of a forested area,” in Proc. IGARSS, pp. 156–159,

6. T. M. Marston and J. L. Kennedy, "Correction of aperture errors in circular SAS imagery via pseudo-stripmap autofocusing," in Proc. SAS/SAR, Lerici, Italy, Sep. 2014.

7. H. Cantalloube and C. Nahum, “Multiscale local mapdrift-driven multilateration SAR autofocus using fast polar format image synthesis,” IEEE Trans. Geosci. Remote Sens., vol. 49, no. 10, pp. 3730–3736, Oct. 2011.

8. T. M. Marston and J. L. Kennedy, “TomoSAS in bathymetrically complex environments,” European Symposium on Synthetic Aperture Radar 2016 (EUSAR’16), [*accepted*].

9. T. M. Marston, J. L. Kennedy and P. L. Marston, “Autofocusing circular synthetic aperture sonar imagery using phase corrections modeled as generalized cones,” J. Acoust. Soc. Amer., vol. 136, pp. 614-622, August 2014.

10. T. M. Marston, “A correlation based autofocus algorithm for coherent circular synthetic aperture sonar,” In Proceedings of EUSAR 2012, Nuremberg, Germany, April 2012.

11. Strategic Environmental Development and Research Plan (SERDP) project MR-2439 (“Multipass and non-concentric circular synthetic aperture sonar”) FY14 Interim Report.

12. A. Ishimaru, Tsz-King Chan and Y. Kuga, “An imaging technique using confocal circular synthetic aperture radar,” IEEE Trans. Geosci. Remote Sens., vol. 36, no.5, pp. 1524-1530, Sept. 1998.

13. L. J Moore and L. C. Potter, “Three-dimensional resolution for circular synthetic aperture radar,” *Defense and Security Symposium.* International Society for Optics and Photonics, 2007.

14. J. C. V. Jakowatz et. al, *Spotlight-Mode Synthetic Aperture Radar: A signal Processing Approach.* Dordrecht, The Netherlands: Kluwer, 1996. Relevant portion can be found on pages 187 – 197.

15. R. E. Hansen, H. J. Callow, T. O. Sæbø, and S. A. V. Synnes, “Challenges in seafloor imaging and mapping with synthetic aperture sonar,” IEEE Trans. Geosci. Remote Sens., vol. 49, no. 10,pp. 3677–3687, Oct. 2011.

16. F. Simonetti, L. Huang, and N. Duric, “On the spatial sampling of wave fields with circular ring apertures,” Journal of Applied Physics, vol. 101, 083103 (2007).

17. S. F. Cotter, B. D. Rao, K. Engan, and K. Kreutz-Delgado, “Sparse solutions to linear inverse problems with multiple measurement vectors,” IEEE Transactions on Signal Processing, vol. 53, no. 7, pp. 2477-2488, 2005.

18. D. S. Plotnick, P. L. Marston, and T. M. Marston, “Fast nearfield to farfield conversion algorithm for circular synthetic aperture sonar,” J. Acoust. Soc. Amer. express letters, vol. 136, August 2014.

19. T. M. Marston and J. L. Kennedy, “TomoSAS images of acoustically penetrable objects,” European Symposium on Synthetic Aperture Radar 2016 (EUSAR’16), [*accepted*].

20. Peng et al, “V3D enables real-time 3D visualization and quantitative analysis of large-scale biological image data sets,” Nature Biotechnology, vol. 28, no. 4, p. 348-355, 2010.

21. Peng et al., “Extensible visualization and analysis for multidimensional images using Vaa3D,” Nature Protocols, vol. 9, no. 1, pp. 193-208, 2014.

22. T. G-Michael et al, “Image-based Automated Change Detection for Synthetic Aperture Sonar by Multi-Stage Co-Registration and Canonical Correlation Analysis,” IEEE J. Ocean. Eng., *accepted for publication.*

23. K. Baik and P. L. Marston, “Kirchhoff approximation for a cylinder breaking through a plane surface and the measured scattering,” IEEE J. Ocean. Eng., vol. 33, no. 4, pp. 386–396, Oct. 2008.

24. G. C. Eastland, T. M. Marston, P. L. Marston, “Evolution of acoustic feature timing and imaging for different cylinder exposures and applications of reversible SS filtering,” In Proc. IEEE OCEANS ‘10, Seattle, WA, Sept. 2010.

25. S.G. Kargl et al., “Scattering from Objects at a Water-Sediment Interface: experiment, High-Speed and High-Fidelity Models, and Physical Insight,” IEEE J. Ocean. Eng., vol. 40, no. 3, pp. 632-642, Oct. 2014.

26. Fan, Haoqiang, et al. “Learning deep face representation.” *arXiv preprint, arXiv:1403.2802* (2014).

27. A. Krizhevsky, I. Sutskever and G. E. Hinton. “ImageNet classification with deep convolutional neural networks.” *Advances in neural information processing systems.* 2012.

28. T. M. Marston, P. L. Marston, and K. L. Williams, “Scattering resonances, filtering with reversible SAS processing, and applications of quantitative ray theory,” In Proc. IEEE OCEANS ‘10, Seattle, WA, Sept. 2010.

29. TREX website: http://www.apl.uw.edu/project/project.php?id=trex13.

This article has been accepted for inclusion in a future issue of this journal. Content is final as presented, with the exception of pagination.

Volumetric Acoustic Imaging via Circular Multipass Aperture Synthesis

Timothy M. Marston and Jermaine L. Kennedy

***Abstract*—In this paper, volumetric imaging via multipass circular synthetic aperture sonar (CSAS) is demonstrated using an autonomous underwater vehicle (AUV). A multidimensional aperture is synthesized by performing a series of circular scans at varying grazing angles around targets and coherently combining the backscattering information from the set of scans to form high-resolution volumetric images. A data-driven technique for precision alignment of the individual scans comprising the multipass set enables synthesis of a multidimensional array. To beamform in the vertical dimension using the irregular and undersampled multipass aperture, a compressive-sensing-based approach is adopted which is similar to methods used in analogous synthetic aperture radar tomography applications but modified to accommodate for the wider fractional bandwidth of the synthetic aperture sonar (SAS) system. The modification exploits a joint sparsity assumption in the vertical scattering profile at different subbands and adapts a standard joint sparse solving algorithm to the relevant case in which the sparsity profile is common between solution vectors but the sensing matrices are different. Results are shown for a variety of targets, including proud and obliquely buried unexploded ordnance, a 2-1 solid aluminum cylinder, and a steel oil drum.**

***Index Terms*—Compressive sensing, multipass sonar, synthetic aperture sonar (SAS), tomography, volumetric imaging.**

I. Introduction

SYNTHETIC aperture sonar (SAS) systems transmit acoustic pulses while moving along a trajectory and coherently combine the backscattered echoes to yield high-resolution images of the seafloor [1], [2]. These images may be projected onto a flat plane or, if the system is interferometric, a height map determined via interferometry [3]. For acoustically penetrable objects or objects with sharp discontinuities in their vertical scattering profiles, multiple acoustic scatterers may map to the same pixel in a beamformed SAS image. This phenomenon, known as range layover, has been described in both SAS [4], [5] and synthetic aperture radar (SAR) literature [6] and can obscure target features, seabed features, and cause problems for interferometric height map estimation.

Manuscript received August 14, 2015; revised November 05, 2015; accepted November 13, 2015. This work was supported in part by the U.S. Office of Naval Research under Grants N000141410087 and N0001415WX00344, and the Strategic Environmental Research and Development Program under Grant #MR-2439.

Associate Editor: T. O. Sæbø.

T. M. Marston is with the Applied Physics Laboratory, University of Washington (APL-UW), Seattle, WA 98105 USA (e-mail: marston@apl.washington.edu).

J. L. Kennedy is with the Naval Surface Warfare Center, Panama City Division (NSWC-PCD), Panama City Beach, FL 32407 USA (e-mail: jermaine.kennedy@navy.mil).

Digital Object Identifier 10.1109/JOE.2015.2502664

One approach for addressing range layover and discriminating between overlapping scatterers is to build a multidimensional synthetic array by performing repeat passes at multiple altitudes or ranges and coherently combine the backscattered signals. Although theoretical and laboratory-based studies have been conducted regarding the feasibility of this approach in a SAS context [7], [8], multipass aperture synthesis has primarily been conducted and reported previously in the field of SAR, where it is commonly referred to as SAR tomography [9]. Demonstrations of SAR tomography include both airborne and spaceborne systems. Applications of spaceborne SAR tomography are being found for biomass and forest canopy research [10], and urban temporal deformation estimates [11]. Airborne tomography demonstrations showing good results are present in the literature as well [12], however airborne tomography must compensate for navigation and platform stability issues. As a result, prominent scatterers such as the array of corner reflectors described in [12] are used for navigation calibration. For the more difficult circular synthetic aperture radar (CSAR) case, isotropic scatterers such as Luneburg lenses [13] and top-hat reflectors [14] are used to provide platform motion calibration. Airborne systems also take advantage of global positioning system (GPS) localization. GPS is ineffective underwater however, and the cost and difficulty associated with introducing isotropic scatterers for navigation references underwater makes the practice rare in synthetic aperture sonar experiments, though some initial circular SAS (CSAS) experiments utilized transponders and hydrophones for similar purposes (see, e.g., [15] and [16]).

A commonly used bandwidth related assumption in SAR tomography literature is that, following deramping in the vertical dimension, the signatures from a vertically distributed set of scatterers all lie within a single range resolution cell. The phase history across the array can be related to the vertical distribution of scatterers by Fourier transform, (see [9], and Section IV), and most SAR tomography literature poses vertical beamforming as a 1-D spectral estimation problem. The relatively short and irregularly sampled apertures have resulted in a necessity for generalized spectral estimation approaches that have super resolution capability, and recent SAR tomography literature has dealt with the application of compressive sensing algorithms to the vertical beamforming problem [17], [18].

In contrast, SAS systems tend to have a much larger fractional bandwidth [19], implying that the 1-D assumption leveraged by SAR tomography algorithms may not be directly applicable to data captured from many fielded SAS systems. Furthermore, the coherent processing of multipass data must be performed without the additional aids of GPS signals or artificially introduced isotropic scatterers to serve as navigation

0364-9059 © 2016 IEEE. Personal use is permitted, but republication/redistribution requires IEEE permission.
See http://www.ieee.org/publications_standards/publications/rights/index.html for more information.

This article has been accepted for inclusion in a future issue of this journal. Content is final as presented, with the exception of pagination.

references. This paper describes methods for overcoming these difficulties by demonstration of multipass tomography from an autonomous underwater vehicle (AUV)-mounted sonar system that insonifies targets using two different scan methods: circular scans that vary in height and circular scans that vary in radius. In Section II, the experiment, the targets, and the scan patterns are described to provide context for the subsequent sections. Section III outlines a multistep process for high accuracy relative localization of the multipass scans. Section IV provides details on a wideband beamforming method for irregular apertures. The method exploits a joint sparse assumption in the scattering profiles of subbanded data to reconstruct a vertical scattering profile and reduce sidelobes. In Section V, the experimental results for the targets are examined and the results of using the different scan patterns are compared. Finally, conclusions and future research directions will be presented in Section VI.

II. Experiment Details

In December 2014, a series of multipass SAS experiments were conducted in 20 m of water off the coast of Panama City Beach, FL, USA. The utilized SAS system has two operational frequency bands: a high-frequency band with a center frequency in the hundreds of kilohertz and a low-frequency band with a center frequency in the tens of kilohertz. The SAS was mounted on a REMUS 600 AUV [20]. The data in this paper come from the high-frequency band.

Two scan patterns were employed, both based around the concept of CSAS (see [15], [16], and [21]). In CSAS operations, the sonar platform moves in a circle around a target of interest, insonifying the target from all aspect angles. From the backscattered echoes, SAS images with improved resolution, speckle, and target features can be acquired. CSAS images are often processed in a "semicoherent" manner, i.e., a series of coherently generated intensity images corresponding to different target looks are incoherently combined to generate a full aperture image (see, e.g., [22] and [23]). Most of the results in this paper have been processed in this manner.

The first scan pattern fixes the radii at 30 m and varies the altitudes from 4.5 to 6.9 m in steps of 0.3 m. The second pattern fixes the altitudes at 5.95 m and varies the radii from 27 to 35 m in steps of 1 m. The second, less orthodox approach is tested because the depth of the sensor can remain fixed, which may have some advantages for a SAS system mounted on a tow-fish. The SAS system has a pair of identical, vertically spaced receiver arrays resulting in 18 scans total for both configurations. Fig. 1 graphically depicts the scan patterns.

The navigation coordinates of the AUV are initialized at the surface via GPS. Following submersion, navigation relies on a fusion of information from a Doppler velocimeter and an inertial navigation system (INS).

The sediment in the experiments is sand. Four targets were scanned: a proud 155-mm Howitzer shell with an end-cap, a partially buried 155-mm Howitzer shell oblique at 55°, a proud 2-1 solid aluminum cylinder, and a vertically oriented steel barrel. Both howitzers had a 1/4-in-thick nylon rope looped twice and tied around their midsection.

III. Aperture Localization

A data-driven algorithm was developed for the purpose of localizing the aperture samples to the precision necessary for coherent multipass aperture synthesis. The algorithm has two primary phases of operation: a coarse rotation and translation stage and a fine radial and angular alignment stage that also estimates medium propagation speed discrepancies. It is assumed that, prior to application of the algorithm, the coordinates of each circular pass have been estimated to sufficient accuracy that images made from the individual scans are free of significant focus aberrations. In circular synthetic aperture processing, this can be accomplished by applying data-driven micronavigation methods [24], [25] in conjunction with autofocusing techniques that further refine the navigation estimates [26], [27], and [28].

In this paper, the cylindrical coordinate system is used for describing aperture sample locations. In subsequent equations, the term r denotes radial distance from the origin in meters with the positive direction denoting the direction toward the sonar platform, θ denotes angle in radians, and h denotes displacement in the height dimension.

A. Coarse Rotation and Translation

Following navigation estimation for the individual scans the coordinate frames of each scan must be unified. The subsequent steps are used to perform a coarse unification: 1) a reference scan is selected; 2) the remaining scans are rotationally aligned with the reference using the envelopes of the temporal spectra; and 3), ground-plane images are formed and correlated to estimate relative translations. Each step will be examined in more detail in the following sections.

1) Selection of a Reference Scan: A reference scan is chosen to represent the true coordinate frame, and the aperture coordinates of all other scans ("compliant" scans) will be aligned with the coordinates of the reference scan. In each of the examples in this paper, the reference scan was chosen to be the scan with the median radius or altitude. In subsequent steps, subscripts are used to denote the scan number out of N scans, the upper (U) or lower (L) array, and whether a scan is a reference or a compliant scan. For each set of scans there is only a single reference data set, which always corresponds to data from the lower receiver array of the scan with the median altitude or radius, so the additional subscripts are dropped. As an example a reference scan would be denoted S_{ref} and the upper stave data from the nth scan of a set would be denoted $S_{\mathrm{comp_}nU}$.

The utilized sonar system has both upper and lower receive arrays, and in the current implementation of the algorithm the described alignment process is only applied to data from the lower array. The distance between the upper and lower arrays is fixed based on the physical dimensions of the sonar system, and if the coordinates of the lower array elements are known it is possible to estimate with high accuracy the coordinates of the upper array.

2) Coarse Rotational Alignment: Via the projection slice theorem, in a CSAS context the 1-D Fourier transform of an echo in the temporal (range) dimension measured at aperture

This article has been accepted for inclusion in a future issue of this journal. Content is final as presented, with the exception of pagination.

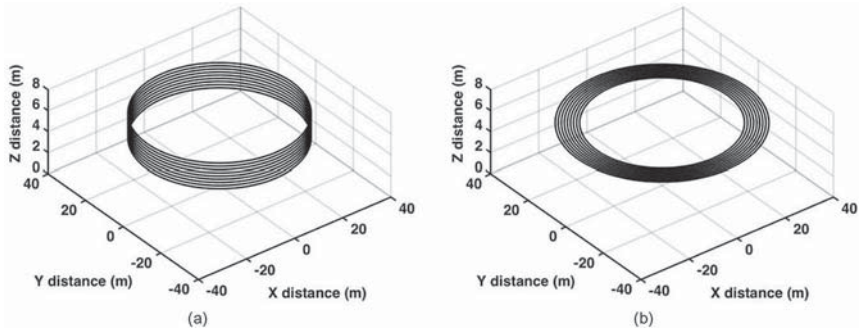

Fig. 1. The scan patterns used in the multipass beamforming experiments. The scans in (a) fix the radius at 30 m and span 2.4 m in altitude. The scans in (b) fix the altitude at 5.95 m and span 8 m in radius.

angle θ corresponds to the central slice at angle θ through the 2-D spatial spectrum of the image reflectivity function [21]. Using this principle, a coarse rotational offset can be found by calculating the 1-D Fourier spectrum of the raw compliant scan data in the time (t)-dimension, two-dimensionally correlating this data with the temporal spectrum of the reference, and measuring the angular (along-track) offset of the correlation peak.

In the present algorithm, the spectral magnitudes are used to reduce sensitivity of the results to translational offsets, which manifest in the spectral phase [28]. During implementation a time gate and azimuthal filter is applied to the reference and compliant scan data, reducing the radial extent of the data used for alignment. Near-field effects can cause decorrelation if the origins of the scans are not aligned, and for this reason a simple linear narrowbeam motion compensation (mocomp) followed by a far-field conversion is applied to the data before rotational alignment. An examination of near-field error for circular synthetic apertures, and a derivation of an efficient far-field conversion method can be found in [29]. The correlation process is summarized in

$$\mathcal{M}_n(\theta,t) = \mathcal{F}^{-(2)}\left\{\mathcal{F}^{(2)}\left\{\left|\mathcal{F}_t\left\{\hat{S}_{\mathrm{ref}}(\theta,t)\right\}\right|\right\} \times \mathcal{F}^{(2)}\left\{\left|\mathcal{F}_t\left\{\hat{S}_{\mathrm{comp_}nL}(\theta,t)\right\}\right|\right\}^*\right\}. \quad (1)$$

in which $\mathcal{F}^{(2)}$ represents a 2-D fast Fourier transform (FFT), $\mathcal{F}_t$ represents the 1-D FFT in the temporal dimension, $||$ represents the absolute value, and an asterisk ($*$) represents the complex conjugate. In (1), $\hat{S}_{\mathrm{ref}}$ and $\hat{S}_{\mathrm{comp_}nL}$ are the raw, motion corrected complex lower array data from the reference and nth compliant scans after application of a far-field conversion derived in [29]

$$\hat{S}(\theta,t) = \mathcal{F}^{-(2)}\left\{\mathcal{F}^{(2)}\{S(\theta,t)\}_m e^{-i\left(\frac{4m^2-1}{16kR}\right)}\right\} \quad (2)$$

where k is the acoustic wave number $2\pi f/c$, (f is frequency in hertz, and c is the sound speed in meters per second), R is the circle radius in meters, and m spans $-M/2$ to $M/2$, where M is the number of samples in the angle dimension. Note that in [29] the expression for (2) differs slightly due to the wave number convention. In (1), the matrix $\mathcal{M}(\theta,t)$ has a correlation peak with a location in the θ-dimension that matches the rotational offset of the two scans. This offset is applied to the compliant set to rotationally align the coordinate frames

$$\overline{\theta}_{\mathrm{comp_}nU,L} = \theta_{\mathrm{comp_}nU,L} + \Delta\theta_{\mathrm{MAX}\{\mathcal{M}_n(\theta,t)\}} \quad (3)$$

where $\Delta\theta_{\mathrm{MAX}\{\mathcal{M}_n(\theta,t)\}}$ is the offset angle, corresponding to the location of the maximum value of the correlation matrix $\mathcal{M}_n(\theta,t)$, and $\overline{\theta}_{\mathrm{comp_}nU,L}$ is the updated set of angular coordinates for the upper and lower array locations of the nth compliant scan.

Algorithm 1. Coarse rotational alignment

Step 1. Preprocess data from the nth scan (mocomp, time gate, far-field conversion).
Step 2. Compute a 1-D Fourier transform of the data in the temporal (range) dimension.
Step 3. Compute the magnitudes of the spectral data.
Step 4. Perform a 2-D cross correlation with the magnitudes of the reference scan spectrum.
Step 5. Find the location of the correlation peak and isolate the angular component $\Delta\theta$.
Step 6. Rotate the navigation coordinates around the polar origin by $\Delta\theta$.

3) Coarse Translational Alignment: The translational offset between the origins of the reference scan and rotationally aligned nth compliant scan can be found by cross correlating images of the sediment reflectivity function near the origin. To generate images, the temporal spectra of the motion compensated and far-field converted raw data are mapped from polar to Cartesian coordinates as described in [21]

$$\hat{S}(\theta,f) \rightarrow \hat{S}(k_x,k_y) \quad (4)$$

where the coordinate mapping is defined as

$$k_x = \frac{4\pi}{c} f\cos\theta \quad (5)$$

$$k_y = \frac{4\pi}{c} f\sin\theta \quad (6)$$

and $\hat{S}$ is the far-field converted temporal Fourier transform of the time gated, motion compensated raw data

$$\hat{S}(\theta,f) = \mathcal{F}_t\left\{\hat{S}(\theta,t)\right\}. \quad (7)$$

The coordinate remapping is performed via 2-D interpolation. An inverse 2-D Fourier transform converts the interpolated wave number data to the spatial domain. The relative

This article has been accepted for inclusion in a future issue of this journal. Content is final as presented, with the exception of pagination.

Algorithm 2. Coarse translational alignment

Step 1. Preprocess data from the nth scan (mocomp, time gate, far-field conversion).
Step 2. Compute a Fourier transform of the data in the temporal (range) dimension.
Step 3. Map complex spectral data to the spatial wave number domain via (4)–(6).
Step 4. Perform an inverse 2-D Fourier transform to generate an image.
Step 5. Perform a 2-D cross correlation with the reference scan image.
Step 6. Measure Cartesian translations Δx and Δy from the location of the correlation peak.
Step 7. Convert the Cartesian translations to a navigation update in polar coordinates.

translational offsets between scans are found by 2-D cross correlation of the reference and compliant scan magnitude images

$$\mathcal{N}_n(x,y) = \mathcal{F}^{-(2)}\left\{\mathcal{F}^{(2)}\left\{\left|\mathcal{F}^{-(2)}\left\{\hat{S}_{\mathrm{ref}}(k_x,k_y)\right\}\right|\right\} \times \mathcal{F}^{(2)}\left\{\left|\mathcal{F}^{-(2)}\left\{\hat{S}_{\mathrm{comp_}nL}(k_x,k_y)\right\}\right|\right\}^*\right\}. \quad (8)$$

The X and Y translations are found via the location of the coordinate of the correlation peak and converted to a navigation update

$$\overline{r}_{\mathrm{comp_}nL,U} = r_{\mathrm{comp_}nL,U} + \Delta x_{\mathrm{MAX}\{\mathcal{N}_n(x,y)\}}\cos\theta_{\mathrm{comp_}nL,U} + \Delta y_{\mathrm{MAX}\{\mathcal{N}_n(x,y)\}}\sin\theta_{\mathrm{comp_}nL,U}, \quad (9)$$

where $\Delta x_{\mathrm{MAX}\{\mathcal{N}_n(x,y)\}}$ is the offset in the x-dimension in meters indicated by the peak of the correlation matrix, $\Delta y_{\mathrm{MAX}\{\mathcal{N}_n(x,y)\}}$ is the offset in the y-dimension, and $\overline{r}_{\mathrm{comp_}nL,U}$ is the updated set of radial coordinates for the upper and lower stave data of the nth compliant scan.

B. Fine Alignment

A method for correcting localized residual rotation and translation errors and estimating fine scale medium propagation speed corrections is introduced in this section. There are many similarities to redundant phase center (RPC) micronavigation (see, e.g., [25]). The outline for the fine alignment process is as follows.

1. The raw data are ping-wise backprojected to a regular grid in cylindrical coordinates.
2. Local angular offset errors are estimated from azimuthal displacement measurements made via patch-wise correlations between the reference and compliant data sets.
3. Radial, height, and medium speed compensations are estimated via decomposition of radial shift measurements into a set of basis functions parametrizing the range variance of the different errors.

Each step will be described in detail in the following sections.

1) Grid Interpolation: To facilitate measurement of the relative residual localization errors between sets, the data are first interpolated onto a common ground-plane grid in cylindrical coordinates. The grid has a uniform height of $h = 0$, spans a predefined radius, and angularly spans 0 to 2π radians. The transformation from time units to radial units is shown in

$$S(\theta,t) \rightarrow S(\theta,\mathrm{r}) \quad (10)$$

$$r = R(\theta) - \sqrt{\left(\frac{tc}{2}\right)^2 - \left(h_{\mathrm{sonar}}(\theta)\right)^2} \quad (11)$$

where R and h_{sonar} are the radius and height above the grid of the sonar at the aperture angle θ. This transformation is a slant-range to ground-range interpolation, however the range direction sign is flipped, and in (11), the positive radial direction extends from the origin toward the sonar platform.

Following radial interpolation the data are interpolated in the angular dimension to make the data both regular in θ and consistent in the number of samples with the reference set. The reference set and all compliant sets are then lowpass filtered and decimated in the angular dimension to narrow the acoustic beam around the origin and reduce the computational burden of the patch-wise correlations used in subsequent steps.

2) Fine Angular Localization: Residual along track navigation errors cause inaccuracies in the angular coordinates of the aperture samples. These errors are estimated via patch-wise 2-D complex cross correlation between the gridded reference and compliant sets. Each gridded data set is binned into a set of patches $O^{(I,J)}$, where I and J are the indices denoting the individual patches. Patches from the reference set are correlated with the corresponding patches from each of the compliant sets using normalized circular cross correlation

$$\mathcal{P}_n^{(I,J)} = \frac{\left|\mathcal{F}^{-(2)}\left\{\mathcal{F}^{(2)}\left\{O_{\mathrm{ref}}^{(I,J)}\right\}\mathcal{F}^{(2)}\left\{O_{\mathrm{comp_}nL}^{(I,J)}\right\}^*\right\}\right|}{\sqrt{\sum\left|O_{\mathrm{ref}}^{(I,J)}\right|^2\sum\left|O_{\mathrm{comp_}nL}^{(I,J)}\right|^2}}. \quad (12)$$

The locations of the correlation peaks in $\mathcal{M}^{(I,J)}$ indicate the relative displacements between the patches. In the current implementation, the patch dimensions are 31×37 samples in the angle and radial dimensions. As performed [30], parabolic interpolation is used to refine the displacement estimate to subpixel precision, i.e., if K and L are the patch dimensions in the angular and radial dimensions, and k_0 and l_0 are the indexes in the correlation matrix corresponding to the peak, then the refined angular offset $\Delta\tilde{\theta}(I,J)$ for the (I,J)th patch is estimated to subpixel precision via (13), shown at the bottom of the page, where $\delta\theta$ is the pixel spacing in the angular dimension.

The value of the correlation peak in $\mathcal{P}_n^{(I,J)}$ is a measure of patch-wise signal coherence and can be used to weight the

$$\Delta\tilde{\theta}(I,J) = \left(k_0 - \frac{\mathcal{P}_n^{(I,J)}[k_0+1,l_0] - \mathcal{P}_n^{(I,J)}[k_0-1,l_0]}{2\left(\mathcal{P}_n^{(I,J)}[k_0+1,l_0] - 2\mathcal{P}_n^{(I,J)}[k_0,l_0] + \mathcal{P}_n^{(I,J)}[k_0-1,l_0]\right)}\right)\delta\theta \quad (13)$$

This article has been accepted for inclusion in a future issue of this journal. Content is final as presented, with the exception of pagination.

Algorithm 3. Local angular alignment

Step 1. Interpolate raw data to a planar grid in cylindrical coordinates with regular spacing in θ and r, and having a height equal to the average ground plane (defined as $h = 0$).
Step 2. Filter and decimate in the θ-dimension.
Step 3. Subdivide the data into large (e.g., $\sim$30 $\times$ 40 pixels) patches.
Step 4. Perform 2-D cross correlation between the patches of the nth and reference scans.
Step 5. Generate a matrix of shifts in the θ-dimension using the locations of the correlation peaks.
Step 6. Generate a weighting matrix using the values of the correlation peaks.
Step 7. Perform a weighted average of angular shift values to estimate the local angular coordinate corrections.
Step 8. Update the angular coordinates of the nth scan: $\overline{\theta} = \theta + \Delta\tilde{\boldsymbol{\theta}}(\theta)$.
Step 9. Iterate Steps 1–8 a set number of times or until a convergence criterion has been met.

radial displacement estimates. The estimated angular error for each aperture coordinate is calculated via a coherence-weighted average in the radial dimension

$$\Delta\tilde{\theta}^{I}_{\text{comp_}nL} = \frac{1}{\sum_J w^{(I,J)}} \sum\nolimits_J w^{(I,J)} \Delta\tilde{\theta}^{(I,J)} \tag{14}$$

where $\Delta\tilde{\theta}^{(I,J)}$ is the matrix of angular displacements estimated from the peaks of $\mathcal{P}_n^{(I,J)}$ and $w^{(I,J)}$ is the weighting matrix of coherence values, where values less than 0.15 are forced to a weight of zero. Following the along-track shift estimate, the angular coordinates for the compliant sets are updated by

$$\overline{\theta}_{\text{comp_}nL,U} = \theta_{\text{comp_}nL,U} + \Delta\tilde{\boldsymbol{\theta}}_{\text{comp_}nL,U}\left(\theta_{\text{comp_}nL,U}\right). \tag{15}$$

The displacement estimation process may be iterated to refine the angular localization. In the current implementation the process is iterated twice.

3) Fine Radial, Height, and Propagation Speed Corrections: Radial displacements between backprojected data sets are measured using the same patch-wise correlation technique described in Section III-B2, however the patch sizes are reduced to 7 by 31 samples, and correlations occur between adjacent scans rather than between the reference and each compliant scan. This reduces the grazing angle disparity and temporal baseline between the scans, increasing the coherence between data sets. The coordinates of the compliant scans relative to the reference scan are found by integrating the offsets measured between scans.

Similar to RPC micronavigation, regression analysis is used in conjunction with a nonlinear model to estimate array and propagation speed corrections. The model for radial and height aperture localization errors and bulk sound speed propagation errors is illustrated in Fig. 2.

In Fig. 2, the black dot represents the height h_s and radial location R of the reference aperture at some angular coordinate

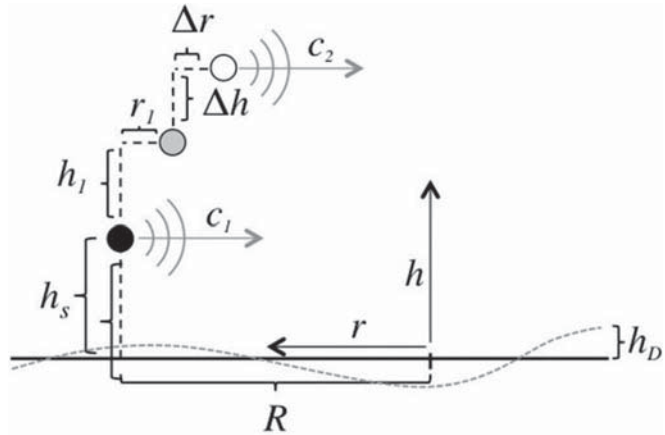

Fig. 2. The aperture localization error model, with the radius (r) and height (h) axes labeled. The black dot is the location of the reference scan, the gray dot is the initial estimate of the location of a compliant scan, and the white dot is the true location of the compliant scan.

θ. The gray dot, which represents the initial estimate of the relative location of a compliant scan at the same angular coordinate, has an initially estimated vertical offset h_1 and radial offset r_1 relative to the reference scan. The true location of the compliant scan, plotted as the white dot, has an offset of $h_1 + \Delta h$ and $r_1 + \Delta r$ relative to the reference. The height of the sediment relative to the ground plane is labeled in Fig. 2 as h_D and varies as a function of θ and r.

Fig. 2 also shows average sound speeds c_1 and c_2 associated with the reference and compliant scan aperture locations. Either due to inaccuracies and drift in the onboard CTD or inhomogeneities in the water column, the sound speeds measured at each scan varied enough to bias localization estimates between scans. To compensate for this biasing a sound-speed correction term $\sigma = c_1/c_2 - 1$ was added to the error model.

The correlation-based radial displacement measurements represent a difference between the radial displacement residuals resulting from mapping the reference and compliant scan data to the flat plane $h = 0$

$$\rho_{\text{cor}} = \rho_{\text{ref}} - \rho_{\text{comp}} \tag{16}$$

$$\rho_{\text{ref}} = \sqrt{D_{\text{ref}}^2 - {h_S}^2} - \sqrt{\check{D}_{\text{ref}}^2 - {h_S}^2} \tag{17}$$

and

$$\rho_{\text{comp}} = \sqrt{D_{\text{comp}}^2 - (h_S + h_i)^2} - \sqrt{\check{D}_{\text{comp}}^2 - (h_S + h_i)^2} \tag{18}$$

where ρ_{cor} represents the radial variation of the ground-range shifts measured via patch correlations, ρ_{ref} represents the residual difference between the true ground-range location of a scatterer having a slant range of D_{ref} and its assigned location during flat-bottom data gridding [i.e. the interpolation step described by (10) and (11)], and ρ_{comp} is analogous case for the compliant scan in which the values of Δr, Δh, and σ contribute to the true slant-range values of the scatterers and thus

This article has been accepted for inclusion in a future issue of this journal. Content is final as presented, with the exception of pagination.

the residual. The true slant range D and the flat-bottom assigned slant-range $\check{D}$ to scatterers at ground range r_g are defined

$$D_{\text{ref}} = \sqrt{r_g^2 + (h_S - h_d(r_g))^2} \tag{19}$$

$$\check{D}_{\text{ref}} = \sqrt{r_g^2 + {h_S}^2} \tag{20}$$

$$D_{\text{comp}} = (1+\sigma) \times \sqrt{(r_g + r_1 + \Delta r)^2 + (h_S - h_d(r_g) + h_1 + \Delta h)^2} \tag{21}$$

$$\check{D}_{\text{comp}} = \sqrt{(r_g + r_1)^2 + (h_S + h_1)^2} \tag{22}$$

and the ground-range variable r_g is defined

$$r_g = R(\theta) - r. \tag{23}$$

Assuming $\sigma \ll 1$, the model for the patch-measured radial shifts with unknown variables Δr, Δh, and σ and input parameters $h_D(r_g)$, sonar height h_s, and initial compliant scan height and radial offsets h_1 and r_1 can be expressed as a function of r_g in (24), shown at the bottom of the page.

Similar to the redundant phase center processing technique described in [25], the present goal is to estimate the parameters Δr, Δh, and σ via regression of the correlation-based shift measurements with the nonlinear model in (24). To do this efficiently, (24) can be linearly expanded around initial values Δr_0, Δh_0, and σ_0, shown in (25)–(30), at the bottom of the page.

The radial displacements estimated from patch-wise correlation are assembled into an $I \times J$ matrix $\tilde{\rho}$ where I is the number of patches in the angular dimension and J is the number of patches in the radial dimension. Each row $1 \le i \le I$ of the measured radial displacement matrix can be approximated as a linear combination of the perturbation bases and noise $\epsilon(r_g)$

$$\tilde{\rho}_i \approx \psi_i + \psi_{0i} + \zeta_{\Delta h_i}(\Delta h_i - \Delta h_{0i}) + \zeta_{\Delta r_i}(\Delta r_i - \Delta r_{0i}) + \zeta_{\sigma_{\text{i}}}(\sigma_{\text{i}} - \sigma_{0i}) + \epsilon_i. \tag{31}$$

Estimates for Δr, Δh, and σ can be found using a weighted least squares inversion, i.e.,

$$\begin{bmatrix} \Delta\tilde{r}_i \\ \Delta\tilde{h}_i \\ \tilde{\sigma}_i \end{bmatrix} = \left(\begin{bmatrix} \zeta_{\Delta r_i} \\ \zeta_{\Delta h_i} \\ \zeta_{\sigma_i} \end{bmatrix} \cdot \left[(w_i \circ \zeta_{\Delta r_i})^T \ (w_i \circ \zeta_{\Delta h_i})^T \ (w_i \circ \zeta_{\sigma_i})^T \right] \right)^{-1} \cdot \begin{bmatrix} (w_i \circ \zeta_{\Delta r i})^T \\ (w_i \circ \zeta_{\Delta h_i})^T \\ (w_i \circ \zeta_{\sigma i})^T \end{bmatrix} \cdot \tilde{\xi}_i^T. \tag{32}$$

In (32), w_i is the ith row of w, an $I \times J$ matrix of weights associated with each shift measurement; $\circ$ is the Hadamard product; superscript ^{T} represents the transpose operator; $\Delta\tilde{r}_i$, $\Delta\tilde{h}_i$, and $\tilde{\sigma}_i$ are the estimates fitted from the ith row of radial displacements; $\zeta_{\Delta r_i}$, $\zeta_{\Delta h_i}$, and $\zeta_{\sigma i}$ are the ith row bases functions; and $\tilde{\xi}_i$ is the ith row of displacement measurements plus a modification term that will be discussed shortly. A least squares fit to the nonlinear equation (24) can be found by initializing Δr_{0i}, Δh_{0i}, and σ_{0i} to zero, solving for $\Delta\tilde{r}_i$, $\Delta\tilde{h}_i$, and $\tilde{\sigma}_i$ using (32), updating the expansion points, re-solving and iterating this process to convergence.

From (31), there are multiple ways for defining $\tilde{\xi}_i$ as iterations progress. In the current case, rather than solving for $(\Delta r_i - \Delta r_{0i})$, $(\Delta h_i - \Delta h_{0i})$, and $(\sigma_i - \sigma_{0i})$ at each iteration and accumulating the subsequent corrections to estimate a final solution, the initial estimates are used to redefine the measurement curve $\tilde{\xi}_i$ as follows:

$$\tilde{\xi}_i = \tilde{\rho}_i - (\psi_i + \psi_{0i} + \Delta r_{0i}\zeta_{\Delta r_i} + \Delta h_{0i}\zeta_{\Delta h_i} + \sigma_{0i}\zeta_{\sigma_i}). \tag{33}$$

Using this updating definition for $\tilde{\xi}$, the full values of Δr, Δh, and σ are estimated directly every iteration. Equation (24) is not highly nonlinear over the expected range of values (e.g.,

$$\rho_{\text{cor}}(r_g) = \sqrt{r_g^2 - 2h_S h_d(r_g) + h_d(r_g)^2} + r_1 \ldots - \sqrt{(1+2\sigma)((r_g + r_1 + \Delta r)^2 + (h_S - h_d(r_g) + h_1 + \Delta h)^2) - (h_S + h_1)^2} \tag{24}$$

$$\rho_{\text{cor}}(r_g) \approx \psi + \psi_0 + \zeta_{\Delta r}(r_g)(\Delta r - \Delta r_0) + \zeta_{\Delta h}(r_g)(\Delta h - \Delta h_0) + \zeta_\sigma(r_g)(\sigma - \sigma_0) \tag{25}$$

$$\zeta_\sigma(r_g) = \frac{(r_g + r_1 + \Delta r_0)^2 + (h_S - h_d(r_g) + h_1 + \Delta h_0)^2}{\psi_0} \tag{26}$$

$$\zeta_{\Delta r}(r_g) = \frac{(r_g + r_1 + \Delta r_0)(1 + 2\sigma_0)}{\psi_0} \tag{27}$$

$$\zeta_{\Delta h}(r_g) = \frac{(h_S - h_d(r_g) + h_1 + \Delta h_0)(1 + 2\sigma_0)}{\psi_0} \tag{28}$$

$$\psi(r_g) = \sqrt{r_g^2 - 2h_S h_d(r_g) + h_d(r_g)^2} + r_1 \tag{29}$$

$$\psi_0(r_g) = -\sqrt{(1+2\sigma_0)\left((r_g + r_1 + \Delta r_0)^2 + (h_S - h_d(r_g) + h_1 + \Delta h_0)^2\right) - (h_S + h_i)^2}. \tag{30}$$

This article has been accepted for inclusion in a future issue of this journal. Content is final as presented, with the exception of pagination.

several centimeters for Δr, Δh, and < 0.01 for σ) and the changes to the variables that occur every iteration tend to be small fractions of their total values. This allows parameter estimates from adjacent aperture samples to be coupled at each iteration by jointly solving the linear equations for every row i and applying some fixed form of regularization bounding their variation. In other words, (32) can be modified to combine all rows $i = 1, 2, \ldots, I$, and replaced with

$$\hat{S} = \left(\zeta^T \cdot (\tilde{w} \circ \zeta) + \gamma_s \chi\right)^{-1} \cdot (\tilde{w} \circ \zeta)^T \cdot \tilde{\xi}_{\text{row}}^T \tag{34}$$

where $\tilde{\xi}_{\text{row}}$ is the row vector formed by concatenating each $\tilde{\xi}_i$

$$\tilde{\xi}_{\text{row}} = \left[\tilde{\xi}_1, \tilde{\xi}_2, \ldots, \tilde{\xi}_I\right] \tag{35}$$

and the solution vector $\hat{S}$ is

$$\hat{S} = \left[\Delta\tilde{r}_{1\ldots I}, \Delta\tilde{h}_{1\ldots I}, \tilde{\sigma}_{1\ldots I}\right]^T. \tag{36}$$

ζ now represents a matrix containing a set of basis functions that update uniquely for each row i depending on the parameter estimates from the previous iteration, in (37), shown at the bottom of the page.

Each of the bases functions is transposed to become $J \times 1$ column vectors; therefore, ζ is an $IJ \times 3I$ matrix. The weighting matrix $\tilde{w}$ has identical structure to the bases matrix, but the bases vectors are replaced with the rows of w, the $I \times J$ matrix of weights associated with each patch correlation. The $3I \times 3I$ regularization matrix χ can be used to penalize unrealistic behavior in the solution vector $\tilde{S}$. A simple example is when χ is set to a symmetric second-order difference matrix

$$\chi = \begin{bmatrix} 2 & -1 & 0 & \cdots & 0 & -1 \\ -1 & 2 & -1 & 0 & \cdots & 0 \\ 0 & -1 & 2 & & & \vdots \\ \vdots & 0 & & \ddots & & 0 \\ 0 & \vdots & & & 2 & -1 \\ -1 & 0 & \cdots & 0 & -1 & 2 \end{bmatrix}. \tag{38}$$

When defining χ as in (38), the second-order difference of the solution vector can be limited by increasing the value of the smoothness regularization parameter γ_s. This version of regularization can be used to penalize impulsive or jittery solutions that do not tend to naturally occur as a result of platform inertia.

The values of the weighting matrix w are initialized as the correlation coefficients associated with each patch pair. Use of the correlation coefficients to weight the inversion adds some degree of robustness to the parameter estimation process (see, e.g., RPC correlation weighting in [25]) however the limited number of sample points in the correlation patches causes these values to bias high, especially in the event of very low correlation. This can still cause outliers to have an exaggerated affect on the regression results. In the present implementation, the reweighting strategy described in [30] is used to iteratively redefine the values of the weights

$$w_k = \frac{w}{\left(\tilde{S}\zeta - \tilde{\xi}_{\text{row}}^T\right)^2 + \gamma_w}. \tag{39}$$

Note that for (39) to be implemented the numerator needs to be reshaped into an $I \times J$ matrix or the numerator needs to be shaped into an $IJ \times 1$ column vector to perform the division, before forming the updated weighting matrix $\tilde{w}$ from the columns of w_k.

The resulting weighting values reject outliers and points that do not fit well with the model. How strongly outliers are rejected depends on the value of the regularization parameter γ_w. The combination of iterative reweighting and iterative convergence toward a nonlinear fit results in a series of nested iteration loops: an inner loop that updates w to reject outliers and an outer loop that converges toward the nonlinear least squares solution. Fig. 3 is a comparison of aperture displacement estimates found via the coupled and uncoupled approaches. For the coupled approach the results in Fig. 3 were obtained by defining the matrix χ as in (38) and setting the regularization parameter γ_s to a value of 0.001.

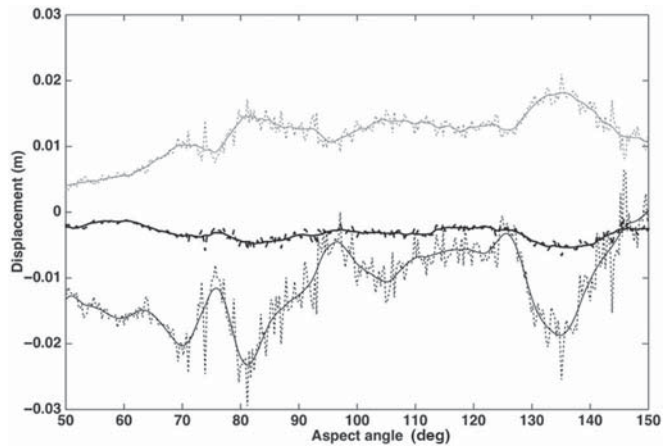

Fig. 3. A 100° segment of the full aperture (360°) estimate for the radial (black), height (gray), and sound-speed induced [bold black, calculated at 30 m using $\sigma(\theta)$] displacements. Solid lines indicate solutions incorporating smoothness regularization and dashed lines indicate unregularized solutions that were calculated independently for each aperture location.

$$\zeta = \begin{bmatrix} {\zeta_{\Delta r1}}^T & 0 & \cdots & 0 & {\zeta_{\Delta h1}}^T & 0 & \cdots & 0 & {\zeta_{\sigma 1}}^T & 0 & \cdots & 0 \\ 0 & {\zeta_{\Delta r2}}^T & & & 0 & {\zeta_{\Delta h2}}^T & & & 0 & {\zeta_{\sigma 2}}^T & & \\ \vdots & & \ddots & & \vdots & & \ddots & & \vdots & & \ddots & \\ 0 & & & {\zeta_{\Delta rI}}^T & 0 & & & {\zeta_{\Delta hI}}^T & 0 & & & {\zeta_{\sigma I}}^T \end{bmatrix}. \tag{37}$$

This article has been accepted for inclusion in a future issue of this journal. Content is final as presented, with the exception of pagination.

Algorithm 4. Local radial, height, and medium corrections

Step 1. Interpolate raw data to a planar grid in cylindrical coordinates with regular spacing in θ and r, and having a height equal to the average ground plane (defined as $h = 0$).
Step 2. Filter and decimate in the θ-dimension.
Step 3. Subdivide the data into small (e.g., $\sim 10 \times 30$ pixels) patches.
Step 4. Perform 2-D cross correlation between the patches of the nth and reference scans.
Step 5. Generate a matrix of shifts in the r-dimension using the locations of the correlation peaks.
Step 6. Generate a weighting matrix using the values of the correlation peaks.
Step 7. Using the linearized model of (33) in conjunction with the regularized surface fitting approach in (34), estimate navigation and medium correction parameters $\Delta r(\theta)$, $\Delta h(\theta)$, and $\tilde{\sigma}(\theta)$.
Step 8. Reinterpolate to the ground-plane grid using the updated navigation coordinates and medium speed corrections.
Step 9. Repeat Steps 2–8 a set number of times or until a convergence criterion has been met.

Note that the sound-speed-induced displacements shown in Fig. 3 appear to be correlated to the navigation parameters. This may be because the bases in (25) do not fully describe all phenomena causing radial displacements and unmodeled effects such as sound-speed profiles may cause coupling. Another possible cause may be the autofocusing procedure used for refining the coordinate estimates of each scan. The autofocus-based navigation refinement process used for the individual scans cannot distinguish between sound-speed errors and navigation errors and some degree of coupling between the values may occur at that point of the signal processing chain.

Section IV will describe how the multipass data can be used in conjunction with the localized aperture coordinates to generate volumetric images.

IV. Wideband Sparse Beamforming

For a given multipass spacing, the diameter of a distribution of vertical scatterers that can be tomographically reconstructed without aliasing is [31]

$$D < \frac{\lambda}{2\,(\Delta\Theta)} \tag{40}$$

where λ is the wavelength in meters at the maximum frequency of the sonar bandwidth: $(f_0 + f_{BW}/2)/\mathrm{c}$, $\Delta\Theta$ is the grazing angle variation between multipass scans, and D is the diameter of the scatterer distribution. [The relationship between (40) and a similar sampling criterion found in SAR literature is shown in the Appendix.] The experimentally realized aperture is irregular, with $\Delta\Theta$ being determined both by the repeat pass scan geometry and the distance between the vertically spaced receiver arrays physically mounted on the AUV. The transmitter and receivers form a weakly bistatic array in the vertical dimension, thus the physical baseline $\Delta h_{rc\nu}$ has an equivalent monostatic baseline of $\Delta h_{rc\nu}/2$ via the phase center approximation [24]. For the nth scan in a multipass aperture using the patterns described in Section II the values of $\Delta\Theta$ vary between

$$\Delta\Theta_{\mathrm{intf}} = \tan^{-1}\left(\frac{h_n + \Delta h_{h_{rc\nu}}/2}{R_n}\right) - \tan^{-1}\left(\frac{h_n}{R_n}\right) \tag{41}$$

and

$$\Delta\Theta_{\mathrm{scan}} = \tan^{-1}\left(\frac{h_{n+1}}{R_{n+1}}\right) - \tan^{-1}\left(\frac{h_n + \Delta h_{h_{rc\nu}}/2}{R_n}\right). \tag{42}$$

For a hypothetical SAS system with $f_0 = 175$ kHz, $f_{BW} = 50$ kHz, and $\Delta h_{rc\nu} = 0.1$ m, similar to the high-frequency band SAS used in the experiments, $D_{\mathrm{scan}} = 0.46$ m and $D_{\mathrm{intf}} = 2.3$ m for the altitude pattern in Section II and $D_{\mathrm{scan}} = 0.65$ m and $D_{\mathrm{intf}} = 2.2$ m for the radial pattern. In these examples, $\Delta\Theta_{\mathrm{scan}}$ is sufficient for small unexploded ordnance (UXO), but insufficient for many mine-like shapes and clutter objects. In contrast, $\Delta\Theta_{\mathrm{intf}}$ is large enough to encompass many mine-like shapes and clutter objects.

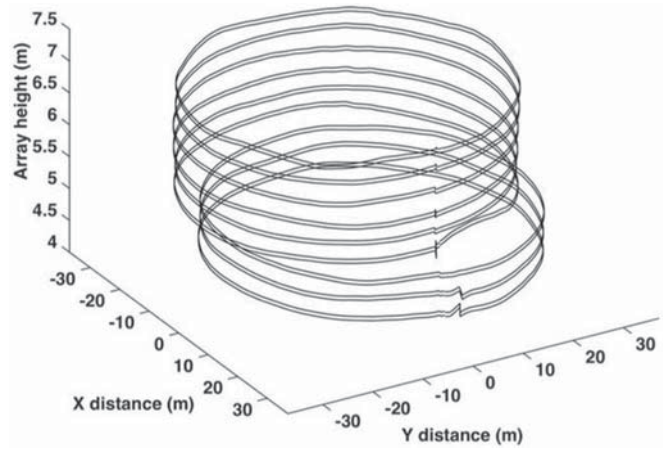

Fig. 4. Example realization of a synthesized multipass array. The vertical samples are irregular as a result of the different vertical spacings between the multipass scans and the interferometric receiver arrays. Additional irregularity occurs in the scans because of environmental affects and errors in the navigation system. The large shift in the bottom three scans is real, and is a result of a navigation glitch rather than an error in data-driven localization estimation process.

In addition to the intrinsic sampling irregularity introduced by the interferometric arrays, irregularities are also introduced by nonideal navigation. This is visibly illustrated in Fig. 4, which plots the coordinates of one synthesized multipass aperture localized using the approach outlined in Section III.

It is clear from Fig. 4 that $\Delta\Theta_{\mathrm{scan}}$ varies significantly depending on whether the vehicle maintained the intended altitude, radius, and origin. The goal of the beamforming algorithm described in this section is to generate an estimate of the vertical scattering distribution in the presence of these sampling gaps and irregularities, and avoid contamination from strong sidelobe artifacts for distributions that have a larger vertical extent than D_{scan} but smaller than D_{intf}.

This article has been accepted for inclusion in a future issue of this journal. Content is final as presented, with the exception of pagination.

An additional complexity faced by the beamformer is that target signatures often span many range cells as a result of the wide bandwidth of sonar systems. This can be seen by deriving the range cell migration criterion for a deramped SAS signal. The round trip distance between the aperture point located at (h_{ar}, r_{ar}) and a scatterer located at (h_t, r_t) is

$$d = 2\sqrt{(r_{ar} - r_t)^2 + (h_{ar} - h_t)^2} \tag{43}$$

or

$$d = 2\sqrt{r_g^2 + (h_{ar} - h_t)^2} \tag{44}$$

after making the substitution $r_g = r_{ar} - r_t$. Assuming a vertical array and expanding to second order around $h_{ar} - h_t$

$$d \approx 2r_g + \frac{(h_{ar} - h_t)^2}{r_g} = 2r_g + \frac{h_t^2}{r_g} - \frac{2h_t}{r_g}h_{ar} + \frac{1}{r_g}h_{ar}^2. \tag{45}$$

The process of deramping the signal around $h_t = 0$, in the present case accomplished by backprojecting the data from each vertical aperture point to the $h_t = 0$ plane, removes the quadratic component of (45) leaving behind the linear and offset terms [9]

$$d_{dr} = 2\sqrt{r_g^2 + (h_{ar} - h_t)^2} - 2\sqrt{r_g^2 + h_{ar}^2} \tag{46}$$

$$d_{dr} \approx \frac{h_t^2}{r_g} - \frac{2h_t}{r_g}h_{ar} \tag{47}$$

where d_{dr} represents the scatterer delay structure after deramping. Via the slope term in (47) and the relationship between range resolution, bandwidth, and propagation speed, the deramped range cell migration criterion can be explicitly expressed

$$2\frac{\mathrm{MAX}\,[h_{ar}] - \mathrm{MIN}\,[h_{ar}]}{r_g}h_t < \frac{c}{2f_{BW}} \tag{48}$$

or

$$\frac{f_{BW}}{c}h_t < \frac{r_g}{4\,(\mathrm{MAX}\,[h_{ar}] - \mathrm{MIN}\,[h_{ar}])}. \tag{49}$$

The value f_0 does not appear in (48) or (49), implying that fractional bandwidth is not the critical factor discriminating between sonar and radar systems from a range cell migration standpoint. Rather, from a bandwidth standpoint, the critical factor is the ratio of the bandwidth to the propagation speed f_{BW}/c, namely the reciprocal of the compressed pulse length. For a SAR system such as TerraSAR-X, which generated the data used in [11], this ratio is less than one. In contrast, a 30-kHz bandwidth SAS system would have a ratio of approximately 20, a value over an order of magnitude higher. Repeat pass tomographic beamforming algorithms have mostly been developed within a 1-D spectral analysis framework that assumes the criterion in (49) has been satisfied but this is not often the case for sonar systems. As an example, for a bandwidth of $f_{BW} = 50$ kHz, a range of 30 m, a vertical aperture spanning 2.4 m, sound speed $c = 1500$ m/s, and a modest scattering profile of $h_t = 0.4$ m the left-hand side of (49) equals $f_{BW}h_t/c \approx 13$, and the right-hand side equals $r_g/(4(\mathrm{MAX}[h_{ar}] - \mathrm{MIN}[h_{ar}])) \approx 3$. In this case, the range migration criterion is not met by a factor greater than four. To visually illustrate the effects of range cell migration, a simulation of an array spanning $h_{ar} = 4.5$–6.9 m ($\Delta h_{ar} = 0.05$ cm, regularly spaced) is performed for the previously listed SAS parameters and $f_0 = 175$ kHz. The sediment is simulated using an ensemble of scatterers distributed around an undulating height map, and a target is simulated as discrete points arranged to resemble the scattering from the top and glints on the leading edge of an oil barrel. The deramped time series is shown in Fig. 5, and the presence of the bright diagonal lines crossing multiple range cells indicates that the range cell migration criterion is clearly not met.

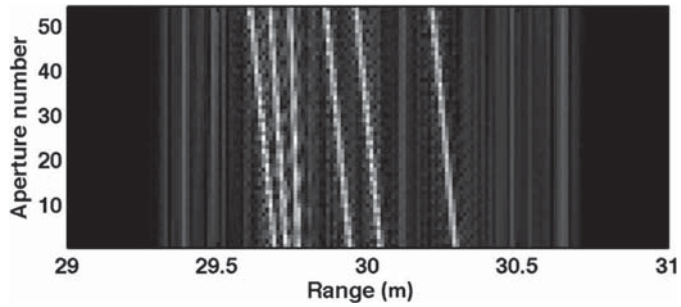

Fig. 5. The backscattered echoes from the scattering distribution shown in X, following the backprojection (deramping) stage. Echoes originating from altitudes near the height of the backprojection plane constitute the vertical lines. The diagonal lines are backscattered echoes from scatterers at significant altitudes, corresponding corners of the barrel.

In addition to crossing multiple range cells, the diagonal echoes shown in Fig. 5 are biased from the true ground range location of the scatterers. This problem, referred to in this paper as range bias, causes geometric distortion in the beamformed image if left uncorrected.

In the present case, range cell migration and sampling irregularity are overcome by subbanding the data to meet the range cell migration criterion and exploiting the similarity of the vertical scattering profile between bands in a compressive sensing framework to reduce beamforming ambiguities. The level of subbanding required to meet the migration criterion is determined by (49) and the vertical distribution size D_{vert}

$$f_{\mathrm{SUB}} = \frac{r_g c}{(\mathrm{MAX}\,[h_{ar}] - \mathrm{MIN}\,[h_{ar}])\,D_{\mathrm{vert}}}. \tag{50}$$

D_{vert} can be determined by D_{intf}, the maximum vertical distribution support of the system, or it can arbitrarily selected as D_{targ} with the stipulation $D_{\mathrm{targ}} \leq D_{\mathrm{intf}}$. In this case, D_{targ} may be determined using interferometry or *a priori* knowledge about the dimensions of the target. The temporally Fourier transformed, deramped data are divided into M partially overlapping subbands of width f_{SUB}. To beamform the irregularly sampled narrowband signals a set of M sensing matrices relating the phase of the received signals to scatterer height is assembled, as in (51), shown at the bottom of the next page.

This article has been accepted for inclusion in a future issue of this journal. Content is final as presented, with the exception of pagination.

In (51), j is the imaginary unit, k_m denotes acoustic wave number $2\pi f_m/c$, and f_m is the center frequency of the mth subband, $m = 1, 2, \ldots, M$. $A^{(m)}$ is the mth matrix of an M-length set of matrices each having size $U \times V$, where U is the number of vertical array samples (e.g., $U = 2N$ in the current example, where N is the number of scans and each scan has two vertically spaced receive arrays) and V is the length of the vertical complex scattering amplitude solution vector. The function Ψ is the deramped delay shown in (46) with the range biasing term (the average delay to the array as a function of h_t), subtracted

$$\begin{aligned}\Psi&\left(h_{ar}^{(u)}, h_t^{(v)}, r_g\right)\\ &= d_{dr}\left(h_{ar}^{(u)}, h_t^{(v)}, r_g\right)\\ &\quad - 2\left(\sqrt{{r_g}^2 + \left(\tilde{h}_{ar} - h_t\right)^2} - \sqrt{{r_g}^2 + \tilde{h}_{ar}^2}\right).\end{aligned} \tag{52}$$

In (52), $\tilde{h}_{ar}$ is the average height of the synthetic array at θ. In both the experiments and simulations $r_g \gg \tilde{h}_{ar}$ and the entries of $A^{(m)}$ change insignificantly over the ranges for which beamforming is applied (versus in the θ-dimension, in which both h_{ar} and the entries of $A^{(m)}$ may change significantly due to platform motion). To save computation time, the set of matrices, during implementation $A^{(m)}$, is only calculated for a single value r_g, equal to the ground range of the sonar platform to the center of the image patch. This set of sensing matrices is used to vertically beamform the data in all range cells of the subbanded data sets.

The subtraction of the second term in (52) prevents the beamforming algorithm from performing an approximate range-bias correction that is discontinuous in frequency, which can result in sidelobe artifacts in the range dimension. In the current algorithm, range bias is corrected after the vertical beamforming operation, and the method for doing this is discussed in a later portion of this section. For a given range cell, the mth subband vertical complex scattering coefficients $\alpha^{(v,m)}$ can be related to the mth column of subbanded, deramped data $S^{(u,m)}$ via

$$A^{(m)}\begin{bmatrix}\alpha^{(1,m)}\\ \alpha^{(2,m)}\\ \vdots\\ \alpha^{(V,m)}\end{bmatrix} = \begin{bmatrix}S^{(1,m)}\\ S^{(2,m)}\\ \vdots\\ S^{(U,m)}\end{bmatrix}. \tag{53}$$

Compressive sensing literature presents a variety of methods to estimate the solution vector $\alpha^{(m,v=1,2,\ldots,V)}$ for the currently relevant case in which $V \gg U$ and the solution vector is sparse. (For a more detailed look at the requirements for application of compressive sensing to synthetic aperture tomography problems, see [18].) In this paper, an approach based on the regularized FOCUSS algorithm [32] is taken. More specifically, the joint sparse extension is exploited because of the assumed common sparsity structure that the M solution vectors $\alpha^{(m,v=1,2,\ldots,V)}$ will have regardless of the frequency subband. The regularized joint sparse M-FOCUSS algorithm, described in [33], calculates a series of solution vectors with common sparsity profile by iterating

$$c_k^{(v)} = \left(\sum_{m=1}^{M}\left(\alpha_k^{(v,m)}\right)^2\right)^{1/2} \tag{54}$$

$$W_{k+1} = \operatorname{diag}\left(\left(c_k^{(1\ldots V)}\right)^{1-\frac{p}{2}}\right) \tag{55}$$

$$\tilde{A}_{k+1} = \tilde{A}_k W_{k+1} \tag{56}$$

$$\begin{aligned}\alpha_k^{(1\ldots V,1\ldots M)} &= W_{k+1}\tilde{A}_{k+1}^T\left(\tilde{A}_{k+1}\tilde{A}_{k+1}^T + \gamma I\right)^{-1}\\ &\quad\cdot S^{(1\ldots U,1\ldots M)}\end{aligned} \tag{57}$$

where k is the current iteration, $\tilde{A}$ is a hypothetical sensing matrix that relates each measurement column to each solution column, I is the identity matrix, γ is a regularization parameter (determined empirically in the present case), and $0 < p \leq 1$ is the chosen norm-like "diversity measure" for which the solution is minimized. For $k = 1$, W is initialized as the identity matrix I. Intuitively, at each iteration the algorithm determines a set of weights for the rows of the sensing matrix using the chosen diversity parameter p applied to the 2-norm $c_k^{(v)}$ of the rows of the previous iteration's $V \times M$ solution matrix. A new solution is calculated using the sensing matrix with the updated weights. Though M-FOCUSS was developed for the multiple measurement vector (MMV) problem in which a single sensing matrix $\tilde{A}$ relates the measurement vectors to the solution vectors, from (54)–(57) it can be seen that the weights are strictly a function of the solution vectors $\alpha_k^{(1\ldots V,1\ldots M)}$ and the assumption of a single sensing matrix is not necessary for the algorithm to operate as long as the joint sparsity assumption holds. In the present case, we assume the sparsity structure is independent of frequency, however from (51), we have M sensing matrices relating the columns of the measurement matrix to the solution matrix. Therefore, in the present case, (56) and (57) are calculated via a *for*-loop that solves $\alpha_{k+1}^{(1\ldots V,m)}$ for each $A_{k+1}^{(m)}$

$$\begin{aligned}&\text{for } m = 1 : M\\ &A_{k+1}^{(m)} = A_k^{(m)} W_{k+1}\\ &\alpha_{k+1}^{(1\ldots V,m)} = W_{k+1} {A_{k+1}^{(m)}}^T\left(A_{k+1}^{(m)} {A_{k+1}^{(m)}}^T + \gamma I\right)^{-1} S^{(1\ldots U,m)}\\ &\text{end.}\end{aligned} \tag{58}$$

$$A^{(m)} = \begin{bmatrix} e^{-jk_m\psi(h_{ar}^{(1)},h_t^{(1)},r_g)} & e^{-jk_m\psi(h_{ar}^{(1)},h_t^{(2)},r_g)} & \cdots & e^{-jk_m\psi(h_{ar}^{(1)},h_t^{(V)},r_g)}\\ e^{-jk_m\psi(h_{ar}^{(2)},h_t^{(1)},r_g)} & e^{-jk_m\psi(h_{ar}^{(2)},h_t^{(2)},r_g)} & & \\ \vdots & & \ddots & \\ e^{-jk_m\psi(h_{ar}^{(U)},h_t^{(1)},r_g)} & & & e^{-jk_m\psi(h_{ar}^{(U)},h_t^{(V)},r_g)}\end{bmatrix}. \tag{51}$$

This article has been accepted for inclusion in a future issue of this journal. Content is final as presented, with the exception of pagination.

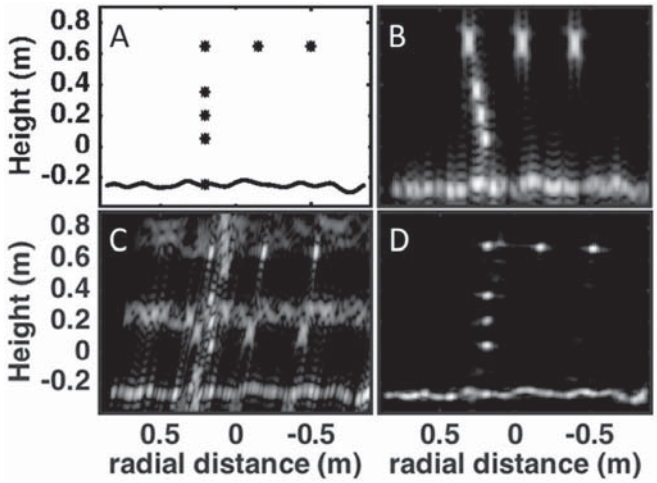

Fig. 6. (a) The simulated scattering distribution and the results for different beamforming approaches. (b) The result of 1-D Fourier analysis applied to the ideal, regularly sampled array. (c) The result of backprojection applied to the irregularly sampled experimental array shape. (d) The wideband sparse result generated using the procedure described in this paper. The color scale is logarithmic and the dynamic range on all SAS images is 30 dB referenced to the brightest point.

The most time-consuming portion of this algorithm is finding the solution of (57), and the obvious downside to this approach is that via the modification in (58) this step must now be repeated M times rather than once. On the positive side $A_k^{(m)}$ remains relatively small in size (i.e., $U \times V$).

Following estimation of the vertical scattering profiles for each range cell of the subbanded data sets a Fourier transform in the range dimension is computed for each subband and a full spectrum representation of the scattering response for the patch is attained by recombining the subbands

$$\tilde{\alpha}\left(h_t, k\right) = \Big[\mathcal{F}_r\left\{\alpha^{(1)}\left(h_t, r\right)\right\}, \times \mathcal{F}_r\left\{\alpha^{(2)}\left(h_t, r\right)\right\}, \ldots, \mathcal{F}_r\left\{\alpha^{(M)}\left(h_t, r\right)\right\}\Big]. \tag{59}$$

Range bias is corrected by reapplying as a height-dependent linear phase the h_t-dependent delays previously subtracted from Ψ. Incorporating this correction, the beamformed scattering profile can be recovered by performing an inverse Fourier transform in range

$$\hat{\alpha}\left(h_t, r\right) = \mathcal{F}_k^{-1} \times \left\{\tilde{\alpha}\left(h_t, k\right) e^{j2k\left(\sqrt{{r_g}^2+\left(\tilde{h}_{ar}-h_t\right)^2}-\sqrt{{r_g}^2+\tilde{h}_{ar}^2}\right)}\right\}. \tag{60}$$

The matrix $\hat{\alpha}(h_t, r)$ now represents the beamformed scattering profile, free of range bias. To demonstrate the algorithm it is applied to the simulated sediment and target distribution depicted in Fig. 6(a). This is the same scattering configuration used to generate the simulated data shown in Fig. 5. Rather than using the regular sampling scheme illustrating range cell migration in Fig. 5, the altitude scan pattern described in Section II with a 10-cm physical receiver array baseline is utilized, similar to the actual experimental configuration. Using a diversity factor of $p = 0.8$, $f_{\mathrm{SUB}} \approx 5$ kHz, $\gamma = 0.01$, 50% overlap between subbands and a hardwired limit of five M-FOCUSS iterations the sparse image in Fig. 6(d) was obtained. For comparison purposes the result of applying 1-D Fourier analysis to the regular, gridded data of Fig. 5 is shown in Fig. 6(b) (note that the effects of irregular array sampling will not be present in this example), and the result of generalized backprojection applied to the irregular array is shown in Fig. 6(c).

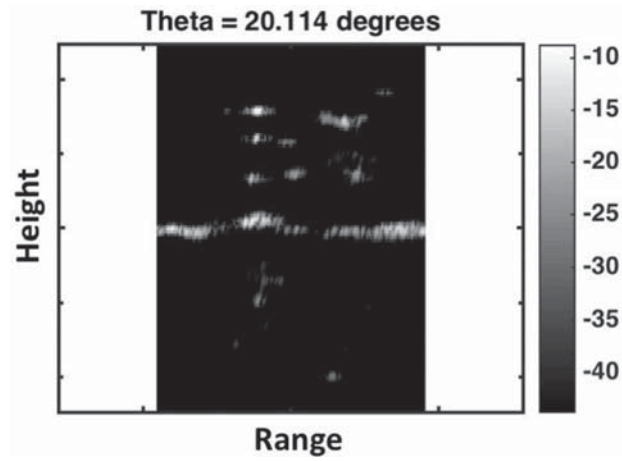

Fig. 7. The scattering profile at one aspect angle of a vertically oriented steel oil barrel, showing the barrel rings and scattering from the sediment surface. The color scale is in decibels referenced to the brightest point.

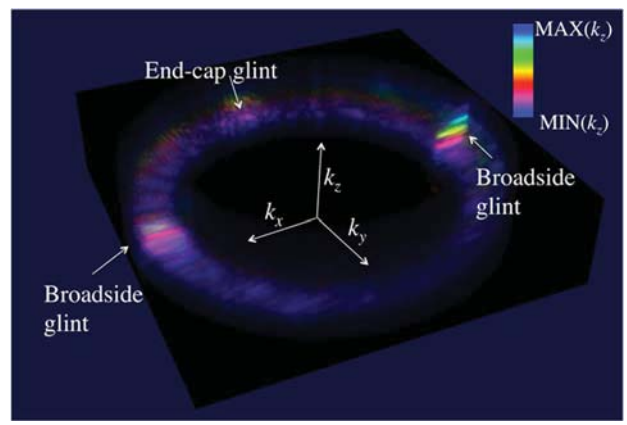

Fig. 8. A maximum intensity projection (MIP) image of the beamformed data in 3-D wave number space. The spectral magnitudes have been color-coded based on the k_z value to make the 3-D structure more visible. The broadside edge glints and the end-cap glint are visible in the spectrum.

In Fig. 6(b), the range bias in the 1-D Fourier beamforming example is highly visible and manifests as a strong slant in the leading edge of the barrel. A reduction in resolution resulting from range cell migration can also be seen. Generalized backprojection corrects range bias and maintains a higher resolution, as can be seen in Fig. 6(c), but it suffers from high grating lobe levels due to undersampling. In contrast, the sparse processing result shown in Fig. 6(d) maintains both high resolution and low grating lobe levels. Fig. 7 shows the results of the algorithm applied to real data corresponding to the multipass insonification of a vertically oriented barrel. In this case, the radial scan pattern is used, however only six scans were successful,

This article has been accepted for inclusion in a future issue of this journal. Content is final as presented, with the exception of pagination.

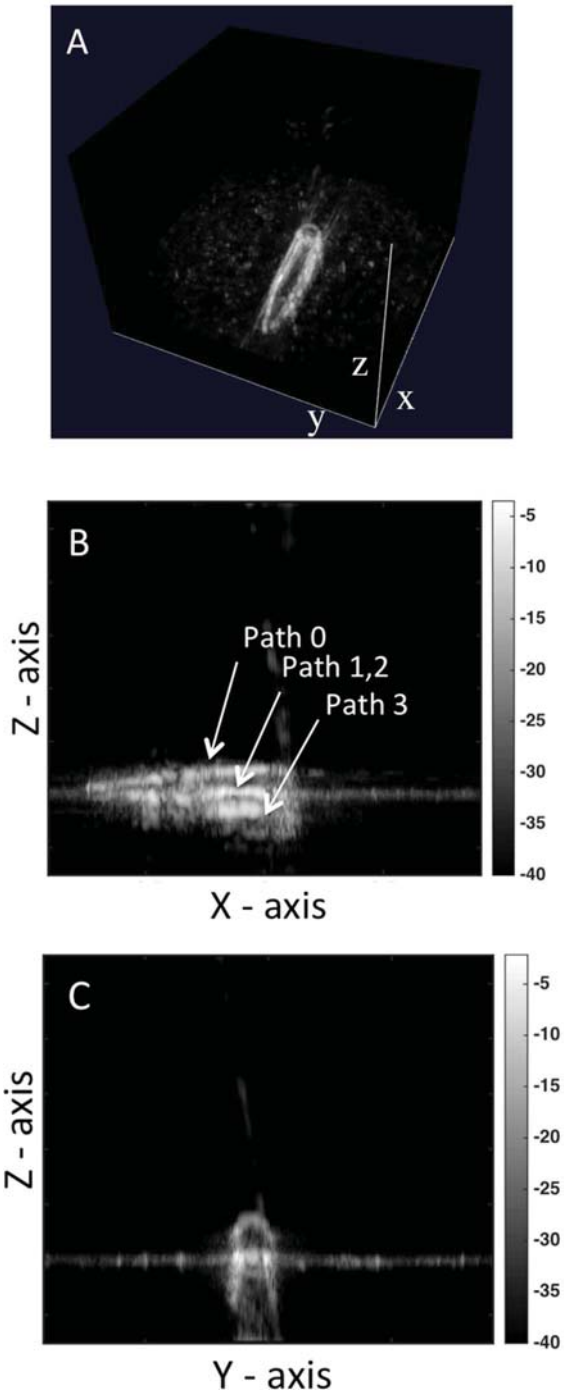

Fig. 9. Three depictions of the beamformed data in the spatial domain. (a) An MIP image of the 3-D data. (b) A cutaway of the side, making the specular glint and the multipath interactions with the sediment visible. (c) A cutaway of the end of the target, showing the end cap and the acoustic reflection of the end cap under the sediment. The intensity scale on each image is logarithmic, spanning 40 dB with reference to the brightest point.

resulting in $U = 2N = 12$. Utilizing the proposed technique, the scattering profile shown in Fig. 7 was constructed.

This compressive sensing approach is used to perform the vertical, multipass beamforming in all subsequent experimental data sets. It performed consistently well in conjunction with the localization techniques described in Section III (see, e.g., the beamforming results shown in Figs. 9–12). A tendency has been noted, however, for compressive sensing algorithms to be highly sensitive to model error [34]. In the present case, navigation and medium propagation model errors manifest as incorrect entry values in the sensing matrices defined by (51). A typical navigation accuracy constraint listed in SAS literature is $\lambda/8$ [1], however one SAR study showed complete image reconstruction failure when direct compressive-sensing-based approaches were applied to data having a positional error variance of $\lambda/8$ [35]. The same paper and others (see, e.g., [36] and [37]) have proposed potentially applicable methods for compressive sensing in the presence of model errors.

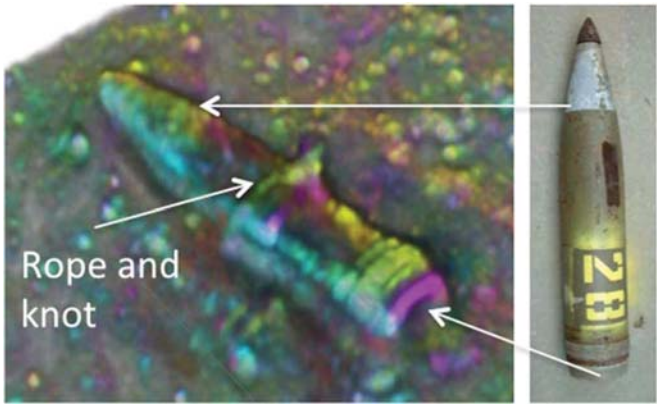

Fig. 10. Volumetric rendering of the beamformed data, mapping voxel color to insonification angle. The rope around the central portion of the target is clearly visible, as are the ring-like structures composing the end cap and the material boundaries near the nose of the target. A picture of the target before deployment (without the rope) is shown on the right-hand side.

Following vertical beamforming the process described in (4)–(7) is used to beamform each height plane, forming a volumetric image. The vertical and horizontal beamforming operations are done in a different order in the present case versus the standard approach in SAR literature, which is to beamform in the vertical dimension using a series of prebeamformed image stacks. The primary reason for the alternate order of operation is that image stacks require integration of the scattered data over a span of aperture points in θ. Due to currents, wave action, and platform instabilities, the sonar can move rapidly as a function of θ. The data often contain scattering signatures from highly anisotropic targets, and in the case of beamformed subapertures it is unclear how to optimally define the beamforming parameters in (51), which must represent entire subapertures irrespective of the directivity of the insonified scatterers.

V. Experimental Results

A series of targets were scanned using the radial and altitude patterns described in Section II. Aperture localization was completed without the aid of GPS or introduced calibration scatterers. Section V-A will focus on interpreting the results from the proud 155-mm Howitzer shell. Section V-B will discuss the results for the remaining targets. All 3-D volumetric images were visualized using the Vaa3D volumetric data visualization tool [38], [39] and [40].

This article has been accepted for inclusion in a future issue of this journal. Content is final as presented, with the exception of pagination.

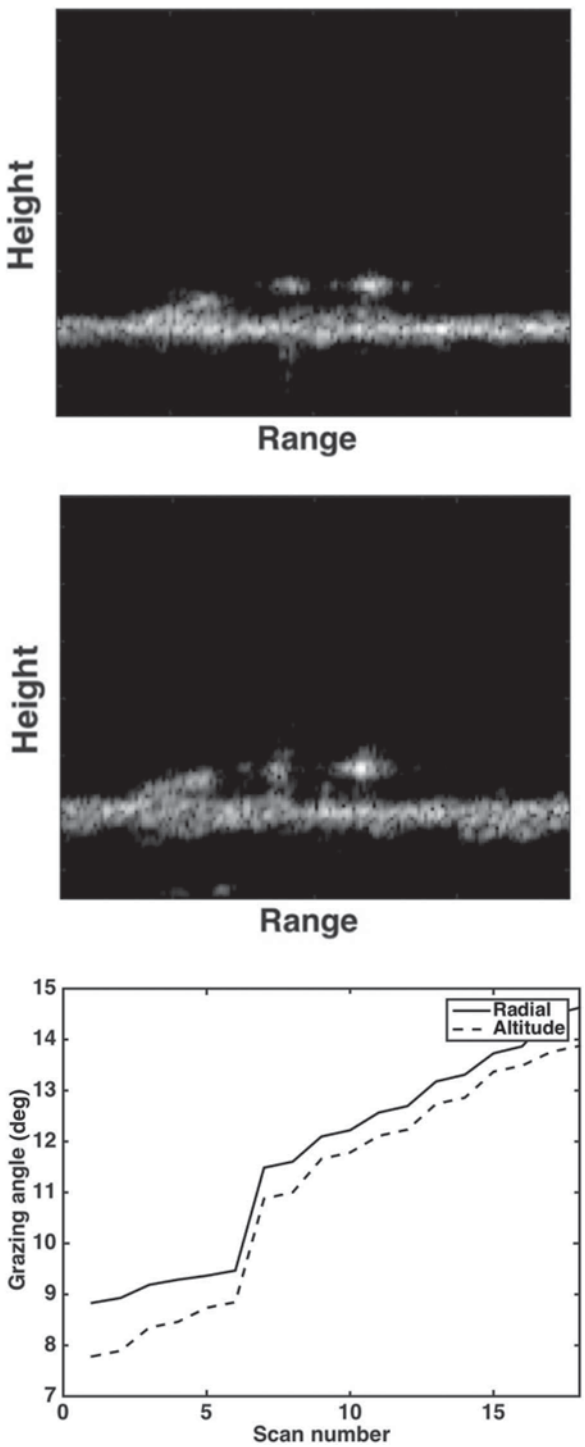

Fig. 11. The vertical scattering profile for the end-on backscattering response of the proud 155-mm Howitzer shell, imaged using both the radial (top) and altitude varying (middle) scan patterns described in Section I, along with the grazing angles of both scans (bottom). The intensity scale on both SAS images is logarithmic, with a dynamic range of 50 dB referenced to the brightest point.

A. Proud Howitzer Shell Results

The wave number domain data for the beamformed proud Howitzer data resembles an annulus and is shown in Fig. 8.

The broadside and end-on scattering mechanisms are clearly visible in the spectrum. An inverse 3-D Fourier transform can be applied to the wave number domain data to recover a complex volumetric 3-D image, the magnitudes of which are shown in Fig. 9.

TABLE I
A LIST OF THE SCANNED TARGETS AND THE NUMBER OF SCANS COMPLETED FOR THE RADIAL AND ALTITUDE TYPES. THE AUV MALFUNCTIONED AFTER SIX SCANS AROUND THE STEEL BARREL, AND NO ALTITUDE SCANS EXIST FOR EITHER THE STEEL BARREL OR THE PROUD, SOLID 2-1 ALUMINUM CYLINDER

Target	Radial scans	Altitude scans
Proud Howitzer	9	9
Oblique Howitzer	9	9
Steel Barrel	6	0
2-1 cylinder	8	0

Scattering mechanisms consistent with the specular glint and the reciprocal target-bottom and bottom-target multipaths are visible, with a double bottom bounce faintly visible as well (paths 0, 1, 2, and 3 in the notation of [41]). In Fig. 9(c), an inverted copy of the howitzer end cap is visible under the interface.

To improve interpretability of the 3-D images, in Fig. 10, the magnitudes of the raw data have been compressed before beamforming and angular subaperture images are incoherently combined [23]. These subaperture images are color coded based on the direction of insonification: subapertures ranging from 1° to 120° are mapped to the red channel, 121° to 240° are mapped to green, and 241° to 360° are mapped to blue.

In Fig. 10, features in the image clearly map to material boundaries and target structures, such as the tip and end cap. Furthermore, the nylon rope tied around the target, absent while acquiring the photo, is clearly visible in the sonar image.

Fig. 11 shows the vertically beamformed data and aperture grazing angles for the nose-on target aspect, using both the altitude and the radial scan patterns.

Both apertures are sampled highly irregularly and a large grazing angle gap occurs at about 10° in both cases as a result of a navigation glitch. This glitch was present in most of the scans and is probably indicative of a systematic error in the navigation system or vehicle objective at the time of the experiments. The average grazing angle of the radial scan pattern is approximately half a degree higher than the altitude scan pattern, but the span of grazing angles is approximately equal, with the altitude scan being slightly greater (5.6° versus 6.1°). Qualitatively, the altitude scan appears to maintain slightly higher focus. A quantifiable estimate of relative image quality can be found via the average of the Shannon entropy of the image [42], calculated columnwise by

$$H = -\sum_v Y^{(v)} \ln Y^{(v)} \tag{61}$$

where

$$Y^{(v)} = \frac{\left|\alpha^{(v)}\right|^2}{\sum_v \left|\alpha^{(v)}\right|^2}. \tag{62}$$

In (61) and (62), Y is the normalized intensity of the complex vertical scattering profile of a single column of α, v is the pixel index in the vertical dimension, and H is the entropy calculated for the column. Using this metric, the average columnar entropy

This article has been accepted for inclusion in a future issue of this journal. Content is final as presented, with the exception of pagination.

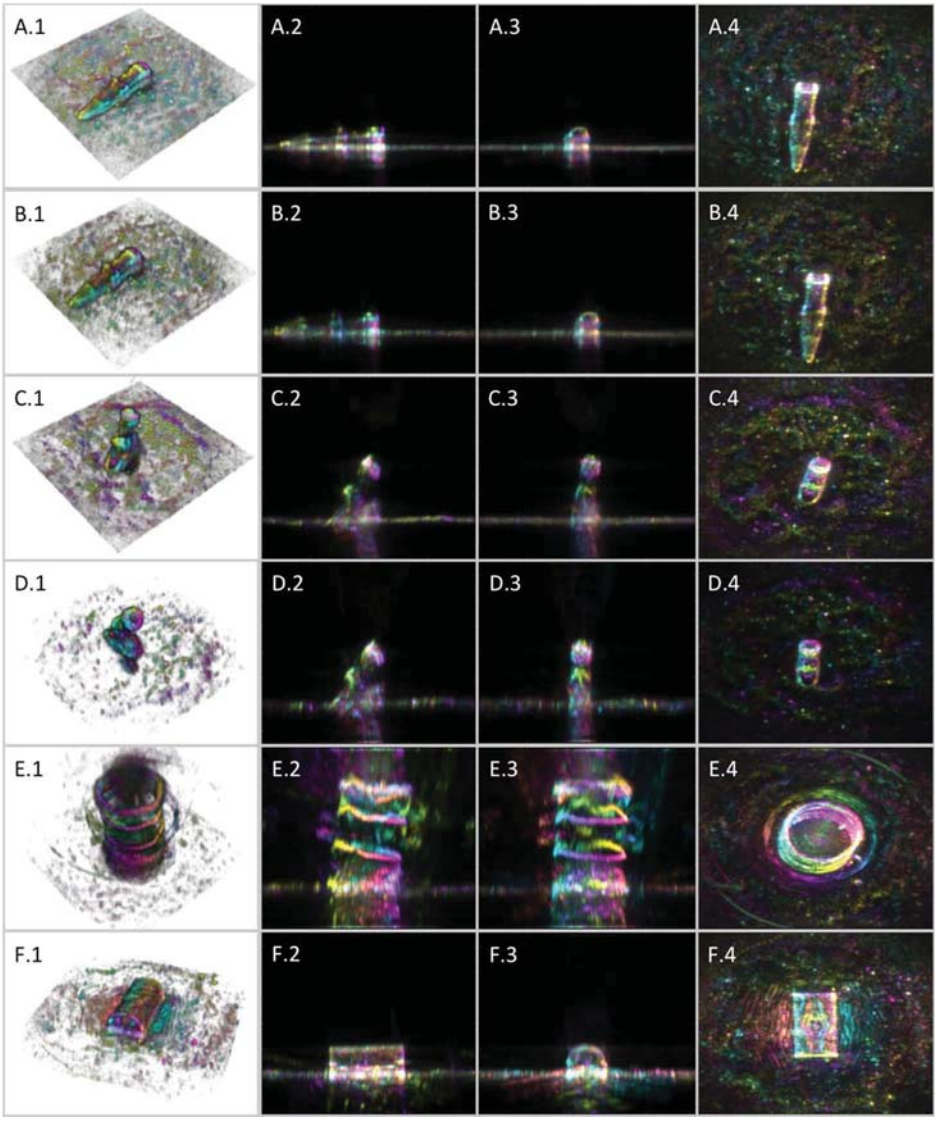

Fig. 12. Rendered images and projections of the volumetric data corresponding to the scans described in Table I. Column 1) shows the linear scale three-quarter view volumetric images rendered using alpha blending; column 2) shows projections of the volumetric images onto the XZ-plane; column 3) shows projections onto the YZ-plane; and column 4) shows projections onto the XY-plane. From top to bottom, the rows show: (A) proud Howitzer, altitude scan; (B) proud Howitzer, radial scan; (C) oblique Howitzer, altitude scan; (D) oblique Howitzer, radial scan; (E) proud vertical steel barrel, radial scan; and (F) proud 2-1 solid aluminum cylinder, radial scan.

measure for the altitude scan is 1.49 and for the radial scan 1.8, where lower values indicate lower entropy and higher focus. Despite the altitude scan having slightly higher focus at this aspect angle, the similarity of the results indicates that the radial scan pattern is also a viable approach for generating volumetric scattering data characterizing targets.

B. Additional Target Results

The scan configurations for all of the targets are listed in Table I, which contains the targets, the utilized scan patterns, and number of completed scans for each pattern. Radial and altitude scans were attempted for each target, however due to time constraints and a GPS coordinate locking error, altitude scans were achieved for only two targets.

For each data set, a three-quarter view alpha-blended volumetric image is displayed in Fig. 12, as well as the projection of the volumetric intensity data in the X-, Y-, and Z-dimensions. Several observations can be made from Fig. 12. The different scan methods used to generate the howitzer images shown in rows A and B result in almost identical volumetric images, indicating that both methods are equally valid for multipass processing. The vertical resolution and general quality of the altitude scan for the oblique cylinder was much better than that of the corresponding radial scan, however. Both oblique UXO scans show prominent acoustic scattering between the UXO and the sediment, probably indicative of multiple scattering. From the results in row E, it can be seen that the barrel is not perfectly vertical in orientation, and in row F, it can be observed that the cylinder is not actually proud on the sediment. In fact, in the time period between deployment and when it was scanned it appears to have become almost half buried.

While there are some obvious visual similarities between ordinary single-pass CSAS images and the XY-plane projected images in the right column of Fig. 12, some crucial differences

This article has been accepted for inclusion in a future issue of this journal. Content is final as presented, with the exception of pagination.

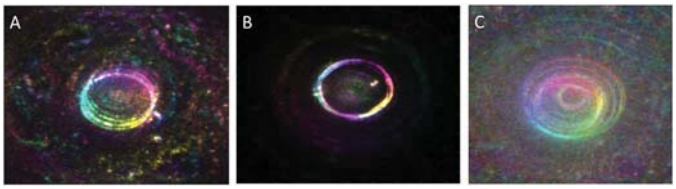

Fig. 13. Slices of the 3-D, tomographically beamformed data cube for the steel barrel corresponding to the bottom (a) and top (b) of the barrel. Shown for comparison is the circular SAS image of the same object (c), generated using only the reference scan.

exist. In single-pass scans, the image must be beamformed to a surface to preserve focus. This is an inherent requirement for nonlinear scan geometries and the circular scan geometry is an extreme case. Objects having some offset from the imaging plane in the Z-(height)-dimension exhibit geometric distortion. In contrast, focus is preserved in the height dimension in the case of the volumetric images, and the projection of the data cube onto the XY-plane preserves the geometry of the features irrespective of the displacement in the Z-dimension. The result is that certain target features are easily visible in the tomographic projection, but are difficult to identify in the single-pass scan. The ability to examine the scattering cross section of an object at a given height plane also reduces the feature masking affects of range layover. Fig. 13 shows examples of this, in which the single-pass CSAS image of the barrel is compared to slices through the data cube made at both the ground plane and the top of the barrel.

Two features of the target that are difficult to discern in the single-pass scan, the flange on the top and an object next to the base, are visible in the target slices at the corresponding scatterer altitudes. These figures demonstrate the ability to resolve features that are either distorted from being out of plane, or hidden by stronger backscattering features as a result of range layover.

VI. Conclusion

Three-dimensional synthetic aperture tomography has been demonstrated using an AUV-based SAS in a multipass circular synthetic aperture framework. Several challenges existed to coherently process the multipass data, including the lack of any external navigation aids, vertically beamforming with an irregular and undersampled synthetic array, sensitivity to medium propagation speed errors, and the migration of the vertical scattering signatures of objects through multiple range cells. Techniques for addressing each of these challenges were presented, and the successful results of the tomographic processing for many targets were shown.

In related SAR and SAS literature, a primary justification for performing tomography is to overcome range layover. The authors suggest that SAS tomography has many more uses than simply overcoming range layover. For example, SAS tomography could be a useful tool for studying physical scattering mechanisms such as target–sediment interactions, elastic scattering mechanisms at low frequencies, volumetric scattering from different types of sediments, or studying how internal target features affect scattering signatures and manifest in 2-D image projections.

Future work may include investigating alternative beamforming approaches, conducting experiments over a larger span of grazing angles, or using more efficient corkscrew or spiral patterns rather than individual circles. Alternatively, rather than merely improving the robustness and efficiency of the data processing, SAS tomography may be applied in actual sediment and environment studies or target characterization or recognition studies.

Appendix

An elevation sampling criterion commonly found in tomographic SAR literature is [6]

$$d \leq \frac{\lambda r_0}{2H} \tag{A.1}$$

where λ is wavelength, d is the height between multipass scans, r_0 is the range to a scatterer distribution, and H is the maximum vertical distance, or height, between scatterers in the distribution. Equation (A.1) is demonstrated to be an approximation to (40). Multiplying both sides of (40) by grazing angle $\Delta\Theta$ and the reciprocal of the scatterer distribution diameter D results in

$$\Delta\Theta < \frac{\lambda}{2D}. \tag{A.2}$$

Multiplying both sides by r_0

$$\Delta\Theta r_0 < \frac{\lambda r_0}{2D}. \tag{A.3}$$

For low grazing angles $D = H$ and for small $\Delta\Theta$, $\Delta\Theta r_0 = d$. Therefore

$$d < \frac{\lambda r_0}{2H}. \tag{A.4}$$

The standard SAR sampling criterion can therefore be interpreted as a small angle approximation of the general tomographic sampling requirement for cases in which the grazing angle is low.

Acknowledgment

The authors would like to thank the NSWC PCD SAS and NSWC PCD Dive Locker for their respective roles in the data collection process.

References

[1] D. W. Hawkins, "Synthetic aperture imaging algorithms: With application to wideband sonar," Ph.D. dissertation, Electr. Electron. Eng. Dept., Univ. Canterbury, Christchurch, New Zealand, 1996.

[2] R. E. Hansen, "Introduction to synthetic aperture sonar," *Sonar Systems*, N. Z. Kolev, Ed. Triangle Park, NC, USA: Intech, Sep. 2011, pp. 3–7.

[3] R. E. Hansen, H. J. Callow, T. O. Sæbø, and S. A. V. Synnes, "Challenges in seafloor imaging and mapping with synthetic aperture sonar," *IEEE Trans. Geosci. Remote Sens.*, vol. 49, no. 10, pp. 3677–3687, Oct. 2011.

[4] H. D. Griffiths, *et al.*, "Interferometric synthetic aperture sonar for high-resolution 3D mapping of the seabed," in *Proc. Inst. Electr. Eng.—Radar Sonar Navig.*, vol. 144, no. 2, Apr. 1997, pp. 96–103.

[5] P. N. Denbigh, "Signal processing strategies for a bathymetric sidescan sonar," *IEEE J. Ocean. Eng.*, vol. 19, no. 3, pp. 382–390, Jul. 1994.

[6] E. Rodriguez and J. M. Martin, "Theory and design of interferometric synthetic aperture radars," in *Proc. Inst. Electr. Eng. F—Radar Signal Process.*, vol. 139, no. 2, Apr. 1992, pp. 147–159.

[7] T. O. Sæbø, R. E. Hansen, and A. Austeng, "Synthetic aperture sonar tomography: A preliminary study," in *Proc. 10th Eur. Conf. Synthetic Aperture Radar*, Berlin, Germany, Jun. 2014.

This article has been accepted for inclusion in a future issue of this journal. Content is final as presented, with the exception of pagination.

[8] J. Jideani and W. Wilkinson, "Air-based synthetic aperture sonar tomography using compressive sensing," in *Proc. IEEE Int. Ultrason. Symp.*, 2014, DOI: 10.1109/ULTSYM.2014.0013.

[9] A. Reigber and A. Moreira, "First demonstration of airborne SAR tomography using multibaseline L-band data," *IEEE Trans. Geosci. Remote Sens.*, vol. 38, no. 5, pp. 2142–2152, Sep. 2000.

[10] D. Ho Tong Minh, *et al.*, "Relating P-band synthetic aperture radar tomography to tropical forest biomass," *IEEE Trans. Geosci. Remote Sens.*, vol. 52, no. 2, pp. 967–979, Feb. 2014.

[11] X. Zhu and R. Bamler, "Very high resolution spaceborne SAR tomography in urban environment," *IEEE Trans. Geosci. Remote Sens.*, vol. 48, no. 12, pp. 4296–4308, Dec. 2010.

[12] O. Frey, F. Morsdorf, and E. Meier, "Tomographic processing of multibaseline P-band SAR data for imaging of a forested area," in *Proc. Int. Geosci. Remote Sens. Symp.*, Jul. 2007, pp. 156–159.

[13] O. Ponce, *et al.*, "Fully polarimetric high-resolution 3-D imaging with circular SAR at L-band," *IEEE Trans. Geosci. Remote Sens.*, vol. 52, no. 6, pp. 3074–3090, Jun. 2014.

[14] C. H. Casteel, L. A. Gorham, M. J. Minardi, S. Scarborough, and K. D. Naidu, "A challenge problem for 2D/3D imaging of targets from a volumetric data set in an urban environment," in *Proc. SPIE—Int. Soc. Opt. Eng.*, vol. 6568, 2007, DOI: 10.1117/12.731457.

[15] S. K. Mitchell, K. N. Scarbrough, S. P. Pitt, and T. L. Kooij, "High resolution circular SAS with controlled focus," in *Proc. SAS/SAR*, Lerici, Italy, Sep. 2006, pp. 65–71.

[16] B. G. Ferguson, K. W. Lo, and R. J. Wyber, "Advances in high-frequency active sonars for countering asymmetric threats in littoral waters," in *Proc. IEEE OCEANS Conf.*, Boston, MA, USA, Sep. 2006 DOI: 10.1109/OCEANS.2006.306801.

[17] C. D. Austin, E. Ertin, and R. L. Moses, "Sparse multipass 3D SAR imaging: Applications to the GOTCHA data set," in *Proc. SPIE—Int. Soc. Opt. Eng.*, vol. 7337, 2009, DOI: 10.1117/12.820323.

[18] X. Zhu and R. Bamler, "Tomographic SAR inversion by L1-normregularization—The compressive sensing approach," *IEEE Trans. Geosci. Remote Sens.*, vol. 48, no. 10, pp. 3839–3846, Oct. 2010.

[19] T. O. Sæbø and R. E. Hansen, "Comparison between interferometric SAS and interferometric SAR," in *Proc. SAS/SAR*, Lerici, Italy, Sep. 2010, pp. 81–86.

[20] R. P. Stokey, *et al.*, "Development of the REMUS 600 autonomous underwater vehicle," in *Proc. IEEE OCEANS Conf.*, Washington, DC, USA, Sep. 2005, DOI: 10.1109/OCEANS.2005.1639934.

[21] B. G. Ferguson and R. J. Wyber, "Application of acoustic reflection tomography to sonar imaging," *J. Acoust Soc. Amer.*, vol. 117, no. 5, pp. 2915–2928, May 2005.

[22] H. J. Callow, R. E. Hansen, S. Synnes, and T. O. Sæbø, "Circular synthetic aperture sonar without a beacon," in *Proc. Underwater Acoustic Measurements (UAM)*, Nafplion, Greece Jun. 2009 [Online]. Available: http://promitheas.iacm.forth.gr/UAM_Proceedings

[23] T. M. Marston, J. L. Kennedy, and P. L. Marston, "Coherent and semi-coherent processing of limited aperture circular synthetic aperture (CSAS) data," in *Proc. IEEE OCEANS Conf.*, Waikoloa, HI, USA, Sep. 2011.

[24] A. Bellettini and M. A. Pinto, "Theoretical accuracy of synthetic aperture sonar micronavigation using a displaced phase-center antenna," *IEEE J. Ocean. Eng.*, vol. 27, no. 4, pp. 780–789, Oct. 2002.

[25] D. A. Cook, "Synthetic aperture sonar motion estimation and compensation," M.S. thesis, Electr. Comput. Eng. Dept., Georgia Inst. Technol., Atlanta, GA, USA, 2007.

[26] H. Cantalloube and C. Nahum, "Multiscale local mapdrift-driven multilateration SAR autofocus using fast polar format image synthesis," *IEEE Trans. Geosci. Remote Sens.*, vol. 49, no. 10, pp. 3730–3736, Oct. 2011.

[27] T. M. Marston and J. L. Kennedy, "Correction of aperture errors in circular SAS imagery via pseudo-stripmap autofocusing," in *Proc. SAS/SAR*, Lerici, Italy, Sep. 2014, pp. 110–117.

[28] T. M. Marston, J. L. Kennedy, and P. L. Marston, "Autofocusing circular synthetic aperture sonar imagery using phase corrections modeled as generalized cones," *J. Acoust. Soc. Amer.*, vol. 136, pp. 614–622, Aug. 2014.

[29] D. S. Plotnick, P. L. Marston, and T. M. Marston, "Fast nearfield to farfield conversion algorithm for circular synthetic aperture sonar," *J. Acoust. Soc. Amer. Exp. Lett.*, vol. 136, Aug. 2014, http://dx.doi.org/10.1121/1.4885486.

[30] T. G-Michael, *et al.*, "Image-based automated change detection for synthetic aperture sonar by multi-stage co-registration and canonical correlation analysis," *IEEE J. Ocean. Eng.*, 2015, DOI: 10.1109/JOE.2015.2465631.

[31] F. Simonetti, L. Huang, and N. Duric, "On the spatial sampling of wave fields with circular ring apertures," *J. Appl. Phys.*, vol. 101, 2007, 083103.

[32] B. D. Rao, K. Engan, S. F. Cotter, J. Palmer, and K. Kreutz-Delgado, "Subset selection in noise based on diversity measure minimization," *IEEE Trans. Signal Process.*, vol. 51, no. 3, pp. 760–770, Mar. 2003.

[33] S. F. Cotter, B. D. Rao, K. Engan, and K. Kreutz-Delgado, "Sparse solutions to linear inverse problems with multiple measurement vectors," *IEEE Trans. Signal Process.*, vol. 53, no. 7, pp. 2477–2488, Jul. 2005.

[34] Y. Chi, L. L. Scharf, A. Pezeshki, and A. R. Calderbank, "Sensitivity to basis mismatch in compressed sensing," *IEEE Trans. Signal Process.*, vol. 59, no. 5, pp. 2182–2195, May 2011.

[35] S. Wei, X. Zhang, and J. Shi, "An autofocus approach for model error correction in compressed sensing SAR imaging," in *Proc. Int. Geosci. Remote Sens. Symp.*, Munich, Germany, Jul. 2012, pp. 3987–3990.

[36] H. Zhu, G. Leus, and G. B. Giannakis, "Sparsity-cognizant total least-squares for perturbed compressive sampling," *IEEE Trans. Signal Process.*, vol. 59, no. 5, pp. 2002–2016, May 2011.

[37] J. Yang, X. Huang, J. Thompson, T. Jin, and Z. Zhou, "Compressed sensing radar imaging with compensation of observation positioning error," *IEEE Trans. Geosci. Remote Sens.*, vol. 52, no. 8, pp. 4608–4620, Aug. 2014.

[38] Peng, *et al.*, "V3D enables real-time 3D visualization and quantitative analysis of large-scale biological image data sets," *Nature Biotechnol.*, vol. 28, no. 4, pp. 348–355, 2010.

[39] Peng, *et al.*, "Extensible visualization and analysis for multidimensional images using Vaa3D," *Nature Protocols*, vol. 9, no. 1, pp. 193–208, 2014.

[40] Peng, *et al.*, "Virtual finger boosts three-dimensional imaging and microsurgery as well as terabyte volume image visualization and analysis," *Nature Commun.*, vol. 5, pp. 4342, 2011.

[41] K. Baik and P. L. Marston, "Kirchhoff approximation for a cylinder breaking through a plane surface and the measured scattering," *IEEE J. Ocean. Eng.*, vol. 33, no. 4, pp. 386–396, Oct. 2008.

[42] J. R. Fienup and J. J. Miller, "Aberration correction by maximizing generalized sharpness metrics," *J. Opt. Soc. Amer. A*, vol. 20, no. 4, pp. 609–620, Apr. 2003.

Timothy M. Marston received the B.S. degree in electrical engineering from Seattle Pacific University, Seattle, WA, USA, in 2004 and the M.S. and Ph.D. degrees in acoustics from Pennsylvania State University, State College, PA, USA, in 2006 and 2009, focusing on infrasonic sound propagation and acoustic transducer calibration.

From 2009 to 2010, he worked at the Physics Department, Washington State University, Pullman, WA, USA, analyzing the acoustic response characteristics of submerged elastic structures near interfaces. From 2010 to 2013, he worked at the Naval Surface Warfare Center, Panama City Division (NSWC-PCD), Panama City Beach, FL, USA, where he received the U.S. Navy Meritorious Civilian Service award in 2013 for contributing significant advancements to mine countermeasure sonar technology and developing robust circular synthetic aperture imaging techniques. He currently works at the Applied Physics Laboratory, University of Washington (APL-UW), Seattle, WA, USA, where his research interests include acoustic signal analysis, remote sensing, and scattering physics.

Dr. Marston is a member of the Acoustical Society of America.

Jermaine L. Kennedy received the B.S. degree in physics and the B.S. degree in physics education from State University of New York at Buffalo, Buffalo, NY, USA, in 1998 and 1999, respectively, and the M.S. and Ph.D. degrees in applied physics from the University of South Florida, Tampa, FL, USA, in 2001 and 2006, respectively.

From 2006 to 2009, he was Vice President and Principal Investigator for a Department of Energy SBIR Phase I and II project at the lasers and fiber optics firm Micromaterials, Inc., Tampa, FL, USA. He is currently a Research Physicist at Naval Surface Warfare Center Panama City Division (NSWC-PCD), Panama City Beach, FL, USA. His research interests include low-to-mid-frequency underwater acoustic scattering for target classification and discrimination, circular synthetic aperture sonar, acoustic image processing, laser & nonlinear optical physics, technology transfer, and applied R&D.

Dr. Kennedy is a member of the Optical Society of America, the American Physical Society, Sigma Pi Sigma, and the Society of Photo-Optical Instrumentation Engineers.

TomoSAS in bathymetrically complex environments

Timothy Marston, APL-UW, marston@apl.washington.edu, USA
Jermaine Kennedy, NSWC-PCD, Jermaine.kennedy@navy.mil, USA

Abstract

In a synthetic aperture radar context, tomography describes the process of resolving the spatial distribution of scatterers in the vertical dimension as well as in the horizontal plane using data stacks collected at varying altitudes or ranges (i.e. "TomoSAR"). The positional accuracy requirements for tomographic processing represent a severe challenge for the analogous field of synthetic aperture sonar (SAS), in which sensors are mounted on autonomous underwater vehicles (AUV's) that can be heavily influenced by currents and rely on dead-reckoning for navigation. Data-driven methods similar to redundant phase center (RPC) micronavigation may be used to accurately resolve the relative locations of the various scans comprising the aperture, however this type of processing is prone to biasing by topographic variation. In this paper, TomoSAS imagery generated using multi-scan data collected from AUV's is compared for the cases in which bathymetry is neglected (i.e. a flat bottom is assumed), or explicitly formulated into the navigation refinement and multi-scan alignment process.

1 Introduction

Tomographic synthetic aperture radar, or TomoSAR, is a technique for resolving range layover and estimating the three dimensional scattering profile of objects in SAR imagery using data from multiple scans. The additional scans provide backscattering information from multiple grazing angles that can be used to create a true, volumetric reconstruction of a structure or scene. TomoSAR is rapidly establishing itself as a useful scientific tool for applications such as estimating biomass density [1] or measuring temporal deformations in permanent structures [2]. TomoSAR has been demonstrated using satellite or airborne systems, however airborne systems are significantly less stable from a navigation standpoint, and the individual scans comprising a multi-scan aperture may contain large perturbations from the ideal path. Precise knowledge of these perturbations is essential when performing aperture synthesis and both GPS technology and the inclusion of isotropic scatterers such as tophat reflectors or Luneburg lenses are typically used during airborne TomoSAR experiments (see, e.g. the experiments described in [3], and [4]).

In the analogous field of synthetic aperture sonar, GPS signals are unavailable due to the attenuating properties of seawater and navigation systems typically rely on dead reckoning. Furthermore, it can be costly to deploy navigation references. The accumulation of navigation errors due to the usage of inertial navigation systems forces SAS systems to rely on data-driven techniques to enhance navigation accuracy.

Investigations into coherent change detection have resulted in a series of SAS papers focused on relative scan localization and repeat pass navigation refinement. In [5], a method for estimating a range and orientation correction between scans is described. In [6] redundant phase center processing is extended to the repeat-pass case, enabling the precision estimation of range and heading corrections. In [7] altitude, range, and surge navigation refinements are estimated from coherently processing repeat-pass images.

Repeat pass navigation is extended to include the effects of topographic variation and medium propagation speed errors in [8], but the field data described in the paper does not contain enough bathymetric variation to explore its effects on multi-pass navigation refinement. Subsequent experiments, however, were conducted in regions with high bathymetric variability, enabling direct observation of its effect on repeat-pass aperture localization. In Section 2 the details of the TomoSAS experiment will be presented. In Section 3 a review of bathymetry-augmented repeat pass navigation refinement will be given, and in Section 4 a quantified comparison between the navigation refinement estimates generated using a flat-bottom assumption vs. bathymetry will be made. Subsequently, the effects of navigation biasing due to bathymetry will be examined.

2 Experiment

In June 2015 a series of multi-pass circular synthetic aperture sonar (CSAS) scans were conducted with altitudes ranging from 4.5 to 6.9 meters in increments of 0.3 meters. Two vertically spaced receive arrays are present in the SAS system, increasing the sample density by a factor of two in the vertical dimension. The multi-pass scans were conducted off the coast of Panama City Beach, Florida in 20 meters of water over a rocky seafloor that contained outcroppings, crevices,

and growths of coral. Targets included barrels, a crab pot, a tire, and various UXO. The SAS was a multi-frequency system containing both high frequency and broad-band transmitters. The data products in this paper all came from the high-frequency band, which in SAS systems typically equates to the low hundreds of kilohertz. More information can be found in [8], in which similar experiments were conducted.

3 Bathymetry-aware aperture localization

The data from an assumed monostatic source and receiver at height h_s relative to the ground-plane may be projected to the ground plane by interpolating from slant-range $r_s = tc/2$ (t = round-trip travel time and c = propagation speed) to ground range r_g:

$$r_g = \sqrt{\mathrm{r}_s^2 - h_s^2}, \tag{1}$$

where h_s is the height of the source and r_s is slant-range. When applying (1), signals reflecting from scatterers at non-zero height will be mapped to an incorrect ground-range, with the residual ρ in terms of r_g, h_s and the local sub-sea topography $h_d(r_g)$ being equal to:

$$\rho_1 = \sqrt{r_g^2 - 2h_S h_d(r_g) + h_d(r_g)^2} - r_g. \tag{2}$$

In the present case the sediment altitude $h_d(r_g)$ is measured via interferometry using the vertically spaced pair of receivers on the AUV. Consider a second monostatic system having a nominal height of $h_s + h_1$ and nominal ground-range of r_1, where h_1 and r_1 represent the intended multi-pass vertical and horizontal spacing between scans. In practice there exists some height and range spacing error Δh and Δr superimposed on h_1 and r_1. The residual ground-range error for data collected by the second system using the nominal sensor location and incorporating the errors is:

$$\rho_2 = \sqrt{(1+2\sigma)\left(\tilde{r}_g^2 + \left(\tilde{h}_c - h_d(r_g) + \Delta h\right)^2\right) - \tilde{h}_c{}^2} \ldots$$

$$\cdots - (r_g + r_1), \tag{3}$$

$$\tilde{r}_g = (r_g + r_1 + \Delta r), \tag{4}$$

$$\tilde{h}_c = h_S + h_1. \tag{5}$$

In (3) an additional term σ has been incorporated to model the effects of small changes in the propagation speed of the environment between scans [8]. The ground-range residual shift $\rho_1 - \rho_2$ is measurable via patch-wise cross-correlation, and its form is determined by Δh, Δr and σ, but also by the bathymetry $h_d(r_g)$. In particular, if the sediment height is non-zero the difference term will also be non-zero as a result of the sensor baselines, even if no position or propagation speed errors are present. Linearizing $\rho_1 - \rho_2$ around Δh_0, Δr_0 and σ_0 results in

$$\Delta\rho \approx \psi + \psi_0 + \zeta_{\Delta r}(\Delta r - \Delta r_0) \ldots \tag{6}$$

$$\ldots \zeta_{\Delta h}(\Delta h - \Delta h_0) + \zeta_\sigma(\sigma - \sigma_0)$$

where

$$\zeta_{\Delta r} = \frac{(r_g + r_1 + \Delta r_0)(1+2\sigma_0)}{\psi_0} \tag{7}$$

$$\zeta_{\Delta h} = \frac{(h_S - h_d(r_g) + h_1 + \Delta h_0)(1+2\sigma_0)}{\psi_0} \tag{8}$$

$$\zeta_\sigma = \frac{(r_g + r_1 + \Delta r_0)^2 + (h_S - h_d(r_g) + h_1 + \Delta h_0)^2}{\psi_0} \tag{9}$$

$$\psi = \sqrt{r_g^2 - 2h_S h_d(r_g) + h_d(r_g)^2} + r_1 \tag{10}$$

$$\psi_0 = \cdots \tag{11}$$

$$\sqrt{(1+2\sigma_0)\left(\tilde{r}_{g0}^2 + \left(\tilde{h}_c - h_d(r_g) + \Delta h_0\right)^2\right) - \tilde{h}_c{}^2}$$

$$\tilde{r}_{g0} = (r_g + r_1 + \Delta r_0), \tag{12}$$

The basis functions (7) and (8) are similar to the sin- and cosine-of-grazing-angle rules that approximate range variation of phase for aperture perturbations in the height or range dimensions for stripmap systems (see e.g. [9]). In the present case similar bases are derived for ground-range projected data. Basis (9) is a 0th-order correction for medium propagation speed error. As with redundant-phase-center (RPC) analysis [10], regression of the linearized model in (5) with shift measurements made via patch-wise correlation between scans may be used to estimate the error parameters Δr, Δh and σ. A fit to the full non-linear model can be obtained by initializing Δh_0, Δr_0 and σ_0 to 0 and iteratively solving for Δr, Δh and σ and updating the expansion points. Note that the ψ_0 in the denominator causes each basis function to be dependent on the sediment height $h_d(r_g)$. Significant to the present study are the cases in which the bottom is represented as flat, (i.e. h_d is set to 0), or if h_d is estimated via onboard interferometry prior to solving for the error parameters.

4 Experimental results

Figure 1 shows the regression residuals for the cases in which bathymetry is and is not used during generation of the regression bases functions.

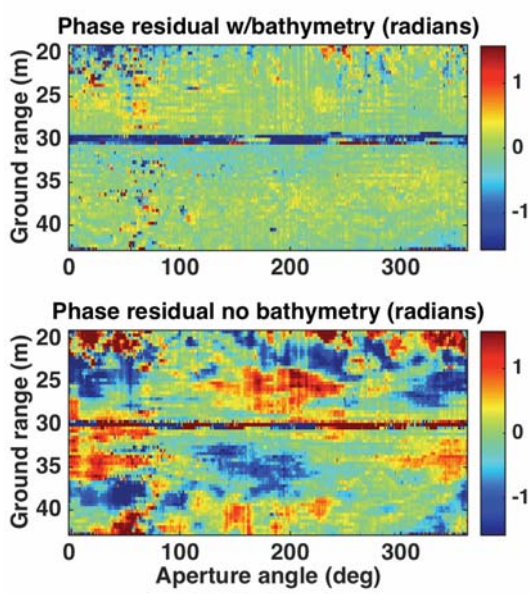

Figure 1: Phase residuals for regression in the cases where bathymetry is used when calculating the bases functions (top) or a flat sediment (bottom) is assumed. The color-scale is shown at right with units of radians.

From Fig. 1 it can be seen that the bathymetry augmented bases result in a lower residual. The regression algorithm attempts to minimize the sum-of-squares of the residual, and the presence of un-accounted bathymetric variation heavily influences the position estimates. This is illustrated in Fig. 2, in which Δr and Δh are plotted for the two cases.

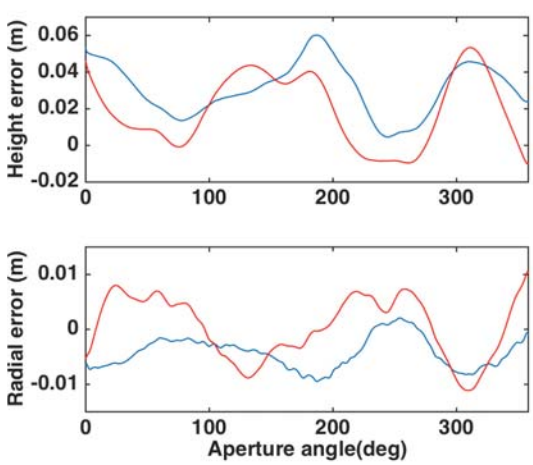

Figure 2: Δh (top) and Δr (bottom) estimates for the flat-bottom (red) and bathymetry (blue) regression instances.

In the present case, the difference in position estimated by the two approaches is on the order of centimeters. Figure 3 shows a maximum-intensity-projection of the vertically beamformed data onto the azimuth vs. height plane. The barrel is an approximately isotropic scatterer with several edges and ribs that should manifest as horizontal lines in the projection, though a slight tilt in the barrel will cause a small first-order sinusoidal variation.

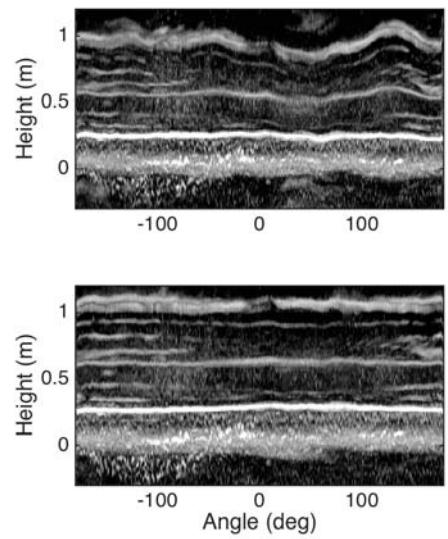

Figure 3: Maximum-intensity-projection images for the vertically beamformed multi-pass data. Data imaged using a flat-bottom assumption during coordinate co-localization is shown at top.

The top dataset, beamformed using the biased coordinates, shows significant fluctuations in the altitude profiles of the various scatterers. The severity of the fluctuations increases with height and is especially visible in the scattering off of the top edge of the barrel at approximately 1 meter.

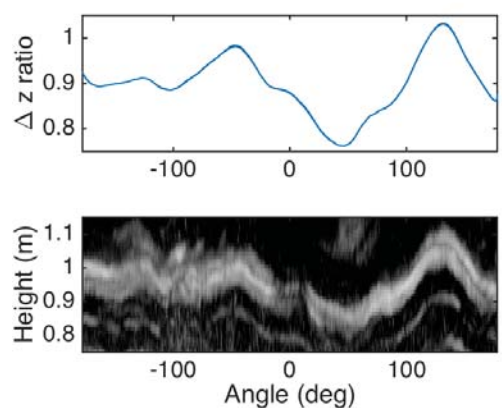

Figure 4: The vertical sample rate ratio $\Delta Z_{biased}/\Delta Z_{unbiased}$ (top) and the vertical scattering profile of the barrel vs. aperture location for the biased aperture coordinate case. (bottom).

To illustrate the cause of these fluctuations the average vertical spacing between scans was computed as a function of position along the aperture for the biased

aperture coordinates. These values were then normalized by the un-biased values. The ratio versus aperture position is plotted in Fig. 4 alongside the scattering from the top edge of the barrel. The similarity between the vertical fluctuation of the edge scattering from the top of the barrel and the sample rate ratio is a result of the Fourier relationship between the phase history and height of a scatterer (see, e.g. the discussion in [2]). The systematic expansion and contraction of the biased vertical array spacing estimates scales the perceived vertical sample rate. This scaling has little effect on scatterers with small vertical phase gradients, (the gradient is zero at $h = 0$), but as the altitude of a scatterer increases the effect of the sample rate scaling becomes more significant.

The final result of the bathymetrically induced distortion on the example data is shown in Fig. 5. The image is rendered using the VAA3D imaging tool [11]. Alpha-mapping is utilized and low intensity scatterers are thresholded out of the image to make the distortion more visible.

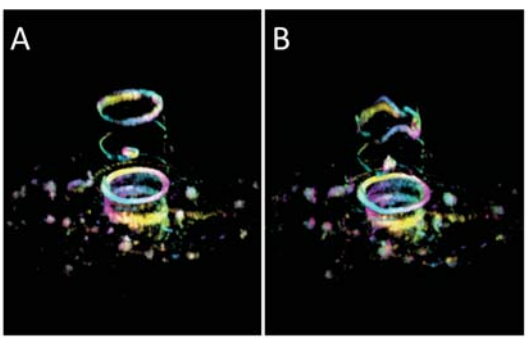

Figure 5: 3D rendered tomographic images of the barrel data, with color-encoded aperture data [8], for the unbiased (A) and biased (B) aperture coordinate instances.

In Fig. 5B the results of aperture coordinate biasing are highly visible in the edge-scattering off the top of the barrel, and comparable to the vertical fluctuations visible in Fig. 3A. In contrast, scatterers near the ground plane, such as sea-bed features, appear to be less distorted.

5 Conclusion

When data-driven approaches are necessary for the refinement of position estimates in the scans comprising a multi-pass set, the potential exists for the topography of the scanned scene to bias the position refinements if left unaccounted for. The results of this biasing is an erroneous expansion and contraction of the estimated vertical scattering profile which can cause high levels of distortion in a tomographically reconstructed image. A method was described for preventing alignment biasing, and an example TomoSAS image processed using this method was greatly improved.

6 Acknowledgements

This work was supported in part by the Office of Naval Research under grants N000141410087 and N0001415WX00344, and the Strategic Environmental Research and Development Program under grant number #MR-2439.

References

1. D. Ho Tong Minh et al., “Relating P-band synthetic aperture radar tomography to tropical forest biomass,” IEEE Trans. Geosci. Remote Sens., vol. 52, no. 2, pp. 967–979, Feb. 2014.
2. X. Zhu and R. Bamler, “Very high resolution spaceborne SAR tomography in urban environment,” IEEE Trans. Geosci. Remote Sens., vol. 48, no. 12, pp. 4296–4308, Dec. 2010.
3. O. Ponce et al., “Fully polarimetric high-resolution 3-D imaging with circular SAR at L-Band,” IEEE Trans. Geosci. Remote Sens., vol. 52, no. 6, pp. 3074–3090, June 2014.
4. C. H. Casteel, et al., “A challenge problem for 2D/3D imaging of targets from a volumetric data set in an urban environment,” SPIE Defense and Security Symp., Orlando, FL, Apr. 9–13, 2007.
5. T. Saebo, R. E. Hansen, H. J. Callow and S. A. V. Synnes, “Coregistration of synthetic aperture sonar images from repeated passes,” Proc. UAM: Technologies and Results (UAM2011), 2011.
6. A. J. Hunter, S. D. Dugelay and W. L. Fox, “Repeat-Pass SAS Micro-Navigation using Redundant Phase Center Arrays,” IEEE JOE 2015 (In Press).
7. T. G-Michael et al., “Image-based Automated Change Detection for Synthetic Aperture Sonar by Multi-Stage Co-Registration and Canonical Correlation Analysis,” IEEE J. Ocean eng., (early access), Nov. 2015.
8. T. Marston and J. Kennedy, “Volumetric acoustic imaging via circular multi-pass aperture synthesis“ IEEE J. Ocean Eng., (early access), Feb. 2016.
9. A. Reigber, P. Prats, JJ Mallorqui, “Refined estimation of time-varying baseline errors in airborne SAR interferometry,” IEEE Geoscience and Remote Sensing Letters, vol. 3, no. 1, pp. 145-149, Jan. 2006.
10. D. A. Cook, “Synthetic aperture sonar motion estimation and compensation,” M.S. thesis, Georgia Tech, Atlanta, USA, 2007.
11. Peng et al, “V3D enables real-time 3D visualization and quantitative analysis of large-scale biological image data sets,” Nature Biotechnology, vol. 28, no. 4, p. 348-355, 2010.

TomoSAS images of acoustically penetrable objects

Timothy Marston, APL-UW, marston@apl.washington.edu, USA
Jermaine Kennedy, NSWC-PCD, Jermaine.kennedy@navy.mil, USA

Abstract

The long acoustic wavelengths of synthetic aperture sonar systems relative to other high-resolution acoustic imaging methods allow for enhanced acoustic penetration of objects, enabling visualization of internal features. Discrimination between internal and external features is difficult in conventional SAS images, however, because of the lack of a height dimension. Interferometry can be used to resolve the vertical location of scatterers but this technique fails to resolve vertical scattering distributions within a pixel. In contrast, synthetic aperture tomography, which makes use of multiple scans to form a multi-dimensional array, can be used to generate 3D voxel-based imagery capable of resolving vertical scatterer distributions. These volumetric images enable identification of both the internal and external features of targets. In this paper, TomoSAS images of two acoustically penetrable objects are examined: a lobster trap and a plastic barrel with a sphere suspended inside.

1 Introduction

Many technologies exist for generating high-resolution three-dimensional visualizations of objects on the sea floor. Examples include acoustic or optical micro-bathymetry systems [1], [2], planar or cross arrays [3], multi-view sonar reconstruction [4], and interferometric SAS [5]. Though all of these technologies can generate high quality 3D representations of targets, synthetic aperture sonar systems are advantageous for applications in which internal feature reconstruction is important. The relatively long wavelengths used in SAS systems tend to attenuate more slowly and penetrate boundaries better than acoustic counterparts with shorter wavelengths. Interferometric SAS, however, does not provide the ability to estimate the height of more than one scatterer per pixel (i.e. “range-layover” [6]). Alternatively, if multiple scans are conducted at varying altitudes then a volumetric rendition of a target’s reflectivity function can be generated by coherently beamforming in three dimensions. In the analogous field of synthetic aperture radar this process is called radar tomography, or “TomoSAR” [7], and applications vary from range layover resolution and deformation measurements [8] to remote sensing of sub-ice geology [9] and biomass estimation [10].

In this paper, TomoSAS case studies of two common underwater clutter objects, (a lobster trap and a barrel), are examined. Target penetration, internal feature reconstruction, and the resolution of range layover are demonstrated. Additionally, the vertical scattering profile for the case of the plastic barrel is examined, to identify the dominant scattering mechanisms of the target.

2 Experiment details

In June 2015, circular scans around targets were conducted to assemble a multi-dimensional array suitable for tomographic data processing.

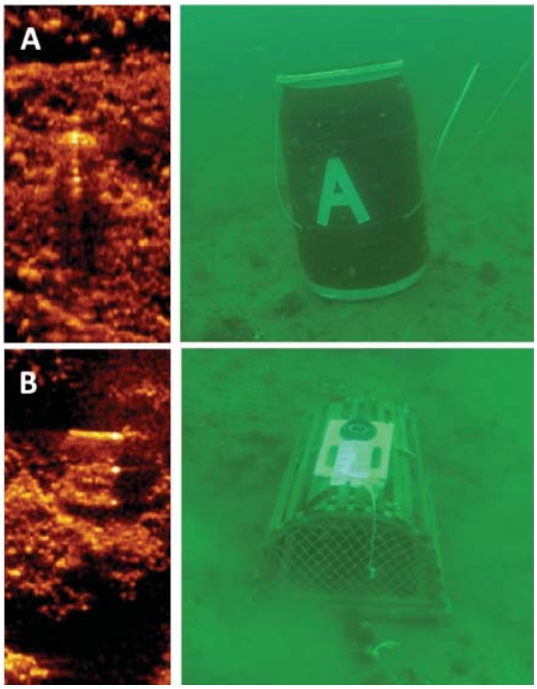

Figure 1: SAS images (L) and photos (R) of targets. A) a vertical plastic barrel, and B) a wooden lobster trap.

The scans had a fixed radius of 30 meters and varied in altitude from 4.5 meters to 6.9 meters in increments of 0.3 meters, resulting in 9 scans. The SAS system,

mounted on a Remus 600 AUV [11], has a pair of parallel, vertically spaced receive arrays forming an interferometric baseline. The pair of receive arrays provides two vertical sample points per scan, resulting in a total of 18 samples in the vertical dimension. Targets were intentionally placed in rocky areas containing coral growths, outcroppings and crevices. Photos of the submerged targets and conventional SAS images are shown in Fig. 1. Due to a lack of GPS localization underwater and the reliance upon dead-reckoning based navigation, the aperture coordinates had significant positional uncertainty. Redundant phase center micro-navigation [12] and multilateration [13] were used to refine the 3D navigation estimates for the individual scans. The multi-stage, bathymetry-aware localization process described in [14] was used to estimate the relative locations of the aperture points in all of the scans to the precision necessary for three dimensional beamforming. Finally, the wideband block-sparse method described in [14] was used to beamform the data in the irregular and undersampled vertical dimension, and projection slice beamforming in conjunction with a farfield transformation [15] was used to beamform in the horizontal dimensions.

3 Experiment results

Fig. 2 shows three renditions of the wooden lobster trap, generated from the volumetric tomography images. Each image was generated using the Vaa3D visualization tool [16]. Fig. 2A is a 3D view of the object rendered using alpha blending. This imaging method gives an intuitive sense for the three-dimensional distribution of the reflectivity function of the target. The color-coding in this figure and in subsequent figures corresponds to the aspect-angle of ensonification and is useful for discriminating between scattering mechanisms. The cross-sections in Fig. 2B and 2C highlight some key target features. In Fig. 2B the rounded top of the lobster trap and reflections from the individual wooden slats are visible, but inside the trap a vertical post is also visible. Furthermore, the bottom of the trap and the sediment beneath are also visible. In Fig. 2C one of the circular inlets of the trap which lies behind a rectangular opening is visible. This same circular inlet is also visible in the alpha blended rendition in Fig. 2A.

Fig. 3 shows the 3D tomographic image of the vertically oriented barrel. A metal shotput was suspended from the center of the lid of the barrel, and the bottom 8 inches were filled with concrete. Focused scattering from the internally suspended shotput is clearly visible in the cutaway shown in Fig. 3. The backscattering appears to be dominated by corner scattering and edge diffraction.

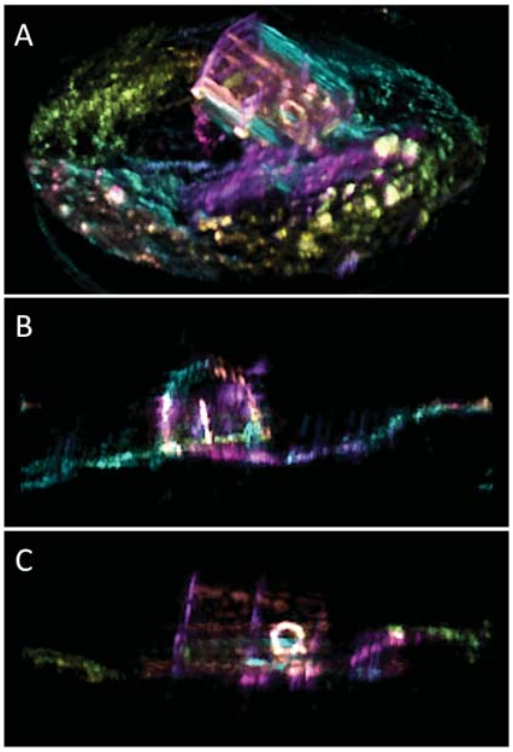

Figure 2: Tomographic image of a lobster trap. A) alpha blended volumetric rendering, B) cross section in the X = 0 plane, C) cross section in the Y = 0 plane.

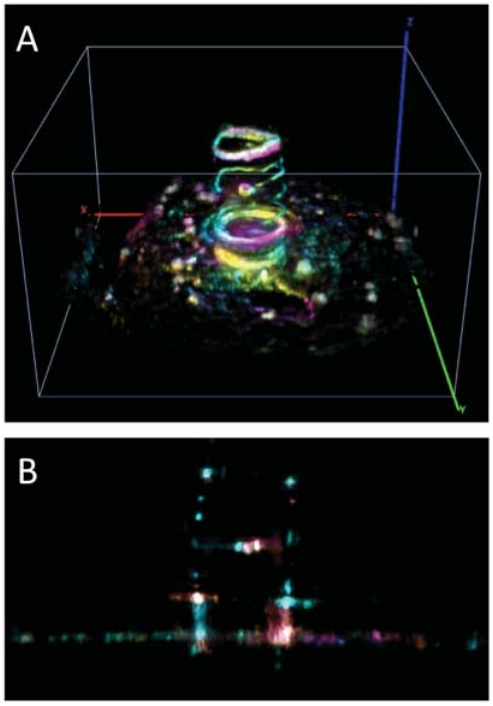

Figure 3: Tomographic image of a plastic barrel. A) The alpha blended volumetric image. B) A cross section showing scattering features.

The backscattering mechanisms for the barrel were enhanced by averaging the magnitudes of the vertically beamformed data over approximately 20 degrees of the circular aperture. The results are shown in Fig. 4, along with a cutaway schematic of the target and identified scattering mechanisms.

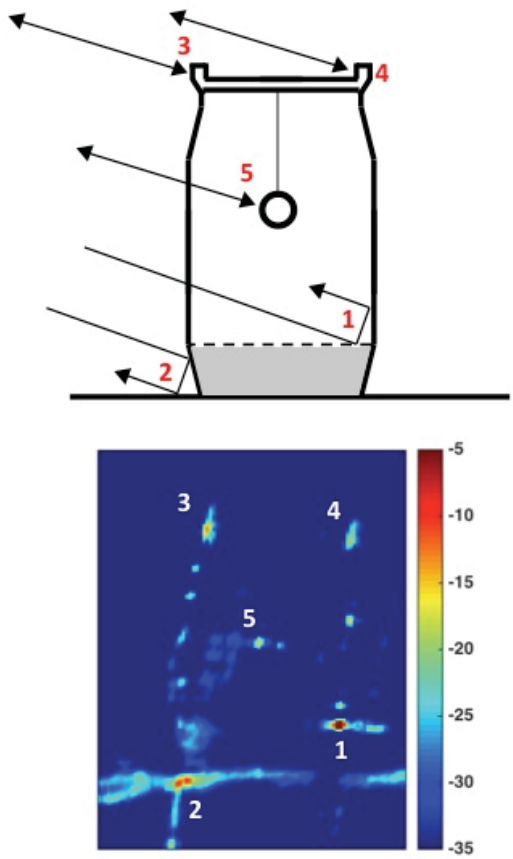

Figure 4: The vertically beamformed backscattering response for the plastic barrel, averaged over a span of azimuthal ensonification angles. The hypothesized backscattering mechanisms are labeled 1 – 5.

Feature 1, labeled in Fig. 4, is by far the strongest scattering mechanism and appears to correspond with internal corner scattering off of the concrete and backside of the barrel. Interestingly, this brightest feature is only visible as a result of the elasticity of the target material. Presumably, the concrete at the bottom of the barrel is too smooth to produce rough surface scattering of sufficient strength to appear in the vertical scattering profile. Feature 2 is another corner scatterer, however the amplitude is not as strong as feature 1. This is possibly because the barrel is slanted near the base and the feature isn't a true corner reflector. Additionally, scattering off of the sediment will be diffuse because of roughness. Features 3 and 4, the next strongest, appear to be scattering from the leading edge and back of the barrel lid. Feature 5, internal scattering from the suspended sphere, is also clearly visible. Other scattering features are visible in Fig. 4, however the particular mechanisms associated with these features are weaker and their cause is not as obvious as features 1 – 5.

4 Conclusions

The high-resolution three-dimensional imagery produced by multi-pass tomographic SAS allows internal features of targets to be examined and scattering mechanisms to be identified in ways that are impossible with conventional two-dimensional or interferometric SAS processing. Internal feature visualization has many potential applications, ranging from determining if objects contain hazardous or valuable substances to non-destructive testing, and identifying derelict crab or lobster traps. Because synthetic aperture technology is employed, the process could potentially be scaled up to encompass larger objects while retaining the same resolution. From a target recognition standpoint, understanding scattering mechanisms may be key to identifying or classifying targets and this technology also provides a method for labeling features and assigning them to physical scattering mechanisms. As demonstrated by the dominance of the interior corner scatterer of the barrel, this process can also highlight key material properties of the object being analyzed.

5 Acknowledgements

This work was supported in part by the Office of Naval Research under grants N000141410087 and N0001415WX00344, and the Strategic Environmental Research and Development Program under grant number #MR-2439.

References

[1] Roman, C. N. et al, "Development of high-resolution underwater mapping techniques." In K. L. C. Bell and S. A. Fuller (eds.), New Frontiers in Ocean Exploration: The E/V Nautilus 2010 Field Season. Oceanography 24(1), supplement, pp. 42-45.

[2] Schmidt, Val E., and Yuri Rzhanov. "Measurement of micro-bathymetry with a GOPRO underwater stereo camera pair." IEEE OCEANS'12, Hampton Roads, VA, Oct. 2012.

[3] Liu, Xuesong, et al. "A Low-Complexity Real-Time 3-D Sonar Imaging System With a Cross Array." IEEE J. Ocean. Eng. (Early Access) 2015

[4] Aykin, Murat D., and Shahriar Negahdaripour. "On 3-D target reconstruction from multiple 2-D forward-scan sonar views." IEEE OCEANS'15, Genova, May 2015.

[5] Hansen, Roy Edgar, et al. "Signal processing for AUV based interferometric synthetic aperture sonar." IEEE OCEANS'03, San Diego, CA, Sept. 2003

[6] H. D. Griffiths et al. "Interferometric synthetic aperture sonar for high-resolution 3D mapping of the seabed," IEEE Proc. Radar, Sonar Navigation, vol. 144, no. 2, pp. 96–103, Apr. 1997

[7] Wang, Yuanyuan, et al. "Operational TomoSAR processing using TerraSAR-X high resolution spotlight stacks from multiple view angles." IEEE IGARSS, Munich, July 2012.

[8] X. Zhu and R. Bamler, "Very high resolution spaceborne SAR tomography in urban environment," IEEE Trans. Geosci. Remote Sens., vol. 48, no. 12, pp. 4296–4308, Dec. 2010.

[9] Ponce, Octavio, et al. "Polarimetric 3-D imaging with airborne holographic SAR tomography over glaciers," IEEE IGARSS, Milan, July 2015.

[10] O. Frey, F. Morsdorf, and E. Meier, "Tomographic processing of multi-baseline P-band SAR data for imaging of a forested area," IEEE IGARSS, Barcelona, July 2007

[11] R. P. Stokey et al., "Development of the REMUS 600 autonomous underwater vehicle," IEEE OCEANS'05, Washington DC., Sept. 2005.

[12] A. Bellettini and M. A. Pinto, "Theoretical accuracy of synthetic aperture sonar micronavigation using a displaced phase-center antenna," IEEE J. Ocean. Eng., vol. 27, no. 4, pp. 780–789, Oct. 2002

[13] H. Cantalloube and C. Nahum, "Multiscale local map-drift-driven mul-tilateration sar autofocus using fast polar format image synthesis," IEEE Trans. Geosci. Remote Sens., vol. 49, no. 10, pp. 3730–3736, Oct. 2011

[14] T. Marston and J. Kennedy, "Volumetric acoustic imaging via circular multi-pass aperture synthesis" IEEE J. Ocean Eng., (early access), Feb. 2016

[15] D. S. Plotnick, P. L. Marston, and T. M. Marston, "Fast nearfield to farfield conversion algorithm for circular synthetic aperture sonar," J. Acoust. Soc. Amer. express letters, vol. 136, August 2014.

[16] Peng et al, "V3D enables real-time 3D visualization and quantitative analysis of large-scale biological image data sets," Nature Biotechnology, vol. 28, no. 4, p. 348-355, 2010.